Design method for open geotextiles

Q.J. Thomas

TU Delft

Boskalis

Design method for open geotextiles

The development of a design method for geotextiles under a single granular filter layer based on the principles of open filters.

by

Q.J. Thomas

in partial fulfilment of the requirements to obtain the degree of Master of Science

at the Delft University of Technology

Student number: 4460197
Study: MSc Hydraulic Engineering

Project duration: September 11, 2022 - July 6, 2023

Thesis committee:	Dr. ir. B. Hofland,	TU Delft (chair)
	Ir. J. van den Bos,	Royal Boskalis Westminster N.V. (supervisor)
	Ing. C. Kuiper,	Witteveen+Bos
	Prof. dr. ir. W.S.J. Uijttewaal,	TU Delft
	R.W. Pol,	Van Aalsburg B.V.

Cover: Jute geotextile - (Photo from database Van Aalsburg)

Preface

Before you lies the thesis "Design method for open geotextiles". It has been written to fulfill the graduation requirements of the Masters program Hydraulic Engineering at Delft University of Technology. This work was conducted at Royal Boskalis Westminster N.V., a contractor in the maritime industry, over a period of 10 months from September 2022 to July 2023. The Hydronyamic engineering department of Boskalis always treated me with kindness and provided ample support. Therefore, I highly recommend doing a graduation internship at this company!

I would like to thank my thesis committee for helping me deliver this master thesis. Thank you, Jeroen van den Bos; my daily supervisor at Boskalis. Your personal attention and guidance really stood out. You always made time to passionately explain the engineering profession and the difficulties that come with it. This was greatly appreciated. Secondly, I would like to thank the chair of the committee, Bas Hofland. Your enthusiasm and passion for solving maritime problems from a higher perspective have always helped me to zoom out and focus on the overall goal of the research. Furthermore, I would like to thank Coen Kuiper, Wim Uijttewaal and Robert Pol for their guidance and insightful discussions during our meetings. Their input greatly assisted me in presenting the research more effectively and focusing on the ultimate goal.

Last but not least, I would like to thank my family and friends. Especially, Opa Henk for always standing ready when needed, his positive feedback on the work I have produced has been incredibly uplifting and motivating.

Q.J. Thomas
Rotterdam, July 2023

Abstract

Geotextiles are permeable fabrics used in various civil engineering and construction applications for the protection against erosion and scour. Geotextiles have predominantly been manufactured using synthetic materials due to their durability and precise design pore sizes. However, the environmental concerns associated with synthetic geotextiles have led to the exploration of sustainable alternatives, including natural fibers and biodegradable thermoplastic polymers.

This study addresses the problem of designing stable geotextile filters. The problem statement resolves around the assumption that geotextiles of natural fibers are considered "open" filters. Existing design criteria for open filters do not directly account for load conditions or the use of fibers in the fabric. Instead, they rely on the relationship of the geometrical properties of the base and filter material. To address this gap, a new approach is proposed based on hydraulic pressure gradients. This approach considers the actual gradient and critical gradient at the geotextile interface. To achieve this, the geotextile will be evaluated within the context of an open channel with uniform flow conditions.

The main research objective is to formulate a design method for geotextiles based on the principles of an open filter structures under a single granular filter layer. A comprehensive literature review has been conducted to investigate the hydrodynamic processes that define the actual gradient at the filter/base interface where the geotextile is positioned. The framework of linear wave theory proved to be a valuable tool for investigating and modeling these hydrodynamic processes. To define the actual gradient, the following hypothesis is proposed:

The actual gradient can be defined by adding the average gradient to a turbulent component derived from measured turbulent wall pressure spectra at the top of the filter layer. Based on spectral approach and linear damping, it is hypothesized that these turbulent components undergo damping within the filter layer, resulting in a diminished turbulent component at the filter/base interface.

From the literature review, it can be inferred that the dimensionless turbulent rough wall pressure spectra developed by Blake (1970) offer the most appropriate representation for the relevant hydraulic conditions (rough horizontal bed, uniform open channel flow). In a turbulent wall pressure spectrum, outer scaling variables and inner variables relate to different length scales within the flow, representing large-scale and small-scale fluctuations, respectively. In this hypothesis, it is assumed that the low-frequency region is scaled by the average velocity u_0 and water depth h, while the scaling variables for the high-frequency region are presented in terms of the shear velocity u_* and nominal diameter of the filter material d_{n50}. By combining both spectra, converting the pressure spectrum to the gradient spectrum, and transforming the spectral domain to the spatial record, the fluctuating gradient can be determined.

The hypothesis was verified using measured data from experiments conducted by Van de Sande (2012) and Wolters & Van Gent (2012). By incorporating Van de Sande's measured dataset into the scaling parameters of the dimensionless pressure spectra and determining the stability parameter for open filters, it was concluded that qualitatively the results align with Van de Sande's findings, indicating stability or instability of the filter layer. However, in some test cases, the hypothesis suggested instability while the experiments indicated stability.

This discrepancy may be due to the fact that while the stability parameter may indicate an unstable filter, it does not necessarily correlate with significant base material transport through the filter layer. In a quantitative analysis, the amount of dimensionless transport of base material was compared to the stability parameter. According to the data presented in figure 4.12, it can be observed that the stability parameter exhibits a value that is three times larger then the stability parameter defined by Schiereck (2012), while not inducing any significant transport of base material. This finding aligns with previous experimental investigations, such as the study conducted by Wolters & Van Gent (2012), which similarly demonstrated that the stability parameter could reach values that are two to three times larger, while still not resulting in notable base material transport.

A direct quantitative comparison was conducted between the measured dataset of Wolters & Van Gent (2012) and the calculated gradients obtained from the hypothesis. The results revealed that the calculated gradients exhibited a comparable magnitude, ranging from 0.25 smaller to 1.50 larger in comparison to the measured gradients reported by Wolters & Van Gent (2012). This indicates a reasonably close agreement between the calculated and measured gradients.

In conclusion, the research objective in this study was to formulate a design method for open geotextiles under a single granular filter layer. To achieve this, it was necessary to take some steps back and define the actual gradients, as well as identifying a suitable method for calculating these gradients. The actual gradient is calculated with the sum of the average gradient and the fluctuating gradient. The fluctuating gradient can be characterized by the turbulent wall pressures, which are derived from the pressure spectrum measured at the top of the filter layer, as described in Blake (1970). Assuming linear damping of the pressures within the filter layer, the actual gradient can be computed at the interface of the geotextile. Consequently, the assessment of stability entails a comparison between this calculated actual gradient and the critical gradient measured by Lemmens (1996).

With a clearer understanding of how to calculate the actual gradients at the geotextile interface, the same approach employed in the hypothesis is applied to address the design of a stable open geotextile under a single granular filter layer. This has been demonstrated through a case study, where the thickness of the filter layer was determined to create a stable filter structure.

Several recommendations can be made to improve the understanding and design methodologies in relation to the hypothesis. Firstly, there is a need for a better understanding of the spectral density of wall pressure fluctuations in open channel flow. This understanding will enable more accurate estimations of fluctuating gradients. Secondly, further research is necessary to incorporate the distribution of pressure at the filter/base interface for non-linear damping. Thirdly, it is advised to conduct tests using modern natural geotextile materials to refine the critical gradient determination and explore alternative approaches, such as considering critical filter velocities. Lastly, it is recommended to extend the design method to encompass wave conditions. Verifying the effectiveness of the design approach under wave conditions through comparison with measured data will ensure its applicability and reliability in practical scenarios.

While further investigations are needed, it still offers a fresh perspective on evaluating the stability of open filter structures. If successfully refined, the design method could become a valuable tool in geotextile design and potentially find applications in other contexts involving "open" structures.

Contents

List of Symbols

Roman symbols

Symbol	Unit	Description
A	$[m^2]$	area
a	$[s/m]$	Forchheimer coefficient
B	$[m]$	width
b	$[s^2/m^2]$	Forchheimer coefficient
C	$[s^2/m^2]$	Chézy coefficient
c_f	$[-]$	dimensionless friction coefficient
c_g	$[m/s]$	group velocity of waves
D	$[s]$	duration
D_f	$[m]$	filter thickness
d	$[m]$	diameter
d_{n50}	$[m]$	nominal diameter
d_x	$[m]$	grain diameter, where x% of the grains has a smaller diameter
$E(x)$	$[-]$	mean value of "x"
e	$[m]$	thickness of the geotextile
F	$[N]$	force
F_D	$[N]$	drag force
F_S	$[N]$	shear force
F_L	$[N]$	lift force
f	$[Hz]$	frequency
g	$[m/s^2]$	acceleration of gravity $[g = 9.81 m/s^2]$
H	$[m]$	wave height
h	$[m]$	water depth
h_s	$[m]$	step height
I	$[-]$	mobility parameter
I_c	$[-]$	stability parameter
i	$[-]$	gradient
$\bar{i}$	$[-]$	average gradient
i'	$[-]$	fluctuating gradient
i_a	$[-]$	actual gradient
$i_{2\%}$	$[-]$	two percent exceedance value of the gradients
i_c	$[-]$	critical gradient
K	$[m/s]$	permeability coefficient (Darcy coefficient)
K	$[-]$	coefficient Izbash
KCF	$[-]$	Keulegan-Carpenter number
k	$[m^{-1}]$	wave-number
k_{D_f}	$[m^{-1}]$	maximum damped wave-number
k_r	$[m]$	(equivalent) roughness of bottom
k_g	$[m]$	geometric height
k_s	$[m]$	(equivalent) sand roughness height
k_{max}	$[m^{-1}]$	maximum sampling wave-number
L	$[m]$	length of the spatial record
L	$[-]$	length scale
l	$[m]$	length

Symbol	Unit	Description
N	$[-]$	number of repetitions of the record
n	$[-]$	sequence number of the wave in the record
n_f	$[-]$	porosity in the filter
O_x	$[m]$	opening size, where x% of the pore sizes have a smaller diameter
p	$[N/m^2]$	pressure
p'	$[N/m^2]$	fluctuating pressure
P	$[m/m]$	permeability per m thickness
P	$[-]$	pressure scale
q	$[N/m^2]$	dynamic head
q_s	$[g/m/h]$	sediment transport rate divided by the width
q_s^*	$[-]$	dimensionless form of q_s
R	$[m]$	hydraulic radius
Re	$[-]$	Reynolds number
Re_*	$[-]$	particle Reynolds number
T	$[s]$	period, time-scale or duration
T	$[g/m/s]$	transported base material
T_*	$[-]$	dimensionless for of T
t	$[s]$	time
U	$[-]$	velocity scale
U_∞	$[m/s]$	free-stream velocity
U_τ	$[m/s]$	friction velocity
U_e	$[m/s]$	edge velocity
U_ν	$[m/s]$	shear velocity
u	$[m/s]$	streamwise velocity (in x-direction)
u_0	$[m/s]$	average velocity
u_*	$[m/s]$	shear velocity
u_c	$[m/s]$	convection velocity or critical velocity
u_f	$[m/s]$	filter velocity
$u_{b,c}$	$[m/s]$	critical base velocity
$u_{f,c}$	$[m/s]$	critical filter velocity
$Var(x)$	$[-]$	variance of "x"
V_G	$[-]$	$[V_G = 1 - \frac{d_{15}}{d_{50}}]$
w	$[-]$	transverse velocity
x	$[-]$	coordinate in direction of the flow
y	$[-]$	vertical coordinate
z	$[-]$	transverse coordinate

Greek symbols

Symbol	Unit	Description
α	$[-]$	empirical constant (various uses), random phase
β	$[-]$	Forchheimer coefficient or fitting coefficient
γ	$[-]$	transport parameter
δ	$[m]$	boundary layer thickness
δ^*	$[m]$	displacement thickness layer
Δ	$[-]$	specific submerged density of stone ($\equiv \rho_s/\rho - 1$)
∇	$[-]$	divergence of the gradient
η	$[m]$	surface elevation
η_c	$[-]$	relative strength
η	$[-]$	relative load
η^2	$[-]$	variance
κ	$[-]$	Von Kármán constant [$\kappa \approx 0.38$]
λ	$[m]$	wavelength
ρ	$[kg/m^3]$	density
ρ_w	$[kg/m^3]$	density of water [$\rho_w = 1000 kg/m^3$]
ρ_s	$[kg/m^3]$	density of stones
σ	$[-]$	standard deviation
τ	$[N/m^2]$	shear stress
τ_w	$[N/m^2]$	wall shear stress
τ_b	$[N/m^2]$	bed shear stress
τ_c	$[N/m^2]$	critical shear stress
ν	$[m^2/s]$	kinematic viscosity [$\nu = 10^{-6} m^2/s$]
ψ	$[m]$	pressure head
Ψ	$[-]$	stability parameter
Φ_{xx}	$[-]$	power spectral density of signal x
Φ^+	$[-]$	dimensionless form of Φ
ω	$[rad/s^{-1}]$	angular frequency or radian frequency
ω^+	$[-]$	dimensionless form of ω

Mathematics

Notation	Description
$\|x\|$	absolute value of x
$\min(x)$	minimal value of all elements of x
$\max(x)$	maximum value of all elements of x
$\overline{x}$	temporal average of x
x'	fluctuating part of x around $\overline{x}$
x^+	dimensionless form
$\propto$	proportional to
$\approx$	approximately equal to
$\frac{\partial}{\partial}$	partial derivative
$\int$	integral
$f(x)$	unspecified function of x
Δx	difference between two values of x

Abbreviations

Abbreviation	Description
BFS	backward-facing step
D-L	densely packed large elements
PE	polyethylene
PP	polypropylene
RVB	rijksvastgoedbedrijf
S-S	sparsely packed small elements
TWP	turbulent wall pressures

1 Introduction

1.1 Background

Geotextiles are permeable fabrics that can be made of synthetic fibers or natural fibers. Common materials used for geotextiles include PP, PE, polyester, bio-based materials, and natural fibers. However, since this study pays particular attention to the loading forces on geotextiles, the specific type of material is not discussed in detail. Geotextiles serve various functions, including filtration, retention, and reinforcement (Lama et al., 2021). This report emphasizes the filter function of geotextiles. Filters can be classified into two types: geometrically closed filters and geometrically open filters. For the purpose of this study, the focus is on geometrically open filters. This choice is motivated by the growing market demand for using natural materials, which often exhibit a more open structure.

Numerous studies have investigated the behavior and properties of geotextile materials. The majority of these studies have focused on synthetic geotextiles. Additionally, the coarse nature of most natural fibers makes it challenging to manufacture fabrics with precise design pore sizes (Lama et al., 2021). Consequently, synthetic geotextiles have been globally adopted for various applications. However, due to growing environmental concerns and the desire to reduce plastic waste, alternative options are currently being explored to replace synthetic geotextiles. Recent research has identified two potential alternatives: natural fibers in geotextile applications and biodegradable thermoplastic polymers (Prambauer et al., 2019). Several types of natural fibers show promise as alternatives to synthetic geotextile fibers, with jute and coir mats being the most prominent candidates (Álvarez-Mozos et al., 2014). Lemmens (1996) extensively argued this point, highlighting the inadequacy of traditional fascine mattresses in terms of sand tightness and proposing alternative natural materials with improved sand retention. One such alternative is jute, which demonstrates comparable sand tightness to conventional synthetic geotextiles.

Starting from 2023, the Dutch Central Government Real Estate Agency, known as Rijksvastgoedbedrijf (RVB), will implement circular procurement practices across all its renovation, new construction, and demolition projects. This initiative aims to promote the adoption of circular building practices within the construction industry, with a strong focus on waste reduction and minimizing the adverse environmental effects associated with construction activities. The RVB has set the ambitious goal of achieving full circularity in all its contracts by 2030 (Du Saar, 2022). While synthetic geotextiles have been widely utilized in construction, their potential contribution to the accumulation of microplastics in the environment has raised significant concerns. Throughout their application process, geotextiles interact with various environmental factors, such as solar irradiation, temperature, chemical agents, and biological agents in a marine environment. Extended exposure to these factors causes harm to geotextiles, leading to a decrease in their lifespan. Consequently, the materials deteriorate and release microfibers (Carneiro et al., 2019). A recent study (Bai et al., 2022), presented evidence demonstrating the role of geotextiles in the presence of microfibers within the environment. This has led to questions regarding the environmental impact of using synthetic geotextiles in construction and their alignment with the principles of circular building. Consequently, efforts are underway to develop environmentally friendly and circular alternatives to synthetic geotextiles, including geotextiles made from natural fibers.

According to Khan (2022), a geotextile filter must meet two essential criteria: retention and permeability. The retention criterion ensures that the filter openings are sufficiently small to prevent excessive erosion of soil particles, while the permeability criterion ensures that the filter openings are large enough to allow water to pass through without significant impedance (PIANC-MarCom report 113, 2011). Carroll (1983) adds an additional requirement to prevent clogging of fine particles within the geotextile pores, as this would otherwise reduce permeability. Moreover, Lama (2021) highlights the importance of durability and tensile strength in geotextiles. While geotextiles made of synthetic materials can, in principle, meet these criteria and conditions, it is challenging to produce natural fiber geotextiles that satisfy all these requirements and provide guarantees for clients.

This study intends to present a design method for natural fiber geotextiles that follows the criteria of an open filter structure. In this research, the geotextile serves as a bed protection with a primary focus on its filter function. Other criteria that pertain to the properties of geotextiles themselves are not considered in this report.

1.2 Problem description

Regarding bed/bank protections, it has been demonstrated that geotextiles can serve as a substitute for multiple layers of granular filter material, thereby maintaining filter capabilities while reducing the overall thickness of the filter layer. In the case of granular open filters, a well-established design criterion exists, comprising a mobility parameter and a stability parameter (CUR, 1993). To achieve a stable geometrically open filter construction, the mobility parameter must be smaller than the stability parameter. This ensures that the filter remains stable and prevents erosion. Various methods for designing geometrically stable open filter structures have been documented in the literature, including the design formula proposed by Hoffmans (2012). However, a common limitation of these methods is that none of them directly takes the load conditions, such as hydraulic loads, into account. Instead, they approach them indirectly by relying on the geometrical properties of the base and filter material. Unfortunately, it is not possible to apply this relationship to natural fibers as they are not composed of the same material as the base layer.

The problem statement revolves around the design of geotextiles composed of natural fibers. Given the natural fiber composition, the resulting filter structure can be classified as an open filter. Therefore, the primary focus of this study revolves around the development of a design method for open filters. One approach to assess the stability of an open filter structure involves treating the mobility parameter as a horizontal hydraulic pressure gradient occurring at the geotextile interface. Simultaneously, the stability parameter represents the critical gradient that initiates material movement and makes the filter unstable.

In order to determine the stability of the geotextile, two conditions must be determined: the critical gradient and the actual gradient. In 1996, Lemmens conducted research on the critical gradients for different filter materials, including natural filters and synthetic geotextiles, in a horizontal flume with uniform flow conditions. His research involved a test setup with different materials, where head loss caused the sandy material of the base layer to stir up through the filter material and enter the flume. He defined the critical gradient as the head loss corresponding to the threshold at which sandy material passed through the filter layer. Based on the test results, jute was identified as an alternative that matched the conventional synthetic geotextile in terms of sand tightness filters, as determined by the critical gradient.

The test results conducted by Lemmens provide an initial insight into the critical gradients identified for various natural geotextiles. For practical design purposes, the determination of the actual gradient at the interface of the filter/geotextile and base material is an essential parameter that is currently missing. Once this gradient can be determined, the design method for alternative filter materials, such as natural materials, can be evaluated to determine their suitability as substitutes for synthetic geotextiles. This approach could be an attractive measure to reduce the use of plastic in hydraulic engineering.

1.3 Objective and research questions

This study emphasizes on understanding the actual gradients. To achieve this, the geotextile will be evaluated within the context of an open channel with uniform flow conditions where the geotextile is protected under a single granular filter layer. The main research objective is:

To formulate a design method for geotextiles under a single granular filter layer based on the principles of open filters.

In order to attain this objective, the following research questions have been formulated:

1. How can the actual gradient at the geotextile interface be defined?
2. Can a method be formulated to calculate this actual gradient under the relevant hydraulic conditions (rough horizontal bed, uniform open channel flow)?
3. Is it possible to verify this approach with the use of measured data?
4. Are there other field of applications for which this approach can be used, and how can this be realized?

1.4 Thesis outline

This research report is divided into eight chapters. Chapter 2 delves into the theoretical background and provides relevant literature for the detailed examination of the stability for geotextiles. Chapter 3 presents an in-depth explanation of an approach to find the actual gradient. In chapter 4, the approach is tested with measured data. The findings obtained from these tests are extensively discussed in chapter 5. Chapter 6 demonstrates the design method for a fictional case. Chapter 7 serves as the concluding section, where the research objective is evaluated and all research questions are thoroughly addressed. Additionally, chapter 8 explores further research directions and potential areas for expanding on the findings of this research project.

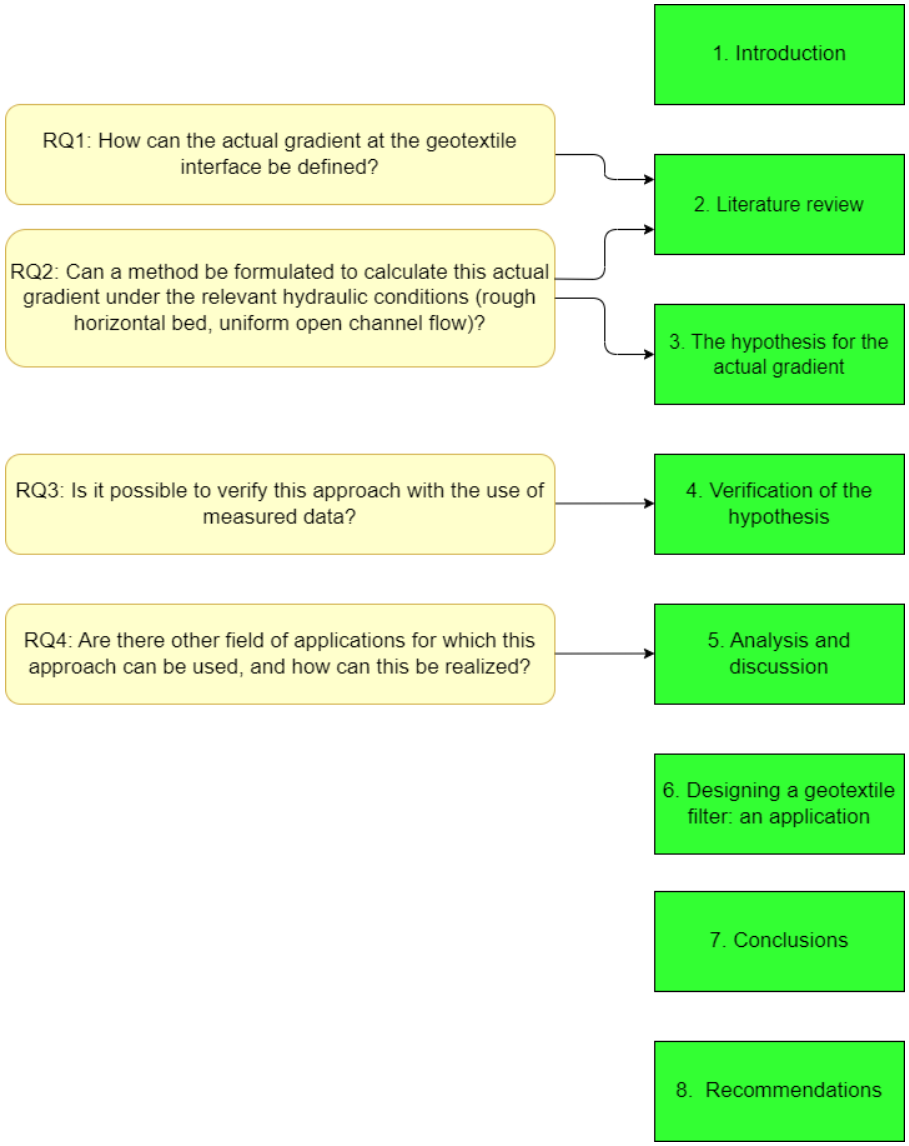

Figure 1.1: Overview of the report with research questions.

2 Literature review

In this chapter a review is given of the hydrodynamic processes that contribute to the pressure above the armored filter layer. Special attention is paid to the wave-induced pressure described by linear wave theory. Next, the stone stability of the grains is discussed. Therefore, the difference between the mean forces and fluctuating forces are presented. The concept of the pressure spectrum, combined with previous studies done within this research area are described in detail. The porous flow inside the filter layer are also elaborated. Finally, the general criteria of stable granular open filter constructions is presented with past design methods discussed.

In this report, we utilize the following coordinate system: the x, y, and z directions represent the streamwise, upward, and transverse coordinates, respectively, while u, v, and w represent the velocity components in their respective directions.

2.1 Design criteria for geotextiles

The two main criteria for the design of a geotextile filter are the retention and permeability criteria (Khan et al., 2022). Several additional conditions are required to ensure a proper design of geotextile filters. Additional conditions like clogging, durability, and survivability are mentioned in literature (PIANC 113, 2011; Lama et al., 2021). However, the retention and permeability criteria must be specified for each case where geotextile is located between the granular armour layer and the sandy base material. If the difference in grain size between the base layer and armour layer is too large, then another filter layer can be placed in between them, see figure 2.1.

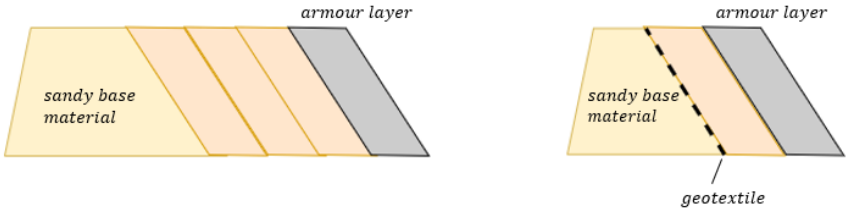

Figure 2.1: Geotextile replacing several filter layers between the base material and armour layer.

Retention criteria

The retention criterion indicates the maximum grain size that could migrate through geotextile, often presented as O_{95} (Kalore and Babu, 2022). As for granular filters, the sandtightness depends on the relation between the properties of the base material and the holes in the filter textile. According to EN12956, a reverse sieve test can be performed with appropriate sand to characterize the openings of the textile. The particle size distribution of this sand is determined after washing through a single layer of the geotextiles used as a sieve, without load. The characteristic opening size, O_{90} or O_{95}, corresponds to a specified size of the granular material that passed. Therefore, sand is washed through a sample of geotextile in a standard sieving machine. The distribution of the material passing through the geotextile is determined, and for example the d_{90} of the passed fraction determines the O_{90} of the geotextile. Other tests to characterize grain sizes or opening sizes are also found in the literature. For instance, Moraci et al. (2012) have proposed retention criteria based on Monte Carlo simulation considering the internal stability of broadly graded soils.

$$O_{95} \leq \alpha d_y \tag{2.1}$$

where O_{95} is the opening size of the filter, d_y is grain size corresponding to y percent passing, and α is retention ration. In PIANC 113 (2011), the stability rule for stationary flow through geometrically closed geotextiles is:

$$O_{90} < 2 \cdot d_{90B} \tag{2.2}$$

The filter works on the principle of self-filtration, as shown in figure 2.2, where the coarser grains are retained by the filter, and the coarser grains retain the finer grains by forming a stable skeleton structure, also commonly known as bridging structure (Giroud, 2010; Weggel and Ward, 2012).

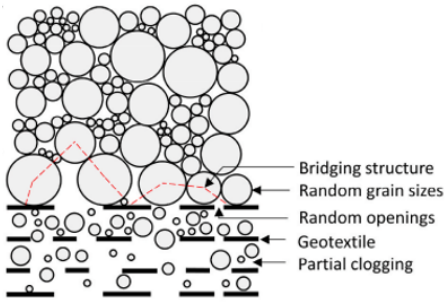

Figure 2.2: Schematic of geotextile filtration process (Kalore and Babu, 2022).

Permeability criteria

The permeability criteria applies to the flow requirement such that it allows water to pass through the geotextile to prevent pressure build-up. In order to meet this condition, the permeability of geotextile must be greater than the permeability of the subsoil. In PIANC 113 (2011) it is stated that the permeability of the geotextile should be more than 10 times larger than that of the subsoil. One way to measure the permeability of a geotextile is using the Darcy-type relations. Also, the permittivity parameter is often applied to specify the permeability of geotextiles:

$$P = \frac{u_f}{\Delta h} = \frac{k}{e} \tag{2.3}$$

in which Δh is the head difference, e is the thickness of the geotextile and k the "normal" permeability coefficient. P can be seen as the permeability per m thickness of geotextile and is a property of the material, regardless of the thickness of the geotextile.

Other criteria

Retention and permeability are the main criteria for the design of geotextile filters, but additional criteria which could affect the performance of the geotextile must be taken into account. There are two phenomena that can reduce the permeability of the geotextile: blocking and clogging. Blocking occurs when large particles seal the openings in the textile. The result is an enormous decrease in permeability. It must be noted that not every type of textile is equally sensitive to this phenomenon. The effect of (very) fine particles trapped inside the openings of the textile could also decrease the permeability. This phenomenon is called clogging. Clogging typically is time-dependent while blocking may occur in a very short span of time (Schiereck, 2012). Clogging, theoretically, stabilizes at a certain level after some time has passed. However, not much experimental evidence is available to support this theory. Also, it must be noted that clogging does not only occur in geotextiles, but also occurs in granular filters.

Another important condition to be met is the execution method of the geotextile. It should be avoided at all cost that during the execution phase the geotextile is damaged due to placing of cover layers. The drop height during the dumping of stones should therefore be restricted to 2.0 m (CUR, 2000). If this is not possible, the geotextile should first be covered with a protective layer of gravel to prevent damage. This study assumes that the geotextiles have been installed without damages. In general, geotextiles are quite durable when they are completely submersed. However, when partly exposed to the open air, for example in the splash zone on a slope protection, the lifespan reduces considerably. For geotextiles consisting of natural fibers this is even less, which makes it less attractive to use.

2.1.1 Natural geotextiles/ Lemmens (1996)

Lemmens (1996) pioneered in searching for a natural material as a substitute for geotextile as bed protection. Figure 2.3 shows the test set-up used by him in that year.

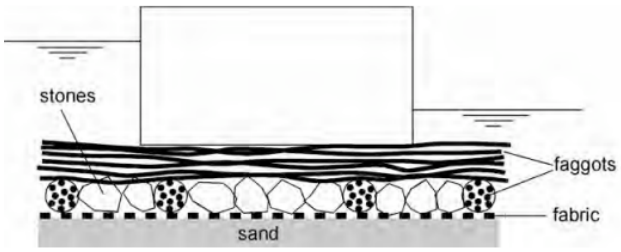

Figure 2.3: Filter tests for nature friendly fascine mattress (Schiereck, 2012).

In his experiments he investigated the critical gradient for various natural fabrics. By varying the water level, the pressure head can be measured. For each fabric, next, with the occurrence of erosion of the sandy base a critical value can be determined. He then found that jute with 4cm woodpulp can withstand the same gradient as synthetic geotextile, see figure 2.4. For bed protection this could potentially be a good alternative. Natural fibers such as jute or coconut can be found in many places. A disadvantage of natural fibers is that the lifespan of the product is usually not more than a few months when applied on a slope in the air-sunshine zone (Schiereck, 2012). Obviously, this is different when the natural fiber is fully submersed. Due to the absence of sufficient experimental data no firm theory has been formulated.

Nr.	Type of fabric	Critical gradient (%)
1	None (classical fascine mattress)	7
2	Synthetic geotextile (not penetrable for roots)	59
3	Synthetic geotextile (penetrable for roots)	16
4	Reed (classical filter cloth in fascine mattresses)	18
5	Coconut fibre cloth	12
6	Coconut fibre cloth filled with 4 cm of woodpulp	14
7	Jute cloth	26
8	Jute cloth filled with 4 cm of woodpulp	56

Figure 2.4: Critical gradient for various types of filters (Schiereck, 2012).

2.2 Pressure-induced hydrodynamic processes above the filter layer

Hydrodynamic processes involve the study of the motion and behavior of fluids, including water. In this section, the hydrodynamic processes that induce pressure at the bottom of the flow are presented. The relevant theory of physics as well as the current state of knowledge will be introduced. This section presents a concise review of the linear wave theory; for in-depth theoretical aspects see Holthuijsen (2007). The wave-induced pressure which derived from linear wave theory receives special attention when discussing the new design method. Other influences, such as wind-induced pressure, dissipation or non linear waves will not be presented in this paper. For an extensive background of these effects see also Holthuijsen (2007).

2.2.1 Linear wave theory

Linear wave theory is a useful tool for the study of surface gravity waves. To apply this theory, certain assumptions must be made. Firstly, the amplitudes of the waves must be small compared to the wavelength and water depth, which is known as the small-amplitude approximation. Additionally, the water is assumed to be an ideal fluid, incompressible and with no viscosity. The third assumption is that the water is subject only to the external force of gravity, with wind-induced pressure and other external forces excluded. The linear theory provides analytical expressions for particle velocities and wave-induced pressure, which are used to describe wave characteristics such as phase speed and energy. The linear wave theory should not be used for steep waves or waves in very shallow water. For these waves, nonlinear theories are available, such as the Stokes wave theory.

The linear theory of surface gravity waves that is considered in this study applies, strictly speaking, only to water with idealised physical properties and motions, and also allowing for gravitation as the only external force. These assumptions lead to two fundamental equations: a mass balance equation and a momentum balance equation.

From the boundary condition mentioned in Holthuijsen (2007), the solution then is one equation of propagating harmonic wave in the positive x-direction:

$$\eta(x,t) = \alpha sin(\frac{2\pi}{T}t - \frac{2\pi}{L}x) \quad or \quad \eta(x,t) = \alpha sin(\omega t - kx) \tag{2.4}$$

where α is the amplitude of the wave, T is the wave period and L is the wave length. Above a sine wave is chosen, but it might as well have been a cosine wave since it would have made no difference except a phase difference of 90 degrees. The relation between the radian frequency ω and wave-number k can be specified with the dispersion relation:

$$\omega^2 = gk \cdot \tanh kh \tag{2.5}$$

This relation will be important for the transformation of the spectrum discussed in the next paragraph. The orbital motion of the water particles under a harmonic wave differs for deep and shallow water. As can be seen in figure 2.5, in deep water, the motion of the water particles is unaffected by the bottom. Only the magnitude of the motion reduces. Whereas in shallow water, these particles are also influenced by the bottom.

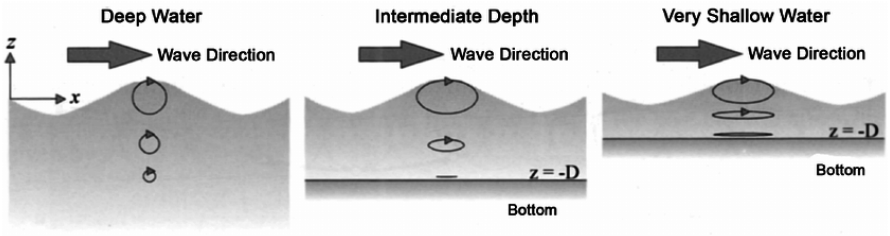

Figure 2.5: The orbital motion in deep water, intermediate-depth water and very shallow water (Holthuijsen, 2007).

The particle velocity of these motions can be derived in eq. (2.6) and (2.7). Note that the y-direction is not mentioned since the velocity in the y-direction is zero. The long-crested, harmonic wave extends only in the (positive) x-direction:

$$u_x = \hat{u}_x sin(\omega t - kx) \quad \text{with} \quad \hat{u}_x = \omega a \frac{cosh[k(h+z)]}{sinh(kh)} \tag{2.6}$$

$$u_z = \hat{u}_z cos(\omega t - kx) \quad \text{with} \quad \hat{u}_z = \omega a \frac{sinh[k(h+z)]}{sinh(kh)} \tag{2.7}$$

Wave-induced pressure

These motions of water particles in circles or ellipses imply accelerations that can be caused only by forces acting on these particles. They are developed by gradients in the wave-induced pressure. The analytical expression for this pressure is derived by substituting the solution for the harmonic wave expressed in the velocity potential into the Bernoulli equation, with the result that the total pressure is:

$$p = -\rho g z + \rho g a \frac{cosh[k(h+z)]}{cosh(kh)} sin(\omega t - kx) \tag{2.8}$$

The first term on the right-hand side in eq. (2.8) is the hydrostatic pressure. This term is independent of the presence of waves in linear approximation. The second term is due to the waves and therefore represents the wave-induced pressure, denoted as p_{wave}:

$$p_{wave} = \hat{p}_{wave} sin(\omega t - kx) \qquad with \qquad \hat{p}_{wave} = \rho g a \frac{cosh[k(h+z)]}{cosh(kh)} \tag{2.9}$$

Thus the gradient under pressure waves is as follows:

$$i = ka \frac{cosh[k(h+z)]}{cosh(kh)} cos(\omega t - kx) \tag{2.10}$$

2.2.2 Wave spectrum

This section presents a concise review of the wave spectrum literature. For an extensive theoretical background, see Holthuijsen (2007) or Bendat & Piersol (1971). A description of harmonic wave components can be given by using linear wave theory. To summarize briefly, a large number of these harmonic components can give a description of the random motion of the sea-surface. At first, a wave record is considered which has a surface elevation η at one location as a function of time with duration D. Sampling of a function in space is entirely analogous to sampling a time function, meaning that period T is replaced by wavelength λ, and frequency f is replaced by wave-number k (Vermeer, 2012). By reproducing the wave record several times, it results in a sum of a large number of harmonic wave components, also known as a Fourier series:

$$\eta(t) = \sum_{i=1}^{N} a_i cos(2\pi f_i t + \alpha_i) \quad \text{or} \quad \eta(x) = \sum_{i=1}^{N} a_i cos(k_i x + \alpha_i) \tag{2.11}$$

where a_i and α_i are the amplitude and phase, respectively, of each frequency $f_i = i/D$ or wave-number k_i ($i = 1, 2, 3...$; the frequency interval is therefore $\Delta f = 1/D$). The amplitudes and phases are random variables, which are precisely defined with their probability density function. The summation of these many harmonic waves, with constant but randomly chosen amplitudes and phases, creates a random sea-surface, see figure 2.6. From this random sea surface, the values of the amplitude and phase for each frequency can be determined with a Fourier analysis that would give the amplitude and phase spectrum for this wave record. This is called the random-phase/amplitude model.

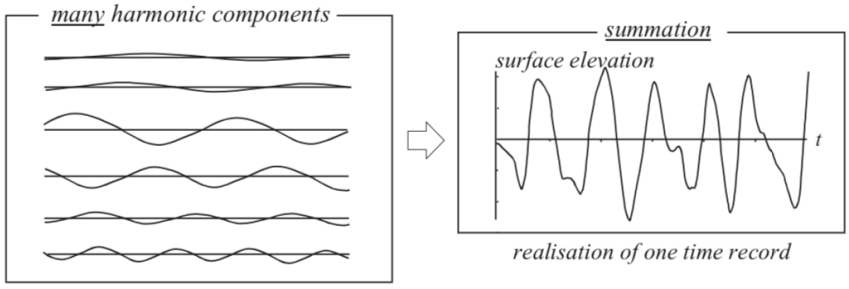

Figure 2.6: The summation of many harmonic waves creates a random seas surface (Holthuijsen, 2007).

For harmonic waves, the phase at each frequency is uniformly distributed between 0 and 2π and the amplitude is Rayleigh distributed. Sometimes it is more convenient to consider the variance spectrum instead of the amplitude spectrum. The main reason is that the variance density spectrum provides a description in a physical sense when multiplied with ρg. This results in the energy density spectrum and shows how the energy of the waves is distributed over the frequencies. By introduction of the variance in this way a link is available to physical properties such as wave-induced pressure variations.

The variance of the surface elevation, $\eta(t)$, by definition is the average of the squared surface elevation $\overline{\eta^2}$. For a harmonic wave with amplitude a, the variance is $\overline{\eta^2} = \frac{1}{2}a^2$. In the random-phase/amplitude model for random waves, a large number of harmonic waves is added and the variance of this sum is equal to the sum of the individual variances:

$$variance = \overline{\eta^2} = E\left\{\eta^2\right\} = \sum_{i=1}^{N} E\left\{\frac{1}{2}a_i^2\right\} \tag{2.12}$$

Since both spectra (amplitude and variance) are based on discrete frequencies and Nature does not select such discrete frequencies, the variance density spectrum must be modified to be continuous so that all frequencies can be present. This is done by letting the width of the frequency band Δf_i approach zero:

$$E(f) = \lim_{\Delta f \to 0} \frac{1}{\Delta f} E\left\{\frac{1}{2}a^2\right\} \tag{2.13}$$

If, for instance, a small part of the spectrum for this Fourier mode is taken, then the variance can be described as illustrated in figure 2.7, where the total variance $\overline{\eta^2}$ of the surface elevation is the sum of the variances of all frequency bands:

$$\overline{\eta^2} = \int_0^\infty E(f)df \tag{2.14}$$

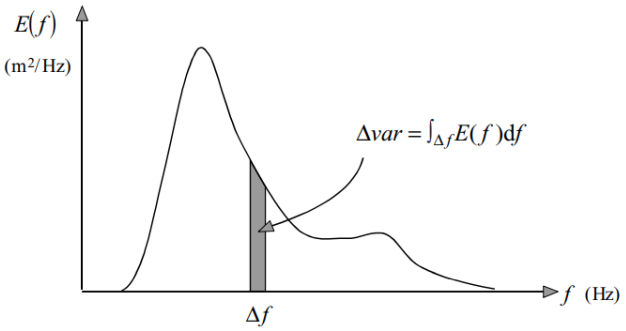

Figure 2.7: Variance density spectrum (Holthuijsen, 2007).

The above theory is explained in terms of the frequency f, but it can equally well be formulated in terms of the radian frequency $\omega = 2\pi f$. The total variance should be conserved for the corresponding spectrum transformation. Under the condition that the integral is conserved a (one-dimensional) Jacobian J is used. As an example, the transformation from a frequency spectrum to the radian frequency spectrum is given. In this case, the Jacobian $J = \frac{1}{2\pi}$ is used:

$$\overline{\eta}^2 = \int_0^\infty E(\omega)d\omega = \int_0^\infty E(f)df \tag{2.15}$$

from which the transformation can be achieved by taking:

$$E(\omega) = E(f) \cdot \frac{df}{d\omega} = E(f) \cdot \frac{1}{2\pi} \tag{2.16}$$

2.3 Stability of loose non-cohesive grains

In this section the stability of loose grains, like gravel or rock, is presented. The situation describes an uniform parallel flow on a horizontal bed and is based on the theory described in Schiereck (2012). For an extensive theoretical background of non-equilibrium turbulent flow reference is made to Hofland (2005) or Hoan (2008).

2.3.1 Basic equations

To understand the stability of loose grains, it is necessary to know which forces make a stone moving. Figure 2.8 gives an illustration of the important forces acting on a grain. The various flow forces that will initiate a motion of a grain are:

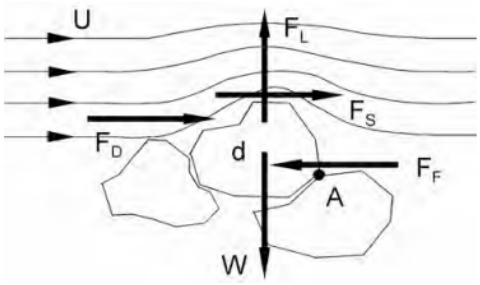

Figure 2.8: Forces on a grain in flow (Schiereck, 2012).

$$\left.\begin{array}{ll} Drag force: & F_D = \frac{1}{2} C_D \rho_w u^2 A_D \\ Shear force: & F_S = \frac{1}{2} C_F \rho_w u^2 A_S \\ Lift force: & F_L = \frac{1}{2} C_L \rho_w u^2 A_L \end{array}\right\} F \propto \rho_w u^2 d^2 \tag{2.17}$$

in which C_i are coefficients of proportionality and A_i form the exposed surface area. From eq. (2.17) can be seen that the surface of a grain is proportional to the square of a representative size d of the grain. This simplifies the derivation of the load, since it can be expressed in one term as shown in eq. (2.17).

There is a critical value of the flow velocity at which the forces on a grain are no longer in equilibrium and the grain starts to move. This means that when the forces are in equilibrium, the grain will not move. The equilibrium of forces is represented in the formula below:

$$\left.\begin{array}{ll} \sum H = 0: & F_D + F_S = F_F \\ \sum V = 0: & F_D = W \\ \sum M = 0: & F_D \cdot O(d) + F_S \cdot O(d) = W \cdot O(d) \end{array}\right\} \rho_w u^2 d^2 \approx (\rho_s - \rho_w) g d^3 \tag{2.18}$$

From eq (2.18) the following relation can be deducted. It must be noted in this case the critical velocity u_c is applied as a stability parameter.

$$u_c^2 \approx (\frac{\rho_s - \rho_w}{\rho_w}) g d = \Delta g d \rightarrow u_c^2 = K \Delta g d \tag{2.19}$$

Two pioneering names are connected with the analysis of the stability of stones in flowing water: Izbash and Shields. Izbash (1931) defined a value for the K-factor from his experiments. There is no influence of depth in his formula. Furthermore, the diameter of the stone and the location of the velocity are not well defined. However, it is still a good tool for a first approximation in cases where the velocity near the bottom is known. The formula is given here:

$$\Delta d = 0.7 \frac{u_c^2}{2g} \tag{2.20}$$

Shields

The other stability relation for uniform flow conditions has been a contribution by Shields (1936). In eq. (2.21), the relation is given between a dimensionless shear stress and the particle Reynolds-number:

$$\Psi_c = \frac{\tau_c}{(\rho_s - \rho_w) g d} = \frac{u_*^2}{\Delta g d} = f(Re) = f(\frac{u_* d}{\upsilon}) \tag{2.21}$$

in which Ψ_c is usually called the Shields parameter; this is a stability parameter which is defined using a critical value of the (shear) velocity. Figure 2.9 shows an illustration of the Shields relation. For high Re_* numbers, Ψ_c is no longer dependent on Re_* and becomes constant with a value of about 0.055. Van Rhijn (1984) replaced the Re_* by a dimensionless particle diameter d_* in his presentation of the Shields relation. This has the advantage of avoiding iteration of u_{*c}. Another practical advantage is that Ψ_c becomes a constant for d = 6-7 mm, depending on ρ and ν. This implies that for usual bed protections, Ψ_c can be used as a constant, which avoids iteration of the diameter in Shields curve. An important conclusion is that no scale effects will be present in tests when the stone size exceeds 6-7 mm.

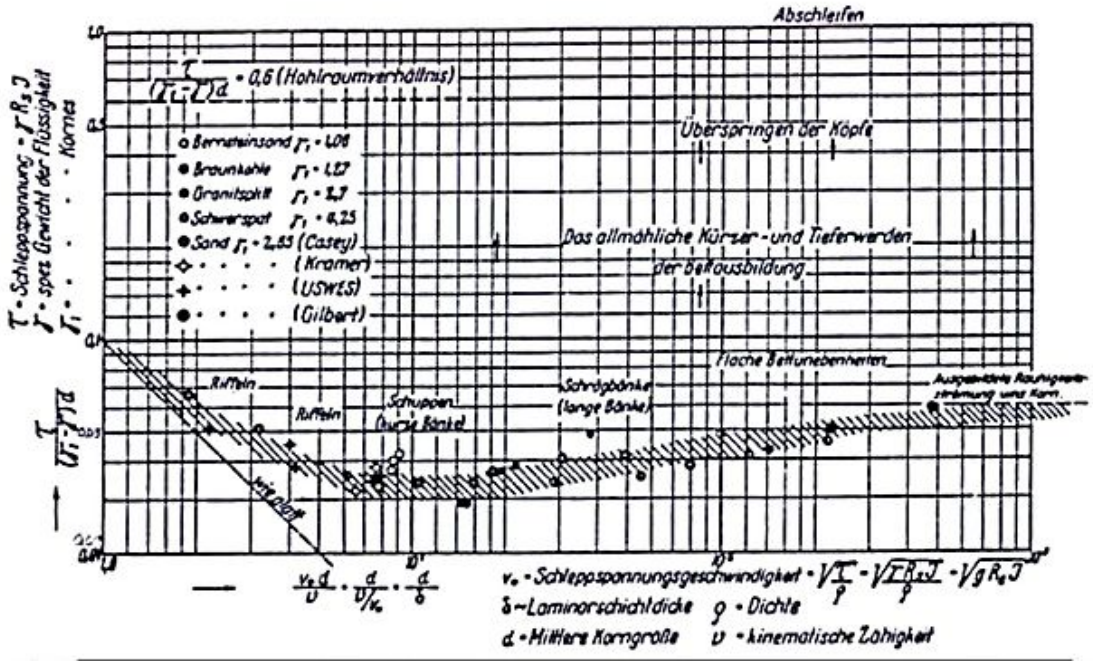

Figure 2.9: Critical shear stress according to Shields (Shields, 1936).

A more practical formula can be derived from the Shields relation by replacing the shear velocity by a mean velocity assuming Chézy. Note that, via C, the water depth is implicitly given in the relation as a bottom roughness, C increases with the water depth: $C = 18log(12R/k_r)$, in which k_r is the so-called equivalent sand roughness.

$$\Psi_c = \frac{\overline{u}_c^2 g}{\Delta g d_{n50} C^2} \rightarrow d_{n50} = \frac{\overline{u}_c^2}{\Psi_c \Delta C^2} \tag{2.22}$$

2.4 Rough wall flow

This section intends to describe the theory on uniform flow on rough walls. Also, the rough wall turbulent boundary layer pressure spectrum and presents studies that discuss these pressure spectra are described in this section. For an extensive review of the theoretical background of turbulent flow at a rough bed the reference is Hofland (2005) or Detert (2008).

2.4.1 Uniform flow

The flow in an open channel is considered uniform when its properties remain constant throughout the channel, including the depth of flow, area of flow, rate of flow, and velocity of flow. In this type of flow, the water moves steadily and consistently, without significant changes in velocity or depth over long distances. The average slope, or average gradient, represents the rate of elevation change per unit distance in an open channel with uniform flow. As water flows along the channel, the slope of the channel causes a continuous conversion of potential energy into kinetic energy, both in the main flow and in turbulent eddies. This energy transformation eventually dissipates as heat. Figure 2.10 illustrates the equilibrium that exists between the bottom shear stress and the fluid pressure component acting on the slope. A pressure gradient exists which overcome the shear resistance and causes the fluid to flow.

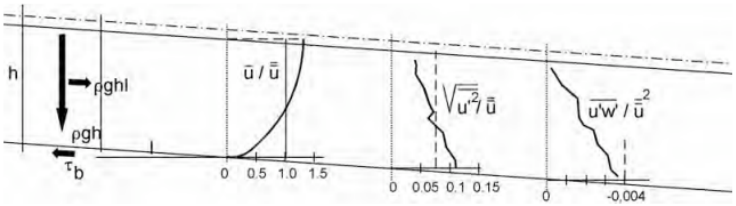

Figure 2.10: Uniform flow (Schiereck, 2012).

As can be seen from figure 2.10, the bottom shear stress can be written as eq. (2.23). The shear stress is directly proportional to the flow velocity, indicating a relationship between shear stress and flow resistance as described by equation (2.23):

$$\tau_b = \rho g h i = c_f \rho u_0^2 = \rho u_*^2 \tag{2.23}$$

in which i is the gradient and c_f is a dimensionless friction coefficient. Based on the Chezy coefficient, the empirical relation is used to describe the average velocity u_0. For an infinitely wide channel the water depth h is used; otherwise the hydraulic radius R should be used.

$$u_0 = C\sqrt{Ri} \quad \text{with :} C = \sqrt{\frac{g}{c_f}} \tag{2.24}$$

From eq. (2.23) and (2.24) the shear velocity u_* can be derived:

$$u_* = u_0\sqrt{g}/C = u_0 \cdot \sqrt{c_f} \tag{2.25}$$

For this study it is important to remember the equilibrium between the bottom shear stress and the fluid pressure component on the slope (eq. (2.23)). The gradient, representing the rate of elevation change per unit distance, influences the flow dynamics and the distribution of pressures within the open channel. Pressure variations arise as a result of the interaction between the flow velocity, shear stress, and the geometry of the channel. The average gradient can be written as follows:

$$\bar{i} = \frac{\tau_b}{\rho g h} \tag{2.26}$$

2.4.2 Flow around a rough bed

In practice, flow is never uniform. Accelerations and decelerations influence the boundary layer and the turbulence in the flow. The flow around a rough bed is therefore turbulent. Booij (1998) states that pressure fluctuations caused by turbulent eddies could contribute considerably to the forces that initiate motion of bed particles. These pressures can also act on smooth walls and are known as turbulent wall pressures (TWP). The equation for these pressure fluctuations in turbulent flow is derived by taking the divergence of the momentum equation, using the continuity equation to drop terms, performing a Reynolds decomposition into mean and unsteady terms, and then subtracting the time-averaged equation. In this paper only the Poisson equation is given, for an extensive derivation see Barba (2013) or Veldman (2013).

The wall pressure can be characterized as the pressure fluctuations on the bed, and can be obtained by solving the Poisson equation for fluctuating pressure, p'. Within an incompressible flow this reads (in Reynolds decomposition, e.g. Chang III et al., 1999) as follows:

$$\nabla^2 p' = -2\rho \frac{\partial \overline{u}_i}{\partial x_j} \frac{\partial u'_j}{\partial x_i} - \rho \frac{\partial^2 (u'_i u'_j - \overline{u'_i u'_j})}{\partial x_i \partial x_j} \tag{2.27}$$

where $i, j = x, y, z$. The first term on the right-hand side represents the mean shear-turbulence interaction and the second term the turbulence-turbulence interaction (Y.-T. Lee et al., 2005). One way to examine the regions of turbulence activity which contribute to the production of surface pressure is reviewing the solutions of the Poisson equation for pressure fluctuations in experiments that measure the pressure spectrum.

2.4.3 Frequency range

The theory follows a two-layer model: a slowly rising low-frequency region and a rapidly decaying high-frequency region (Blake, 2017). Both regions overlap in the slowly decaying mid-frequency region. This two-layer model, its expected power laws and the overlapping region, have been investigated by numerous researchers (Blake, 2017; Farabee and Casarella, 1991; Gravante et al., 1998; Hofland, 2005; Varano, 2010; Meyers et al., 2015; Jiao et al., 2022). Next, Meyer et al. proposed the triple scaling hypothesis, which states that the rough-wall-pressure spectrum can be divided in three independent scaling regions. The majority of these studies involve smooth-wall-pressure spectra followed from measurement in other fields of application, such as naval and accoustical

ones. In the literature the general form of the scaled spectrum can be described in the following relation (Joseph et al., 2020):

$$\frac{\Phi(\omega)U}{P^2L} \quad \text{versus} \quad \frac{\omega L}{U} \tag{2.28}$$

in which $\Phi(\omega)$ is the pressure spectral density. The length scale L, velocity scale U and pressure scale P were chosen differently by various researchers. The data collected from the measurements cover a broad frequency range. From the collected data, the scaling behavior of the various spectral regions of the wall pressure field can be examined. In this literature these regions can be delineated by the scaling behavior that collapses the data. In the low-frequency region the two most well-known scalings are the classical smooth-wall scaling and the mixed-outer scaling of Blake (1970). These were originally developed for scaling the smooth-wall-pressure spectrum, but because of the assumption of wall similarity have been extended to rough-wall flows (Joseph et al., 2020). For the high-frequency region Blake stated that the length scale that can be used to collapse the high-frequency part of the rough wall spectrum is the roughness height rather than the viscous length scale (Hofland, 2005). The region where both the low- and high-frequencies overlap is scaled on both inner and outer variables.

In a turbulent wall pressure spectrum, the outer scaling variables and inner scaling variables are related to the boundary layer and represent the different length scales within the flow. The outer variables typically capture the large-scale structures or fluctuations in the flow, which are primarily influenced by the outer region of the boundary layer. These variables are associated with the larger eddies occurring withing the flow field. Conversely, the inner scaling variables focus on the small-scale structures or fluctuations in the flow, which are primarily influenced by the inner region of the boundary layer. These variables are associated with smaller eddies and turbulent motions that manifest in closer proximity to the wall. The differentiation between these scaling variables helps in understanding and analyzing the turbulent characteristics of the wall pressure spectrum at different length scales within the boundary layer.

2.4.4 Past studies

Wall-pressure spectra for equilibrium flows have been studied experimentally and with numerical simulations for many years. The greatest part of these experiments has been implemented in others fields of application (e.g. naval and accoustical). However, numerous aspects are relevant for our research. The area of contact between the flow and solid wall are smooth or rough. This paper focuses on rough walls, since the bed layer on top of the geotextile consists of granular material. However, some characteristics of a smooth wall show similarities with a rough wall. In this section those past studies are presented, which are of importance for describing rough-wall pressure spectra.
Farabee and Casarella (1991) performed experimental measurements of the frequency spectra of the wall pressure fluctuations below turbulent boundary layers in a low-noise flow facility. The experiments conducted in those researches are based on an equilibrium turbulent boundary layer flow, which has been examined most frequently. Experimental measurements are effective in acquiring data of wall pressure fluctuations (Jiao et al., 2022). Another approach for investigating the wall pressure fluctuations is numerical simulation. Lee & Sung (2002) described the characteristics of wall pressure fluctuations in separated and reattaching flows over a BFS (Backward-Facing Step) in a wind tunnel. The flow pattern then becomes a non-equilibrium flow. Hofland (2005) did experiments with a BFS in an open-channel flow and compared the results of Lee & Sung with his own tests. Meyers *et al.* (2015) extended the existing database of boundary-layer fluctuating pressures measurements and introduces the triple scaling hypothesis.

Blake (1970)

In 1970 Blake did research on the turbulent boundary-layer wall-pressure fluctuations on smooth and rough walls. He performed his experiments with microphones in an accoustic wind tunnel and he compared the wall-pressure measurements on smooth and rough walls. He concluded that the high-frequency pressure levels are determined by length and velocity scales characteristics. For the rough walls these scales are respectively the average geometric height $\bar{k_g}$ and the friction velocity U_τ. For the smooth wall they are respectively ν/U_τ and U_τ. Blake proposed the following two relations for rough walls:

$$\frac{\Phi(\omega)U_\infty}{\tau_w^2\delta^*} \quad vs. \frac{\omega\delta^*}{U_\infty} \tag{2.29}$$

$$\frac{\Phi(\omega)U_\tau}{\tau_w^2 k_g} \quad vs. \frac{\omega k_g}{U_\tau} \tag{2.30}$$

in which eq. (2.29) presents the low-frequency scaling and eq. (2.30) the high-frequency scaling relation. Figure 2.11 refers to the high-frequency pressure levels for smooth wall pressure (a) and rough wall pressure (b). Other important parameters are the wall-pressure spectral density, $\Phi(\omega)$, dynamic head, q and the radian frequency, ω.

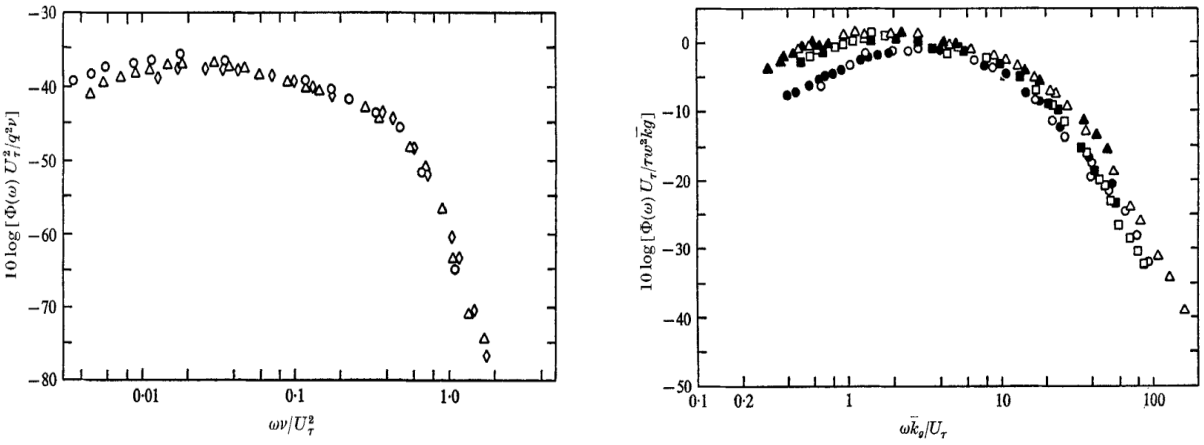

(a) Smooth wall pressure spectrum, inner variables.

(b) Rough wall pressure spectrum, inner variables.

Figure 2.11: Wall-pressure spectra scaled for high-frequency range (Blake, 1970).

The low-frequency region for both smooth and rough walls is illustrated in figure 2.12. Both walls are scaled on the free-stream velocity, U_∞, and displacement thickness layer, δ^*, as outer variables. In literature, sometimes another term is used for the free-stream velocity, namely, the edge velocity U_e (Meyers et al., 2015; Joseph et al., 2020).

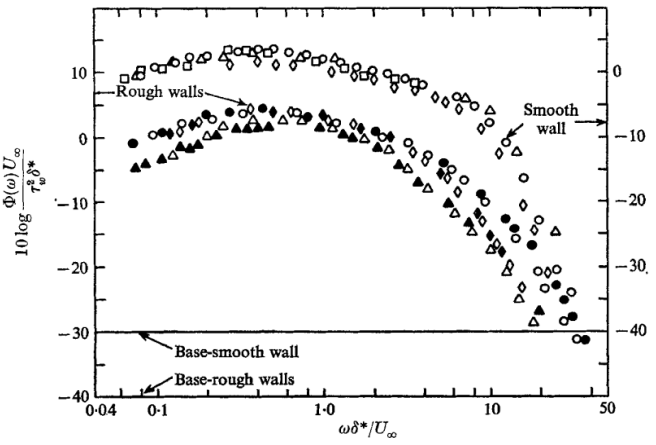

Figure 2.12: Wall-pressure spectra over smooth and rough walls, outer variable scaling (Blake, 1970).

For low frequencies the wall pressures under a rough boundary layer flow show the same scaling behavior as for the smooth wall in the frequency range $0.3 \leq \omega\delta^*/U_\infty \leq 2.5$.

Farabee and Casarella (1991)

Farabee and Casarella performed experiments for the measurement of the frequency spectra of the wall pressure fluctuations beneath a turbulent boundary layer in a wind tunnel. The data, taken over a range of flow velocities, display the pressure spectrum on dimensionless frequencies for smooth walls and each region can be given a certain range in which the spectrum is scaled.

In the low-frequency region ($\omega\delta/u_\tau < 5$) the spectrum collapse on the outer variables δ (boundary layer thickness), and u_τ. Although Blake described the displacement thickness layer as the length scale, other variables are also possible. Farabee and Casarella (1991) state that the scaling behavior in the low-frequency range will be different in pressurized flow, due to the different upper boundary. Therefore, the length scale h will be more appropriate than δ. The overlap region is scaled on both inner and outer variables ($100 < \omega\delta/u_\tau$ and $\omega\nu/u_\tau^2 < 0.3$). The high-frequency region is scaled on the inner variables ν, τ_w and u_τ for smooth walls and covers the high-frequency range ($0.3 < \omega\nu/u_\tau^2$). The difference with Blake is that the high-frequency region is scaled with the roughness height k instead of the viscous length scale (ν/u_τ).

Figure 2.13a illustrates the pressure spectrum scaled on the low frequencies by the boundary layer thickness, δ, and shear velocity, u_τ (outer variables). The inner variables that scale the pressure spectrum on the high frequencies are ν/u_τ and u_τ, see figure 2.13b.

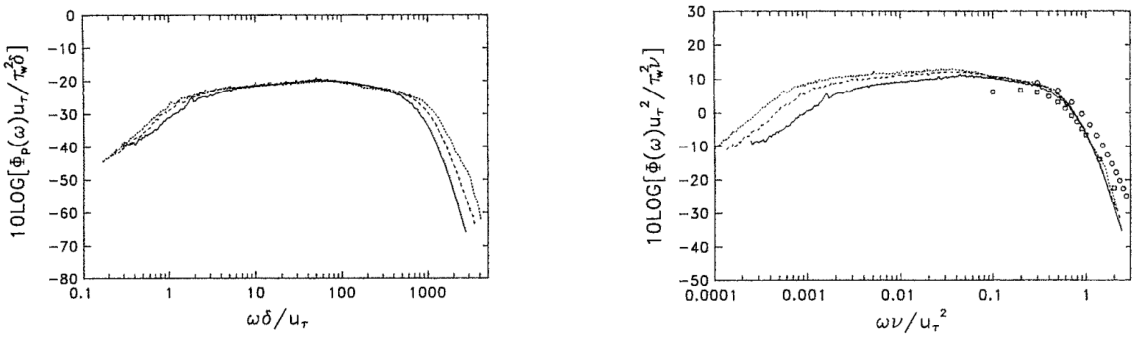

(a) Wall-pressure spectrum scaled on outer flow variables.

(b) Wall-pressure spectrum scaled on inner flow variables.

Figure 2.13: Wall-pressure spectra for smooth walls from wind tunnel measurements (Farabee and Casarella, 1991).

Lee & Sung (2002)

The experiments discussed so far (Blake, 1970; Farabee and Casarella, 1991) focused on the equilibrium turbulent boundary layer flow. Then, Lee & Sung described the characteristics of wall pressure fluctuations over a BFS (Backward-Facing Step) in a wind tunnel. The flow pattern in this approach separates and reattaches in streamwise location, resulting in a non-equilibrium flow. Figure 2.14 illustrates the pressure spectra at various locations.

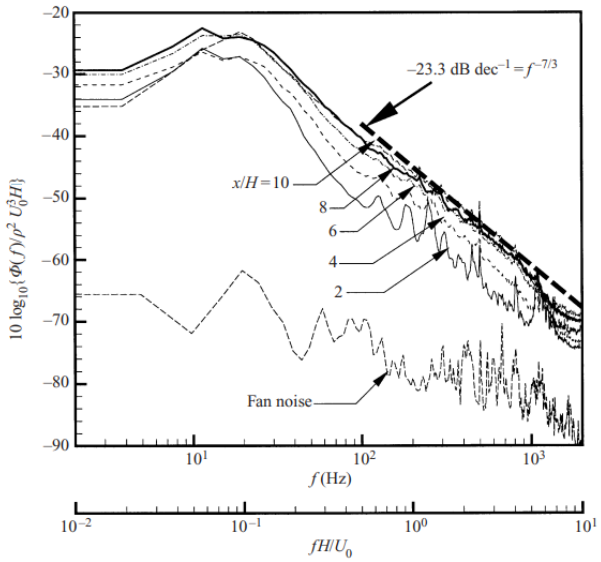

Figure 2.14: Spectra of pressure at different streamwise locations (I. Lee and Sung, 2002).

The scaling law can be defined as follows:

$$\frac{\Phi(f)}{\rho^2 U_0^3 H} \quad vs. \quad \frac{fH}{U_0} \tag{2.31}$$

in which the velocity scale is the free-stream velocity U_0.

Hofland (2005)

Hofland evaluated the presence of TWP-induced forces on rough-bed material by comparing the measurements of Lee & Sung (2002) with his own measurements of pressures on a rough bed behind a BFS. The combination of a smooth wall in his windtunnel experiments with a rough wall in the open-channel, gave Hofland the possibility to examine the origins of forces on the material. Figure 2.15 shows the comparison of spectra on a cube behind a BFS with a TWP from a smooth wall windtunnel experiment. In this way Hofland proved that the source for the high-frequency fluctuating pressures is indeed the turbulence generated by the outer flow, since the flow near the bed is completely different (Hofland, 2005). The low-frequency region, namely, does posses different characteristics. The reason is that the turbulence characteristics of an open-channel flow differ from those of an equilibrium boundary flow. The spectra for low frequencies should differ because the free surface influences the resulting pressures. This is not the case for high-frequencies because in both fields of application the TWP characteristics are generated by near-bed flow processes (Hofland, 2005).

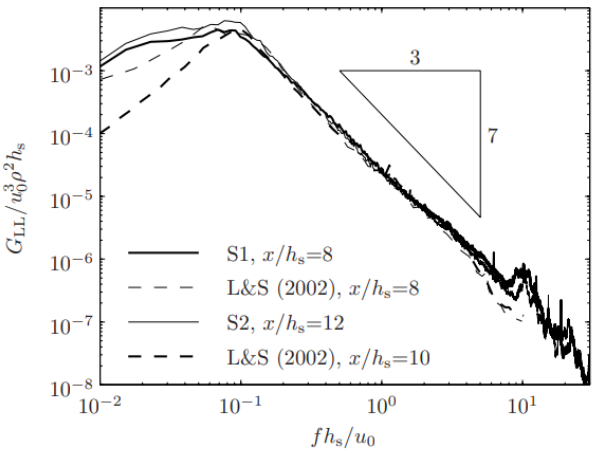

Figure 2.15: Comparison of spectra of pressures on a cube behind a BFS to TWP spectra from a smooth wall windtunnel experiment (Hofland, 2005).

As can be seen in figure 2.15, Hofland (2005) described the velocity scale u_0 as the average velocity on the step, whereas Lee & Sung presented the velocity scale as the free-stream velocity. The comparison between both experiments can be made because the step on which the average velocity is measured was smooth. The assumption was made that the average velocity could therefore be a suitable alternative.

Meyers *et al.* (2015)

Meyers *et al.* (2015) proposed the triple scaling hypothesis, which states that the rough-wall-pressure spectrum comprises of three independent scaling regions. This contrasts with the Blake model which consists of two regions that also overlapped. The extra region which Meyers *et al.* introduces is the mid-frequency region. Furthermore, he examined the applicability of various scaling as had been suggested by previous researchers. First, in the low-frequency region, the plot that correlates best with different rough-wall spectra is scaled as $\Phi(\omega)U_\tau/(\tau_w^2\delta)$ versus $\omega\delta/U_\tau$. This is in line with the pressure spectrum as scaled on outer flow variables of Farabee and Casarella (1991). At least for $20 \leq \omega\delta/U_\tau \leq 800$.

Secondly, in the mid-frequency region, the scaling given earlier by Blake's high frequency region correlates closely with various rough-wall pressure spectra. The extent of this region seems to reach out at least between $3 \leq \omega k_g/U_\tau \leq 20$ for the experimental cases that were considered by Varano (2010). Also, figure 2.16 show the pressure spectra plotted on a log-log scale in which for this frequency range a -4/3 slope can be seen.

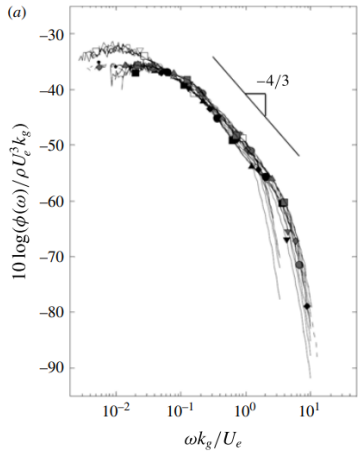

Figure 2.16: Pressure spectra scaled for the mid-frequencies (Meyers et al., 2015).

Thirdly, Meyers *et al.* concluded that at the highest frequencies the wall-pressure spectrum of both rough- and smooth-wall boundary layers has a universal viscous form: $\Phi(\omega)U_v^2/\tau_v^2\nu$ versus $\omega\nu/U_v^2$, in which U_v is the shear friction velocity and $\tau_v = \rho U_v^2$ (see figure 2.17). Since the scaling method of Blake does not contain any direct reference to viscosity, it is not surprising that his scaling shows no optimal collapse on the highest frequencies. Although Blake's scaling fails at the highest frequencies, it does show some clear signs of collapsing the spectra in the mid-frequencies $3 \leq \omega k_g/U_\tau \leq 20$.

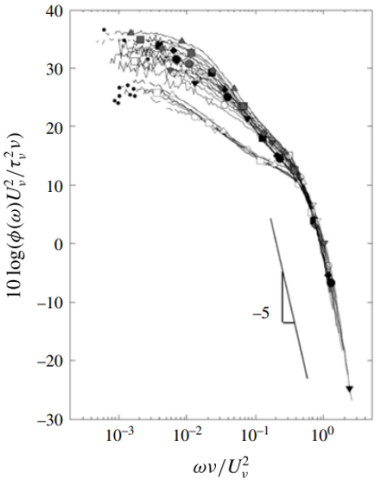

Figure 2.17: Pressure spectra scaled using the shear friction velocity (Meyers et al., 2015).

Overview and concluding remarks

Figure 2.18 provides an overview of the extensive research conducted on TWP and the distinct scaling characteristics identified by various researchers. Additionally, the figure presents the different wall conditions and the specific application fields in which the experiments were conducted. Based on this overview, it can be inferred that the pressure spectra proposed by Blake (1970) offer the most suitable depiction of the scenario presented in this study involving geotextiles. Blake's spectra demonstrate a representation for the rough wall conditions for both the low- and high-frequency regions. In this study, these conditions could correspond to the upper granular filter layer protecting the geotextile. Considering Blake's account of the rough wall experiments encompassing both low- and high-frequency regions, there exists a possibility to approach the fluctuating component from the TWP spectra.

Spectral region	Research	Velocity scale	Length scale	Pressure scale	Wall conditions	Field of application
Low-frequency	Blake (1970)	U_∞	δ^*	τ_w	Rough	Wind
	Farabee & Casarella (1991)	U_τ	δ	τ_w	Smooth	Wind
	Lee & Sung (2002)	U_∞	H	ρU_∞^2	Smooth	Wind (BFS)
	Hofland (2005)	U_0	h_s	ρU_0^2	Smooth	Water (BFS)
	Meyers *et al.* (2015)	U_τ	δ	τ_w	Smooth	Wind
Mid-frequency	Meyers *et al.* (2015)	U_e	k_g	ρU_e^2	Rough	Wind
High-frequency	Blake (1970)	U_τ	k_g	τ_w	Rough	Wind
	Blake (1970)	U_τ	ν/U_τ	q	Smooth	Wind
	Farabee & Casarella (1991)	U_τ	ν/U_τ	τ_w	Smooth	Wind
	Meyers *et al.* (2015)	U_v	ν/U_v	τ_v	Rough	Wind

Figure 2.18: Summary of pressure spectrum scalings.

2.5 Porous flow

In this section the porous flow through a granular medium is presented. The porous flow can either be laminar or turbulent depending on the Reynolds number. The flow direction can also be either perpendicular or parallel. In principle, flows in porous media are governed by the incompressible Navier-Stoke equations. The derivation of this equation is not discussed in here, but for an extensive review a reference is Holthuijsen (2007).

2.5.1 Forchheimer equation

The expression of the Navier-Stokes equation is valid for both laminar and turbulent flows. For turbulent flow, the values of velocity and pressure can be divided in an average value, $\bar{u}$, and a turbulent fluctuation, u'. This theory is called Reynolds decomposition and leads to the two-dimensional Navier-Stokes equation in Reynolds form for the x-direction:

$$\frac{\partial u}{\partial t} + u\frac{\partial u}{\partial x} + w\frac{\partial u}{\partial z} = -\frac{1}{\rho}\frac{\partial p}{\partial x} + \nu\frac{\partial^2 u}{\partial z^2} - \frac{\partial \overline{(u')^2}}{\partial x} - \frac{\partial \overline{u'w}}{\partial z} \tag{2.32}$$

in which u is the velocity in x-direction and w the velocity in z-direction. From eq. (2.32) the flow in a porous medium can be calculated, provided that every stone and every pore is taken into account (Schiereck, 2012). In practice, it is impossible to give an answer for the flow in such detail, but also not necessary. By averaging the equation, a practical solution can be found, see figure 2.19.

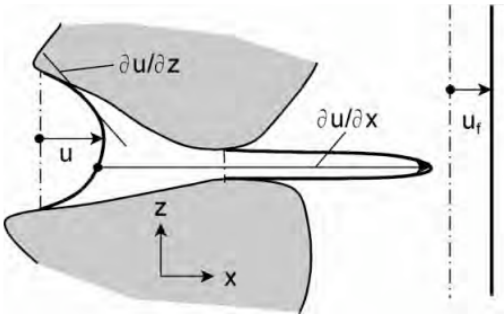

Figure 2.19: Velocities, gradients and averaging (Schiereck, 2012).

The averaging has to include enough pores to represent an average flow in a process which is of a random nature. The horizontal velocity u is defined as the filter velocity u_f when averaged over an area, dA:

$$u_f = \frac{1}{A}\iint u dA = n \cdot u \tag{2.33}$$

Finally, all square inertia and turbulence terms are combined into one quadratic friction term and the viscous gradient is replaced by a linear friction term (Van Gent, 1992):

$$\frac{1}{\rho g}\frac{\partial p}{\partial x} = i = a u_f + b u_f |u_f| + c\frac{\partial u_f}{\partial t} \tag{2.34}$$

with:

$$a = \alpha \frac{(1-n)^2}{n^3}\frac{\mu}{g d_{(n)50}^2} \tag{2.35}$$

and,

$$b = \beta \frac{(1-n)}{n^3}\frac{1}{g d_{(n)50}} \tag{2.36}$$

in which n is the porosity. For stationary flow ($\frac{\partial u_f}{\partial t} = 0$) this is the classical Forchheimer equation. In case of fine material, there occurs laminar flow through the porous medium. The relation between the gradient, i, and filter velocity, u_f, is linear, indicating that the relation is described by the first term of the right-hand side in the Forchheimer equation (eq. (2.34)). If the material is coarser, then the flow pattern is turbulent and the relation will be quadratic and the second term dominates. For material ranging in between both terms play a role (Schiereck, 2012).

2.5.2 Laminar flow

The flow inside a porous medium is laminar for $Re < 2000$ (Schiereck, 2012). Examples of laminar flow through porous media are usually flows in ground masses consisting of clay or sand. In laminar flow, the relation between the gradient and filter velocity is linear in the Forchheimer equation, reducing the eq. (2.34) to:

$$\frac{1}{\rho g}\frac{\partial p}{\partial x} = i = a u_f \tag{2.37}$$

Van Gent (1992) formulated the expression for the coefficient a (s/m). The dimensionless coefficient α has been determined experimentally, but for a first approximation $a \approx 1000$ can be used (Van Gent, 1992). Another way to present the pressures is in terms of heads:

$$h_p = z + \frac{p}{\rho_w g} \tag{2.38}$$

where h_p is the piezometric head and z the elevation above a reference level. Combining eq. (2.37) with eq.(2.38) gives the following relation in the x-direction:

$$u_f = -K_x \frac{\partial h}{\partial x} \qquad w_f = -K_z \frac{\partial h}{\partial x} \tag{2.39}$$

in which K_x (m/s) is the Darcy coefficient for permeability in the x-direction. The same steps can be taken for the z-direction. To compute the pressure and velocity distribution, the continuity equation must be taken into account. Combining Darcy and the continuity equation results in the Laplace equation, see eq. (2.40):

$$K_x \frac{\partial^2 h}{\partial x^2} + K_z \frac{\partial^2 h}{\partial z^2} = 0 \tag{2.40}$$

2.5.3 Turbulent flow

When the flow passes through coarse material, the flow is usually turbulent with $Re > 2000 - 3000$ (Schiereck, 2012). The concept turbulence describes the fluctuations in velocity and fluctuations in pressure in the porous medium. For coarser material, the relation between the gradient and filter velocity in the Forchheimer equation will be quadratic and the second term of eq. (2.34) dominates:

$$\frac{1}{\rho g}\frac{\partial p}{\partial x} = i = b u_f |u_f| \tag{2.41}$$

2.6 Stability of a granular filter

A granular filter can be used to protect the subsoil against erosion and scour. The design of a granular filter can be based on different criteria. Figure 2.20 presents the relation between strength and load in terms of the stability parameter I_c and the mobility parameter I, respectively. With reference to this figure two types of filters are discussed: geometrically closed and geometrically open filters. The latter can be distinguished in a stable and an unstable filter. In some specific scenarios some loss of material is accepted resulting in an unstable filter. Since the focus of this research lies on open filters, the two categories; closed and unstable open filters will be examined briefly.

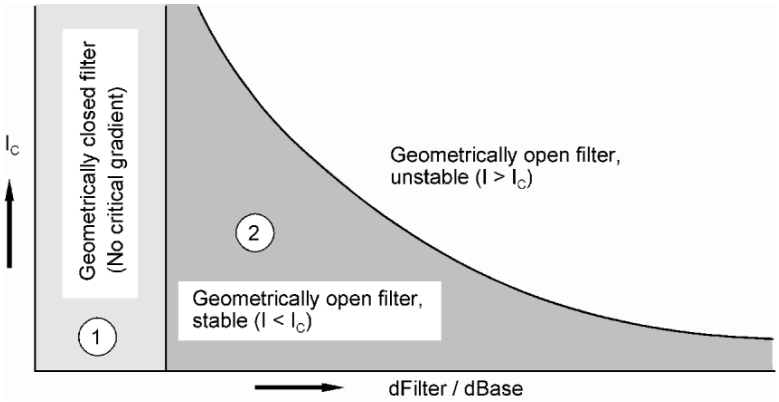

Figure 2.20: Design criteria for granular filters (Schiereck, 2012).

2.6.1 Geometrically closed filter

The stability of a geometrically closed filter depends on the geometrical properties of the filter materials. The size of the grains should be such that they cannot move in the filter. In this way finer grains cannot penetrate through the pores of the coarser grains. Geometrically closed filters are stable, regardless of the porous flow through the filter. They must fulfill the following conditions:

$$Stability: \quad \frac{d_{f15}}{d_{b85}} < 5 \quad Int.Stability: \quad \frac{d_{60}}{d_{10}} < 10 \quad Permeability: \quad \frac{d_{f15}}{d_{b15}} > 5 \tag{2.42}$$

A disadvantage of a closed filter is that the design could often lead to an uneconomical design, where multiple layers of granular filters are needed to satisfy the given conditions.

2.6.2 Geometrically open filter

In case of a geometrically open filter the size of the grains in the filter layer are much larger than those in the base layer. This allows grains of the base layer to move in and through the filter layer. However, erosion will only manifest itself when the load is higher than some critical value. The filter is stable when this critical value is larger than the load in the structure. Sometimes, loss of material is accepted within the limits of admissible settlements. In this scenario, the open filter is unstable and even larger quotients of filter and base diameters are allowed.

From the previous paragraph it is known that, based on the Forchheimer equation eq. (2.34), the gradient is either linear (laminar flow) or quadratic (turbulent flow). This depends on the filter velocity which in turn relates to the forces that have an impact on any grain ($F_f = \rho_w g i$). When the loading forces on a grain of the

base layer are smaller than the resisting forces, there will be no erosion. The flow inside the filter layer can be in all directions, but for clarity a distinction is made between perpendicular flow and parallel flow. In case of perpendicular flow, the critical gradient is defined in the base layer, whereas in parallel flow this is defined in the filter layer (see figure 2.21).

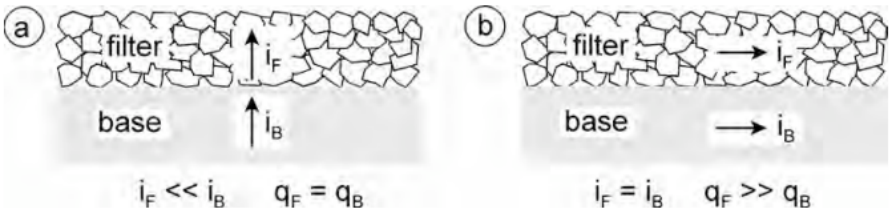

Figure 2.21: Perpendicular and parallel flow in granular filter (Schiereck, 2012).

When the water flows parallel to the filter/base interface, the gradient in both layers is roughly the same. Then, the flow velocity in the filter layer is much higher than in the base layer, due to the greater permeability. Because of the difference in gradient at the interface a shear stress on the upper grains of the base material is induced. This outcome can be compared to the situation for incipient motion in an open channel flow causing a critical shear stress; hence the critical gradient is defined in the filter layer. For perpendicular flow, the flow through the base and filter layer is equal, causing a much larger gradient in the base layer, due to the larger permeability in the filter layer.

The stability of base material in a flow parallel to the interface of a filter can be seen as the stability of a grain on the bottom of a very small channel (Schiereck, 2012). De Graauw (1983) demonstrated an empirical relation between the critical gradient in porous flow and the Forchheimer equation, given the threshold of movements as developed by Shields. The first and second term in eq. (2.43) correspond, respectively to the laminar and turbulent terms (De Graauw et al., 1983):

$$i_c = \left[\frac{0.06}{n_F^3 d_{15F}^{4/3}} + \frac{n_F^{5/3} d_{15F}^{1/3}}{1000 d_{50B}^{5/3}} \right] \cdot u_{*cr}^2 \tag{2.43}$$

in which the filter velocity u_{*cr} can be derived from Shields's diagram or can be expressed as follows (De Graauw et al., 1983):

$$u_{*cr} = 1.3 \cdot d_{b50}^{0.57} + 8.3 \cdot 10^{-8} \cdot d_{b50}^{-1.2} \tag{2.44}$$

2.6.3 Design method for open filters

In the past a large number of tests have been performed by Wörman (1989), Bakker *et al.* (1994), and Hoffmans (2012) to determine criteria for the initiation of motion in granular filters. In our report the design criteria for Hoffmans' design formula and Wolters & Van Gent (2012) will be discussed in detail. For the other tests is referred to their published papers (Wörman, 1989; Bakker et al., 1994).

Hoffmans, 2012 / Van de Sande, 2012

Schiereck (2012) argued how the stability of a granular filter depends on the relation between the strength and load. Hoffmans's formula described strength as the shear strength of a single grain. If this shear stress exceeds the critical value, then the grains begin to move. Then, the relative strength η_c is defined as the ratio of the mean strength of the base layer $\tau_{c,bf}$ at the transition of the filter-base layer, and the mean strength at the top of the filter layer τ_c. Eq. (2.45) gives the derivation of the relative strength. For the full derivation, see Hoffmans (2012).

$$\eta_c = \frac{\tau_{c,bf}}{\tau_c} = \frac{d_{b50}}{d_{f50}} \frac{\Delta_b}{\Delta_f} \frac{\Psi_{c,b}}{\Psi_{c,f}} \frac{1 - \gamma V_{c,b}}{1 - \gamma V_{c,f}} \tag{2.45}$$

The relative load is the result of the balance of forces, the Forchheimer equation, the hypothesis of Boussinesq and the eddy viscosity (Hoffmans, 2012). In Hoffmans (2012) the relative load is given as eq. (2.46). For the derivation see Hoffmans (2012).

$$\eta = \frac{k_f(z)}{k_b} = e^{\frac{D_f}{\alpha_d d_{f15}}} \tag{2.46}$$

Combining eq. (2.45) and eq. (2.46) leads to the design method as developed by Hoffmans:

$$\frac{D_f}{d_{f15}} = \alpha_d \quad ln(\frac{d_{f50}}{d_{b50}} \frac{\Delta_f}{\Delta_b} \frac{\Psi_{c,f}}{\Psi_{c,b}} \frac{1-\gamma V_{Gf}}{1-\gamma V_{Gb}}) \tag{2.47}$$

Hoffmans derived for the load damp coefficient α_d a value of 1.5. Next, Van de Sande (2012) suggested a new design method with a relative layer thickness that fits better for d_{f50} than d_{f15}, and adopts a lower alpha value than the one proposed by Hoffmans (Van de Sande, 2012).

$$\frac{D_f}{d_{f50}} = \alpha_d \quad ln(\frac{d_{f50}}{d_{b50}} \frac{\Delta_f}{\Delta_b} \frac{\Psi_{c,f}}{\Psi_{c,b}} \frac{1-\gamma V_{Gf}}{1-\gamma V_{Gb}}) \tag{2.48}$$

Hoffmans (2012) compares his equation with the one developed by Wörman, see fig (2.22). The main difference between these two equations is the relation between the layer thickness and the material properties. In Wörman's formula this relation is linear, whereas in Hoffmans it is logarithmic.

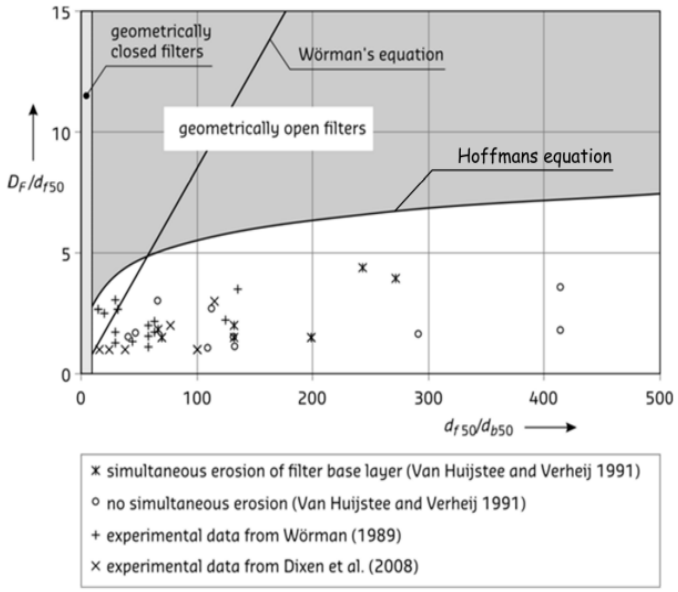

Figure 2.22: Wörman equation and Hoffmans equation compared with measurements (Hoffmans, 2012).

Wolters & Van Gent, 2012

Wolters & Van Gent conducted experiments for granular open filters on a horizontal sand bed under three different external loading conditions: wave loading, current loading or a combination of both. The physical model tests were performed in a wave & current flume that consisted of a submerged granular filter construction on a sand bed, see figure 2.23.

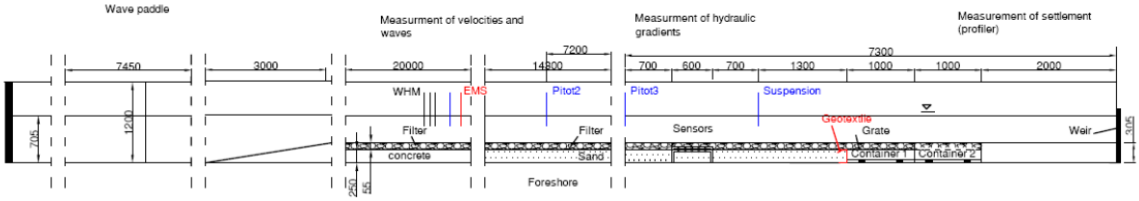

Figure 2.23: Set-up for current and combined wave & current loading (Wolters and Van Gent, 2012)

It should be noted that the velocities (u_f) inside the filter were not directly measured in this study. Instead, the two percent exceedance value of the velocities ($u_{2\%}$) is based on the measurements taken 25 mm above the filter. However, the gradients have been directly measured at the interface between the filter and the sand. Consequently, the data based on the $i_{2\%}/i_{cr}$ ratio can be considered somewhat more reliable (Wolters & Van Gent,

2012). Their research focused on the transport of base material itself. For low current velocities ($u_{2\%} < 0.6$ m/s) no base material transport was observed. Measurable material transport was observed through the filter at $u_{2\%} > 1m/s$. The observed amount of transport material was very low for the current loading (< 0.06 $g/m/s$).

Wolters & Van Gent concluded that the transport of sandy bed material in a granular filter can be described as a function of the hydraulic gradient $i_{2\%}/i_{cr}$, and would be independent of the loading condition (wave/ current/ wave & current). The measured transported base material from the tests is presented as T in $g/m/s$ and in dimensionless form T^*:

$$T^* = \frac{T/\rho_s}{\sqrt{\Delta g D_{50,b}^3}} \tag{2.49}$$

in which Δ the relative buoyant density of base material ($\rho_s/\rho_w - 1$). In figure 2.24 the (dimensionless) transport is plotted against the hydraulic gradient, resulting in the following relation:

$$T^* = 1.4 \cdot 10^{-6} (\frac{i_{2\%}}{i_{cr}})^{5.8} \tag{2.50}$$

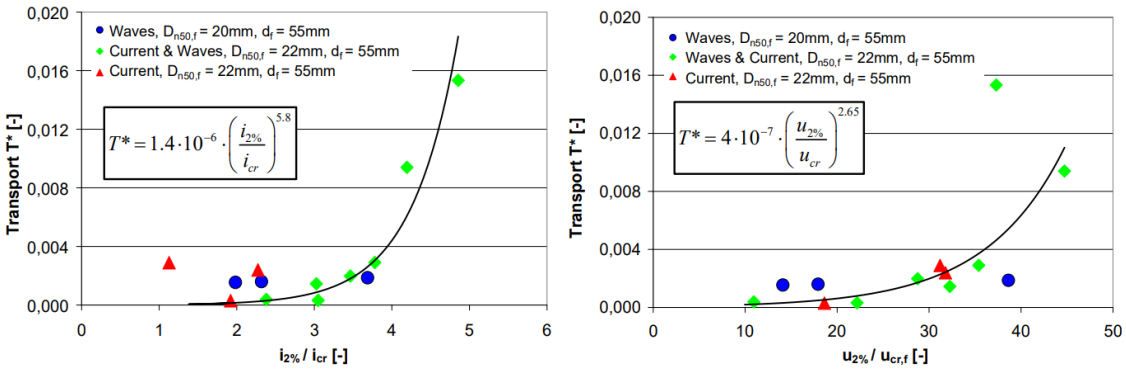

Figure 2.24: Transport vs. hydraulic gradient and Transport vs. velocity (Wolters & Van Gent, 2012).

For waves, the hydraulic gradient can be estimated using the modified Keulegan-Carpenter (KC_f) number. The KC_f number is based on the velocity measured directly above the filter exceeded by 2% of waves ($u_{2\%}$, the wave period T_m, porosity and filter thickness D_f:

$$KC_f = \frac{u_{2\%} T_m}{n_f D_f} \tag{2.51}$$

$$i_{2\%} = 0.06 \cdot KC_f^{0.28} \tag{2.52}$$

It should be noted that Wolters & Van Gent (2012) expected that the filter layer thickness would have a dominant effect on base material transport, and therefore the hydraulic gradient. Due to the limited amount of performed tests, this effect needs further study.

2.7 Summary - Literature review and past studies

In the second chapter, a comprehensive literature study was conducted to investigate the hydrodynamic processes that define the actual gradient at the location where the geotextile is positioned. The framework of linear wave theory proved to be a valuable tool for investigating and modeling these hydrodynamic processes. The analysis focused on defining the mean and fluctuating component of the gradient that occur at the bed level and on describing how the impact of these components is measured at the filter/base interface.

In uniform flow, a pressure gradient exists which overcome the shear resistance and causes the fluid to flow. This gradient can be characterized as the average gradient. Additionally, when the flow encounters a rough bed, it undergoes accelerations and decelerations, which has effect on the behavior of the boundary layer and the turbulence within the flow. By applying the Poisson equation the pressure fluctuations at the bed can be derived. The distribution of these pressure fluctuations across different frequencies can be characterized with the help of a pressure spectrum. Many studies on these spectra have been conducted in other fields of application. By transforming the pressure spectrum, it is possible to derive the pressure gradient. This is an important parameter for assessing the stability of an open filter; see chapter 3. For a filter to be stable, the actual gradient must be smaller than the critical gradient which implies that no transport through the filter will occur.

During the literature review, it became evident that there was a lack of existing literature on open geotextiles, thus revealing a research gap in this area. In this study, the assumption is made that the term open geotextiles is associated with open filter structures, providing an opportunity to explore the application of theory related to the mobility parameter and stability parameter for stable open filters. Previous studies have focused on designing methods for open granular filters, which differ from open geotextiles in their characteristics and behavior. The aim of this research was to formulate a design method to describe the stability of an open geotextile. As the concept of an open geotextile had not been developed, it prompted us to examine the physics of an open filter and take such as a point of departure. Therefore, the study was divided into two steps: firstly, understanding the physics of an open filter, and secondly applying this knowledge to geotextiles. Based on this literature review, it became apparent that the actual gradient at the bed level can be divided in an average component and a fluctuating component. To determine the actual gradient, the following hypothesis is proposed:

The actual gradient can be defined by adding the average gradient to a turbulent component derived from measured turbulent wall pressure spectra at the top of the filter layer. Based on spectral approach and linear damping, it is hypothesized that these turbulent components undergo damping within the filter layer, resulting in a diminished turbulent component at the filter/base interface.

From the literature review, it can be inferred that the dimensionless turbulent rough wall pressure spectra developed by Blake (1970) offer the most appropriate representation for the relevant hydraulic conditions (rough horizontal bed, uniform open channel flow). By adopting the spectral approach, we are able to determine the turbulent component, and incorporating the framework of linear damping enables us to describe the damping occurring within the filter layer. This spectral approach allows us to approach the actual gradient at the interface between the filter and the base. To verify this hypothesis, two suitable datasets were identified in the literature. The dataset from Van de Sande (2012) provides an indirect verification of this hypothesis by examining stable or unstable filter conditions. On the other hand, the dataset from Wolters & Van Gent (2012) enables a direct comparison of the actual gradients. These datasets offer valuable insights to support and evaluate the proposed hypothesis.

3 The hypothesis for the actual gradient

This chapter describes the analytical approach to derive the actual gradient at the location of the geotextile. Consistent with the criteria established for open filters, this hypothesis specifies that the actual gradient can be defined as the sum of the average gradient and a turbulent component that can be obtained from the pressure spectra measured by Blake (1970). This chapter extensively describes the approach to find the gradient of the turbulent component. A detailed explanation of the hypothesis for assessing the actual gradient under turbulent uniform flow conditions can be found in section 3.1. To effectively outline the steps involved in the hypothesis, certain assumptions and simplifications need to be made, which are elaborated upon in section 3.2. Furthermore, a visual representation of the steps in the hypothesis is provided in the form of a flow chart, depicted in section 3.3.

3.1 The actual gradient under turbulent uniform flow

The hypothesis follows the principle of linear wave theory and all of its assumptions and limitations. To review the pressure fluctuations on the bed, the outcome is demonstrated in the form of a pressure spectrum. The pressure spectrum can be transformed to the gradient pressure spectrum to eventually find the gradient at the location where the geotextile is placed. Its locations is the filter/sand interface at $z = -D_f$, see figure 3.1. It is crucial to bear in mind that the pressure fluctuations obtained from the pressure spectra represent the turbulent component. In this study, when referring to the gradient in the pressure spectrum, it specifically implies the fluctuating gradient (i') rather than the average gradient ($\bar{i}$). A more detailed explanation about the difference between the two gradients will be provided in section 3.6.

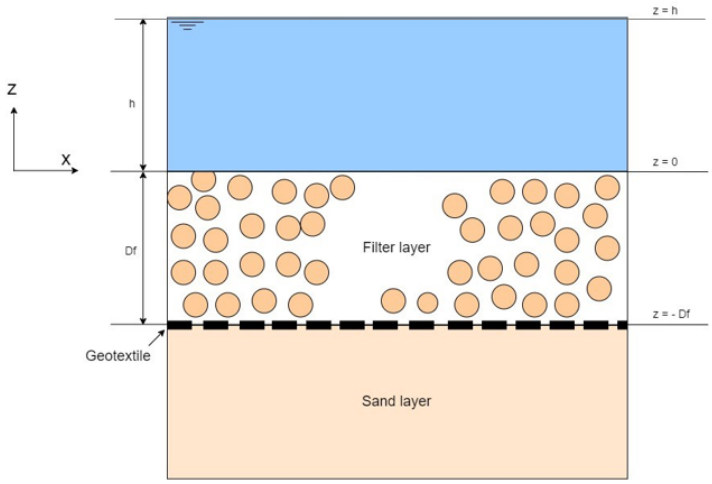

Figure 3.1: Geotextile under a single filter layer in uniform flow.

The hypothesis can be divided in two phases. The first phase consists of transforming the pressure spectrum to a pressure gradient spectrum. In the second phase the spectral domain of the pressure gradient is transformed to the spatial domain assuming a random phase. In the spatial domain the actual gradient at the filter/sand interface then can be deducted.

3.1.1 Dimensionless rough wall pressure spectrum

In the literature review, it was concluded that the pressure spectra measured by Blake offered the most appropriate representation for this study on geotextiles. Blake (1970) at an early date argued how a dimensionless pressure spectrum for rough walls could be obtained through turbulent boundary-layer wall-pressure measurements in a wind tunnel. In his measurements, he used two different types of rough walls: densely packed large elements (D-L) and sparsely packed small elements (S-S). Figure 2.11b and 2.12 illustrate the presence of scatter across different stone sizes. Taking into consideration the order of magnitude of typical filter materials, it is determined that the large elements (D-L) exhibit the closest resemblance to the filter material. In this study the largest equivalent sand roughness height k_s is chosen, which is the densely packed one (D-L) and amounts to approximately 5 mm. Figure 3.2 displays the curves representing the densely packed large elements for both the outer and inner variables.

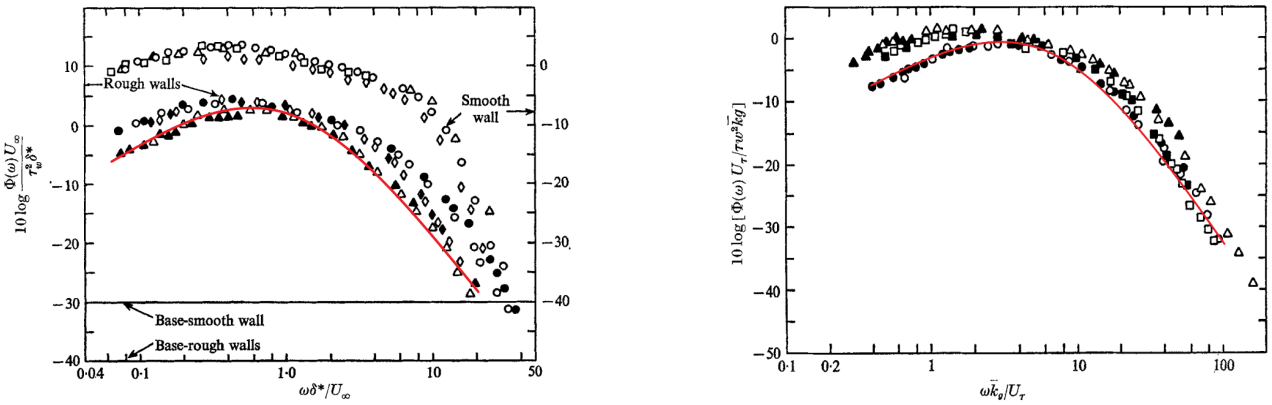

(a) The curve presenting the outer variables.

(b) The curve presenting the inner variables.

Figure 3.2: The pressure spectra presented by the D-L elements (Blake, 1970).

Given the uncertainties on how to deal with the roughness and threshold of motion, the practical choice of $k_s = 2d_{n50}$ is made, resulting in a nominal diameter d_{n50} of 2.5 mm (Schiereck, 2012). Although this measurement has been acquired from wind measurement, the TWP characteristics in both fields are generated by near-bed flow processes, showing the same scaling behavior for the high-frequency region (Hofland, 2005). Therefore the pressure spectrum of Blake is assumed to be useful for this hypothesis when focusing on the high-frequency region in the spectrum. As for the low-frequency region, the free surface influences the pressures, expecting a different spectrum. Unfortunately, there is hardly any literature available and thus more research is required on this matter. In this report, it is assumed that the scaling of the low-frequency region is the same for open channel flow.

3.1.2 Phase 1: pressure spectrum/ spectral domain

The starting point of this hypothesis is the dimensionless pressure spectrum $\Phi_{pp}(\omega)$ that was originally developed by Blake (1970). Figure 3.3 shows a schematization of a pressure spectrum under turbulent uniform flow that is plotted on a double logarithmic scale. The use of a double logarithmic scale provides a visual representation that allows for the observation of a slope between the low- to high-frequencies. Generally, this is in agreement with the cascade process of turbulent energy being converted from large-scale eddies to small-scale eddies. In the literature review different slopes were assumed depending on the scaling region in the spectrum. In the overlap region, usually a slope of $-\frac{4}{3}$ or -1 is proposed (Meyers et al., 2015; Blake, 1970).

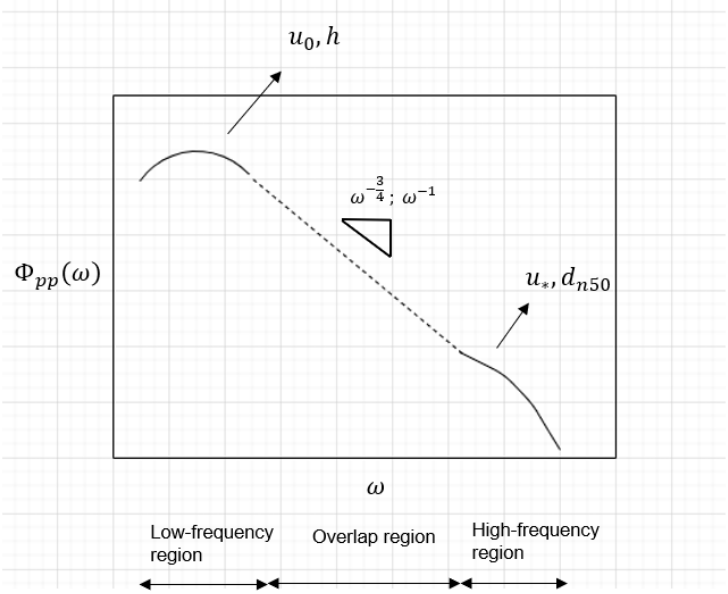

Figure 3.3: Pressure spectrum scaled on variables in different regions.

Blake (1970) described the scaling of the low-frequency region for the outer variables δ^*, U_∞ and τ_w, whereas the high-frequency region is better scaled for the inner variables k_g, U_τ and τ_w. The equivalent sand-grain roughness k_s is usually greater than the geometric height of the roughness k_g. In Blake (1970) the k_s/k_g ratio is approximately 2, meaning that the geometric height k_g is equal to the stone size d_{n50}. At an earlier stage various scaling variables had been experimented with (Farabee and Casarella, 1991; I. Lee and Sung, 2002; Hofland, 2005; Meyers et al., 2015). In this hypothesis the assumption is that the low-frequency region is scaled for the depth and time averaged velocity, u_0 and water depth h. Therefore, the assumption is made that the averaged velocity is related to the free-stream velocity, and the displacement thickness layer to the water depth (Hofland, 2005; Farabee and Casarella 1991). The scaling variables for the high-frequency region is kept the same as in Blake (1970). The shear stress can be rewritten in terms of the averaged velocity or shear velocity, see eq. (2.23). The roughness height can be rewritten in terms of the nominal diameter. As a result, the following two relations are proposed for low- and high-frequency region in the dimensionless pressure spectrum, respectively:

$$\frac{\Phi(\omega)U_\infty}{\tau_w^2\delta^*} \quad vs. \frac{\omega\delta^*}{U_\infty} \quad (\text{Blake}, 1970) \qquad \rightarrow \qquad \frac{\Phi(\omega)}{u_0^3 c_f^2 \rho_w^2 h} \quad \text{vs.} \quad \frac{\omega h}{u_0} \tag{3.1}$$

$$\frac{\Phi(\omega)U_\tau}{\tau_w^2 k_g} \quad vs. \frac{\omega k_g}{U_\tau} \quad (\text{Blake}, 1970) \qquad \rightarrow \qquad \frac{\Phi(\omega)}{u_*^3 \rho_w^2 d_{n50}} \quad \text{vs.} \quad \frac{\omega d_{n50}}{u_*} \tag{3.2}$$

Eq. (3.1) and (3.2) can also be rewritten in the dimensionless power spectral density $\Phi(\omega)^+$ and the dimensionless angular frequency ω^+ scaled on either their inner or outer variables. The pressure spectrum, as introduced by Blake is defined as an one-dimensional frequency spectrum made dimensionless based on scaling variables in the outer or inner regions of the boundary layer. The one-dimensional wave-number spectrum $\Phi_{pp}(k)$ is identical to that of the frequency spectrum with two exceptions. Firstly, time t is substituted by the horizontal co-ordinate x, and secondly, the radian frequency ω similarly is substituted by wave-number k. The subscript pp in the power spectral density stands for the pressure. Later in this study the subscript ii is used to indicate the gradient. For the transformation of a spectrum it must be borne in mind that the total variance $\overline{\eta}^2$ must be conserved (Holthuijsen, 2007). The conversion from a frequency spectrum to the radian frequency spectrum requires the Jacobian $J = \frac{1}{2\pi}$ (see eq. (2.16)). For the transformation to the wave-number spectrum the Jacobian value $\mathrm{J}\frac{\partial\omega}{\partial k}$ is needed to conserve the total variance. By use of the dispersion relationship of the linear wave theory, the frequencies ω and wave-numbers k are related. Under wave loading this is the group velocity c_g of waves, but under turbulent uniform flow this is influenced by the rotating vortexes. Blake applied for rough walls a convection velocity of 0.44 times the average velocity. The transformation then, is the following:

$$\Phi_{pp}(k) = \Phi_{pp}(\omega) \cdot 0.44 \cdot u_0 = \Phi_{pp}(\omega) \cdot u_c \tag{3.3}$$

$$k = \omega/(0.44 \cdot u_0) \tag{3.4}$$

Since the objective of this hypothesis is to determine the actual gradient, the next step is to describe the pressure gradient spectrum. To get a better understanding of the transformation, the relation between the pressure p and gradient i is explained with Darcy's law. The elevation z is not included in the equation, since we will remain on the corresponding horizontal position ($z = 0$). In Darcy's law the following relation for the pressure head, then, results:

$$\psi = \frac{p}{\rho_w g} = \frac{a \cdot sin(kx)}{\rho_w g} \tag{3.5}$$

in which the pressure p is defined as a pressure wave caused by the rough bed. Please note that in eq. (3.5), a sine wave is used to represent this wave; however, a cosine wave could also be employed for the same purpose. The hydraulic pressure gradient in the x-direction then becomes:

$$i'(x) = \frac{d\psi}{dx} = \frac{k \cdot a \cdot cos(kx)}{\rho_w g} \tag{3.6}$$

On the concept of wave spectrum, it is known that Fourier series with randomly chosen amplitudes and phases create a random sea-surface. With the random-phase/amplitude model, an amplitude spectrum can be described from this random sea-surface. The same method is followed for the pressure wave as for the surface elevation $\eta(t)$ in the wave spectrum. This means that the sum of a large number of pressure waves can be described with a Fourier series in spatial domain x, as follows:

$$p(x) = \sum_{n=1}^{N} a_n \cdot sin(k_n x) \tag{3.7}$$

in which n is the sequence number of the wave in the record, a_n the amplitude, and N the number of waves. The variance of the Fourier mode is the average of $(a_n \cdot sin(k_n x))^2$; this is equal to $\frac{1}{2}a^2$. An illustration of the distribution of the total variance is shown in figure 3.4. A single component n in this discrete spectrum is related to the spectrum via:

$$\Delta k \cdot \Phi_{pp}(k_n) = \frac{1}{2} a_n^2 \tag{3.8}$$

where $\Phi_{pp}(k_n)$ is the variance density, and $\Delta k \Phi_{pp}(k_n)$ the variance.

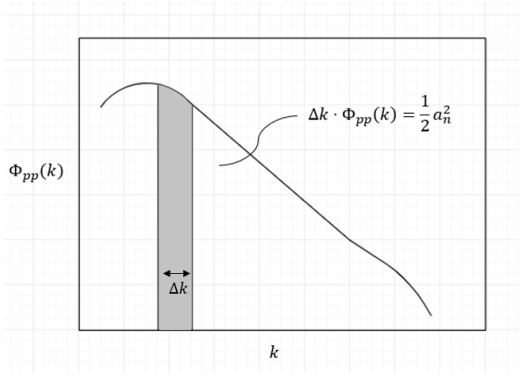

Figure 3.4: The variance of Δk in the pressure spectrum.

Next, the gradient can be described from the pressure wave. This leads to:

$$i'(x) = \sum_{n=1}^{N} a_{i,n} \cdot cos(k_n x) \quad \text{with :} \quad a_{i,n} = \frac{k_n a_n}{\rho_w g} \tag{3.9}$$

See eq. (3.6) for the derivation of the amplitude a_i. For the gradient spectrum the cosine also gives the variance $\frac{1}{2}a^2$. The difference is the amplitude term, resulting in the eq. (3.10):

$$\Delta k \cdot \Phi_{ii}(k) = \frac{1}{2} a_i^2 \tag{3.10}$$

The transformation from the pressure spectrum to the gradient spectrum is described by rewriting eq. (3.8) in eq. (3.10):

$$\Phi_{ii}(k, z = 0) = \Phi_{pp}(k) \cdot (\frac{k}{\rho_w g})^2 \tag{3.11}$$

Remember that Blake measured the pressure fluctuations on the rough walls. Therefore, the pressure gradient spectrum in eq. (3.11) indicates the gradient at bed level ($z = 0$). However, the location of geotextiles for a bed protection is between the granular filter layer and the base material, see figure 3.1. In order to describe the spectrum at the filter/base interface the assumption is made that the flow inside the porous media is laminar (low Reynolds numbers). Given laminar flow in the porous media, the pressure at the filter/base interface is derived following eq. (3.5). The assumption is therefore made that the pressure waves are not influenced by the permeable filter layer. Given the Laplace equation (eq. (2.40)), the assumption is made that the permeability coefficient K drops out of the equation:

$$K \cdot \nabla^2 \psi = 0 \qquad \text{becomes} \qquad \nabla^2 \psi = 0 \tag{3.12}$$

Eq. (3.12) shows, in accordance with theory, how for the gradient it is not relevant whatever the permeability of the granular material is, on the assumption that the material is not zero (impermeable wall). This equation describes the relationship where the divergence of the gradient (Laplace operator) of the pressure head is equal to zero, ensuring a uniform pressure field at the bed ($z = 0$), as shown in equation (3.13). Figure 3.5 pictures the situation.

$$\psi(z = 0) = \psi_f(z' = D_f) \tag{3.13}$$

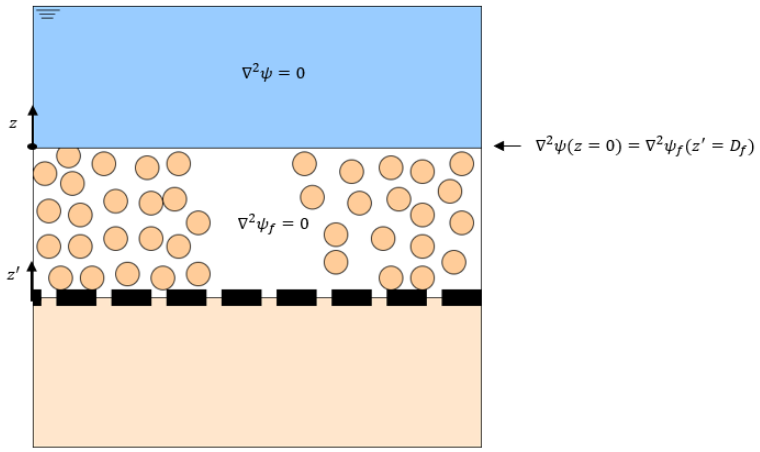

Figure 3.5: Pressure head ψ at the water/filter interface at $z = 0$.

On the assumption of a constant value for the pressure field at $z = 0$, now the pressure at the interface of the filter/base layer can be described with the thickness of the filter layer in the same way as describing the wave-induced pressure at the bed, see section 2.2.1. The gradient over a spatial distance x (see eq. (3.9)) at the filter/base interface ($z = -D_f$) is described by the following function:

$$i'(x) = \sum_{n=1}^{N} \frac{a_{i,n} \cdot cos(k_n x)}{cosh(k_n D_f)} \tag{3.14}$$

Or in terms of the gradient spectrum at $z = -D_f$:

$$\Phi_{ii}(k, z = -D_f) = \frac{\Phi_{ii}(k, z = 0)}{cosh(kD_f)^2} \tag{3.15}$$

3.1.3 Phase 2: Spatial domain

The second phase consists of the transformation of the spectral/frequency domain into the spatial domain on the assumption of a random-phase model with random phases between $0 \leq \underline{\alpha} \leq 2\pi$. The pressure gradient, therefore, is:

$$i'(x) = \sum_{n=\Delta k}^{N\Delta k} a_{i,n} \cdot cos(k_n x + \underline{\alpha}_n) \tag{3.16}$$

Each gradient component i has a distinct value for the amplitude a_i, and the wave-number k. α_n is the only random variable. Since the gradient spectrum is known from the method of Blake (phase 1), it is convenient to rewrite eq. (3.10) in terms of the amplitude a_i:

$$a_i = \sqrt{2 \cdot \Delta k \cdot \Phi_{ii}(k_n, z = -D_f)} \tag{3.17}$$

The pressure gradient can therefore be derived from the spectrum with the following function:

$$i'(x) = \sum_{n=\Delta k}^{N\Delta k} \sqrt{2 \cdot \Delta k \cdot \Phi_{ii}(k_n, z = -D_f)} \cdot cos(k_n x + \underline{\alpha}_n) \tag{3.18}$$

On the concept of wave spectrum, the narrower the spectrum, the more regular the record is. In the spectrum of Blake (1970) the distribution of the variance is divided over a wide frequency band, which gives a rather chaotic gradient field. Figure 3.6 illustrates the transformation of the spectral domain to the spatial domain in the x-direction, as shown in eq. (3.18).

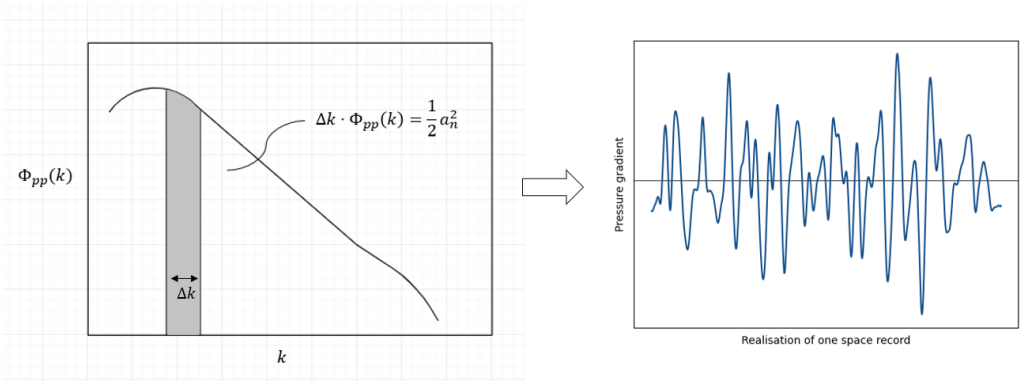

Figure 3.6: Transformation from the spectral domain (left) to the spatial domain (right).

In the space record, the gradients' 2% exceedance value ($i'_{2\%}$) can be determined. Originally, the two percent parameter is used to describe the two percent of the largest waves. In a time record/signal, a wave is the profile of the surface elevation between two downward (or upward) zero-crossings of the elevation (Holthuijsen, 2007). From this signal, the peaks of individual waves are measured, and the total number of waves occurring in the signal can be determined. Each individual wave measurement results in a discrete value. For example, if there are 1000 waves in a specific time record, the 2 percent of the largest waves correspond to the 20 largest waves in the signal ($H_{2\%}$). In the case of currents, a continuous turbulent signal presents the gradient. The distinction arises due to the nature of turbulent flow, where individual gradients caused by turbulence are not determined separately. Instead, each gradient is considered. In Figure 3.7, the wave height H corresponds to a discrete value representing a single wave, while the gradient i (red dots) shows a continuous signal where every point is considered.

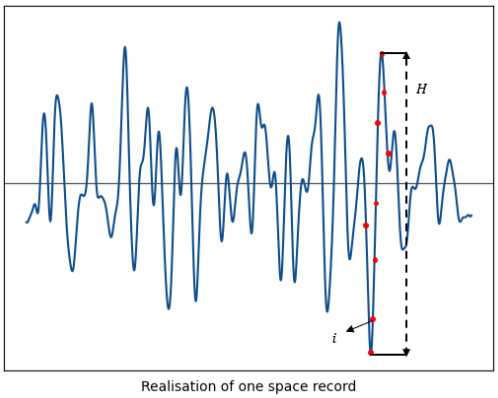

Figure 3.7: The definition of the discreet wave height H and continuous gradient i (red dots) in a record.

One way to present the 2 percent largest gradients ($i'_{2\%}$) is by means of a histogram. By creating a histogram of the absolute gradient values, you can visualize the distribution of gradients and identify the bins that capture the top 2 percent of the largest gradients. In figure 3.8, the $i'_{2\%}$ is represented by the green dotted line.

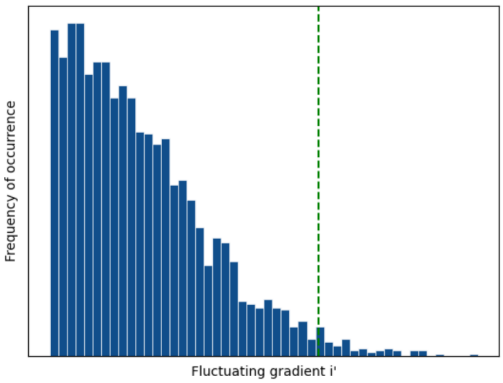

Figure 3.8: The histogram represents the distribution of gradients from the space record, with the $i_{2\%}$ indicated by the green dotted lines.

So far, the actual gradient is derived for the gradient of the fluctuating pressures ($i'_{2\%}$). The average gradient is therefore not yet taken into account. In case of an uniform flow, the average gradient can be written according to eq. (2.26). Figure 3.9 illustrates both average and fluctuating gradient for uniform flow conditions. Previous experiments have demonstrated exponential damping of pressure fluctuations, as observed in Klar (2005), and therefore also an exponential decay in fluctuating gradient.

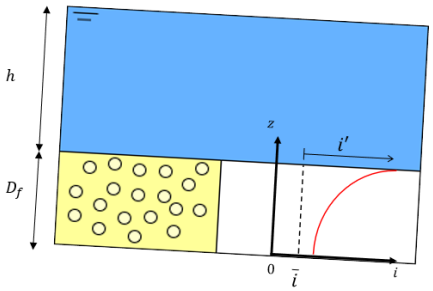

Figure 3.9: Average gradient $\bar{i}$ and fluctuating gradient i' for uniform flow.

The actual gradient $i_{a,2\%}$ is obtained by combining the average gradient $\bar{i}$ from equation (2.26) and the 2 percent largest gradients of the fluctuating gradient $i'_{2\%}$ from equation (3.18), as shown in eq. (3.19).

$$i_{a,2\%} = \bar{i} + i'_{2\%} \tag{3.19}$$

From eq. (3.19) an approach can be made to determine the actual gradient.

3.2 Assumptions and simplifications

In this section the assumptions and simplifications are presented that were made for the hypothesis under turbulent uniform flow. Two important assumptions that have been adopted for our method are the linear wave theory and laminar flow in the filter layer. Both assumptions were shortly elaborated on in the literature review. For an extensive review on linear wave theory and laminar flow, see references, respectively Holthuijsen (2007) and Schiereck (2012). Other assumptions or simplifications that were decided on are listed below:

- The pressure spectrum of Blake (1970) follows the principle of an impermeable rough wall. Contrary to this assumption, it is hypothesized that the same spectrum hold for a permeable rough wall.
- The measurements by Blake (1970) were executed in a wind tunnel. For the low frequencies, however, the spectra are expected to differ in a water/air environment, because of the free surface in the water environment. In this method, the hypothesis has been argued that both environments have the same spectra.
- The boundaries of the pressure spectrum of Blake (1970) are bound to the limitations of the measurements. The assumption is therefore made that the scope of the pressure spectrum of Blake covers the low- and high-frequencies of the spectrum when considering an open channel.
- The densely packed large elements (D-L) used for the rough walls in Blake (1970) are the largest sized elements and assuming $k_s = 2d_{n50}$, and have a nominal diameter of 2.5 mm. It is assumed that larger stone sizes do not change the presented pressure spectrum of Blake (1970).
- One of the scaling variables for the low-frequency region is the depth and time averaged velocity. For smooth walls, Hofland (2005) confirmed that the averaged velocity scaled the low-frequencies, but for rough walls this is not confirmed. Therefore, the assumption is made that for rough walls the average velocity collapses the spectrum in the low-frequency region.
- Even though the filter material is permeable, it is assumed that the waves are not influenced by the permeable rough bed.
- The stability of the geotextile depends on the chosen stage for allowable transport according to the Shields graph. The desired transport for this geotextile is low, so that occasional movement of grains is allowed for some locations at the top base layer.

3.3 Flowchart hypothesis

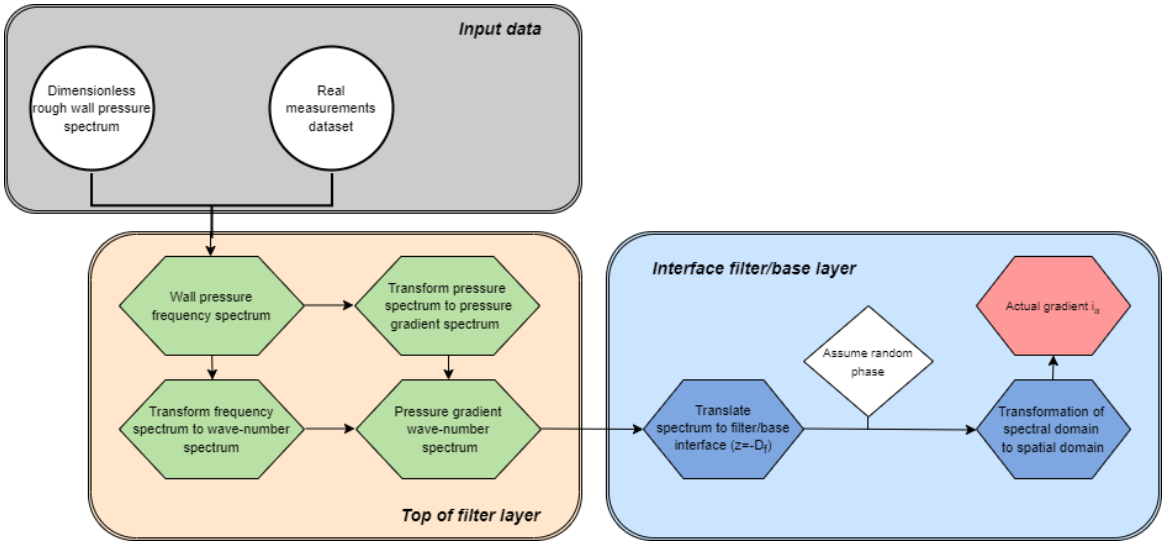

Figure 3.10: Flowchart of the hypothesis for the actual gradient.

3.4 Summary - The hypothesis for the actual gradient

To develop a design method that accurately captures the stability of geotextiles, the initial focus should fall on calculating the gradients at the locations within the filter structure where the geotextiles is located. At this stage, a hypothesis is formulated regarding the determination of the actual gradients, which are composed of both average gradients and fluctuating gradients. While the average gradient is defined by the resistance of flow and can be easily explained for uniform flow conditions, particular attention is given to the fluctuating component. In this hypothesis, an approach is described that relies on a dimensionless rough wall pressure spectrum developed by Blake (1970). These spectra are scaled by using appropriate characteristics and can be categorized into two types: one representing the low-frequencies scaled on outer variables, and the other depicting the high-frequencies scaled on inner variables. The combination of both spectra gives the determination of the fluctuating gradient that results from the entire pressure spectrum. The theoretical framework of linear damping is another key element that influences the definition of the pressure gradient at the filter/base interface. Additionally, certain assumptions and simplifications are made to enable the practical implementation of this hypothesis. They are part of the utilization of linear wave theory.

4 | Verification of the hypothesis

In this chapter, the hypothesis for actual gradient is tested using the experimental data provided by Van de Sande (2012) and Wolters & Van Gent (2012). Optimally, the results of the hypothesis coincide with the results of both experiments. As discussed in the literature study, Van de Sande's experiments have provided valuable validation for Hoffman's formula through physical experiments, making it a suitable and reliable option to test the effectiveness of the hypothesis in terms of stability. In the case of the measured data from Wolters & Van Gent (2012), a direct comparison with the hypothesis is possible since the gradients were measured directly in the experiments. Firstly, the experimental setup of Van de Sande and the outcomes of his research are presented in section 4.1. The dataset obtained by Van de Sande is integrated into the approach of the hypothesis in section 4.2, allowing for the calculation of gradients at the filter/base interface. In section 4.2.3, the stability at the filter/base interface is assessed based on the stability criteria defined for open filters. Section 4.3 presents the experimental setup and results conducted by Wolters & Van Gent (2012). Subsequently, the actual gradient is calculated using their measured data.

4.1 Dataset Van de Sande (2012)

Van de Sande (2012) conducted several experiments in a 12 meter long flume in the Environmental Fluid Mechanic Laboratory at Delft University of Technology. Other important properties of the flume are the width, depth and discharge: 40 cm, 40 cm and $\sim$ 100 l/s, respectively. Figure 4.1 gives an impression of the flume. In his experiments he tested the design method of Hoffmans for the stability of a granular open filter.

Figure 4.1: Flume with test set-up in the Environmental Fluid Mechanic Laboratory (Van de Sande, 2012).

The results of his tests can be split up in three categories, see figure 4.2 (Van de Sande, 2012):

- Base material moves at a lower critical velocity than the filter material (red area in figure 4.2).
- Base and filter material begin to move at about the same critical velocity (orange area in figure 4.2).
- Filter material moves at a lower critical velocity than the base material (green area in figure 4.2).

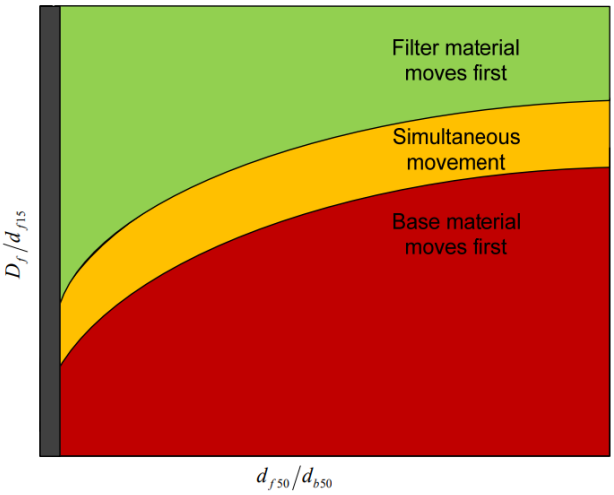

Figure 4.2: Movement of base material and filter material (Van de Sande, 2012).

The transport of filter material was based on the initiation of motion and was measured visually. The amount of transported base material is caught in a sieve placed behind the flume. After that the base material is dried and weighted. By measuring the amount of transport and plotting this against the velocity, the critical velocity can be determined when the grains start to move. Table 4.1 shows the results of each test.

Test	$u_{c,b} < u_{c,f}$ (red area)	$u_{c,b} \approx u_{c,f}$ (orange area)	$u_{c,b} > u_{c,f}$ (green area)
T01			x
T02a	x		
T02b	x		
T03		x	
T04		x	
T05	x		
T06a		x	
T07			x

Table 4.1: Results of the model test (Van de Sande, 2012).

Base material

For his experiments, Van de Sande used two types of base material. The dimensions are given in table 4.2. The analysis of these dimensions (sieve curve, densities) is well discussed in Van de Sande (2012).

	Type	d_{b15} [μm]	d_{b50} [μm]	d_{b85} [μm]	ρ_b [kg/m^3]
A_b	m32	248	309	389	2630
B_b	0.50-0.80	523	633	739	2527

Table 4.2: Dimensions and density base material (Van de Sande, 2012).

Filter material

As for the filter material, the stone type Yellow Sun and Basalt were used, see table 4.3. For the sieve curves and measurements, see Van de Sande (2012).

	Type	d_{f15} [mm]	d_{f50} [mm]	d_{f85} [mm]	d_{fn50} [mm]	ρ_f [kg/m^3]	n_F [$-$]
A_f	Yellow Sun 8-11	7.42	8.57	9.99	7.54	2633	0.43
B_f	Basalt 16-22	15.93	17.86	19.91	15.72	2960	0.38
C_f	Yellow Sun 20-40	22.45	25.01	27.23	22.01	2633	0.31

Table 4.3: Dimensions and density filter material (Van de Sande, 2012).

Tests

Not all experiments performed by Van de Sande were useful for the verification of the hypothesis. In test T02a the stones placed above the test section for base material transport were glued together. Also, test T05 has not been used, since no measurements were obtained in that test, and the conclusions were based on visual observations. Table 4.4 presents the cases for which the hypothesis will be tested, including the material and the thickness of the filter layer D_f. Also, the critical velocities for the base and filter material are given in the table in order to show at which velocity the transport of material starts.

	T01	T02b	T03	T04	T06a	T07
Filter	A_f	C_f	C_f	C_f	B_f	B_f
Base	A_b	A_b	A_b	B_b	A_b	A_b
D_f $[mm]$	20	27	61.5	27	40	57
$u_{c,b}$ $[m/s]$	> 1.00	~ 0.60	~ 0.85	~ 0.90	~ 0.90	> 0.95
$u_{c,f}$ $[m/s]$	~ 0.65	> 0.60	~ 0.85	~ 0.90	~ 0.90	~ 0.80

Table 4.4: Data tests (Van de Sande, 2012).

4.2 Verification of the hypothesis with Van de Sande (2012)

This section together with appendix A presents the results of the model tests of the hypothesis. All the different steps, as illustrated by the flowchart (figure 3.10) are presented here for test T01 case 1; for the other cases, see appendix A.

4.2.1 Dimensional rough wall pressure spectrum

The initial stage in the flowchart involves utilizing Blake's (1970) dimensionless rough wall pressure spectra. As discussed earlier in Chapter 3, Blake's figures exhibit scatter across different stone sizes. For this study, the experiments featuring the largest equivalent sand roughness height, denoted respectively by the triangle and circle symbols in figure 2.12 and 2.11b, were chosen. Figure 4.3 illustrates the dimensionless pressure spectra of Blake. The left panel corresponds to the red line shown in Blake's figure depicted in Figure 3.2a, while the right panel corresponds to the red line in Blake's figure presented in Figure 3.2b. It should be noted that the axis in this figure differs from Blake's due to assumptions defined for an open channel, as outlined in equations (3.1) and (3.2). The nominal diameter d_{n50} in equation (3.2) corresponds to that of the filter material and will be referred to as d_{fn50}. As figure 4.3 is dimensionless and independent of the input parameters of Van de Sande, it can be utilized for each test case.

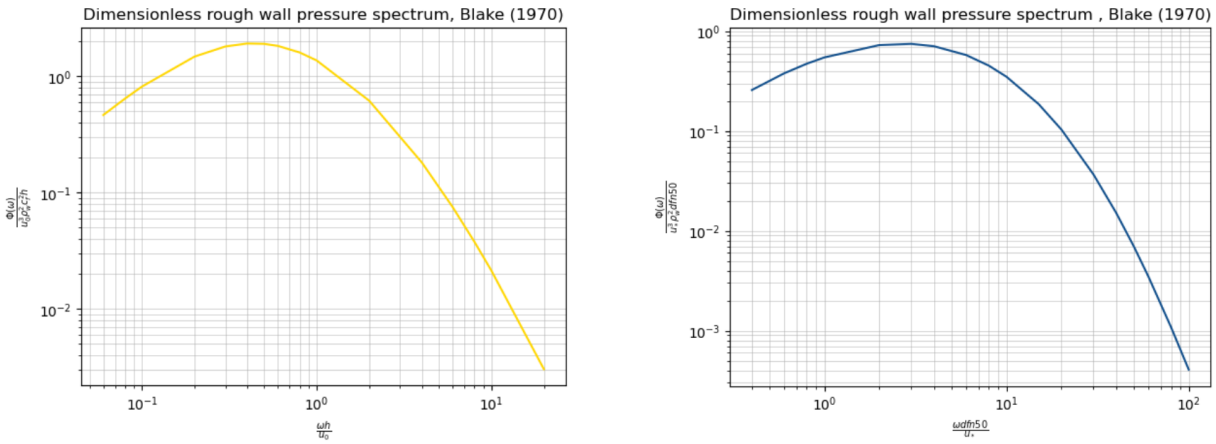

(a) Pressure spectrum scaled on the outer variables.

(b) Pressure spectrum scaled on the inner variables.

Figure 4.3: Pressure spectra of Blake (1970).

In order to asses the velocity which initiates the motion of the filter/base material, Van de Sande increased the velocity until the critical value was reached (see table 4.4). For the testing of our hypothesis the same increase of velocity is being used to analyze the stability of the base material. The Van de Sande (2012) dataset gives us the measured mean velocities in table 4.5 with the corresponding water depths, shear velocities and stone

sizes. These parameters will be the input scaling parameters for the dimensionless spectrum of our hypothesis in figure 4.3.

T01	Mean velocity u_0 $[m/s]$	Water depth h $[cm]$	Shear velocity u_* $[m/s]$	Stone size d_{fn50} $[mm]$
Case 1.	0.30	6.7	0.0326	7.54
Case 2.	0.40	23.4	0.0360	7.54
Case 3.	0.55	23.8	0.0494	7.54
Case 4.	0.60	26.5	0.0533	7.54
Case 5.	1.00	17.1	0.0933	7.54

Table 4.5: Scaling parameters for pressure spectrum obtained from dataset Van de Sande (2012).

The subsequent step in the flowchart involves assigning a dimension to the dimensionless spectrum by inputting the values of the scaling parameters obtained from Van de Sande's dataset. Figure 4.4 displays the pressure spectrum at z=0 for all T01 cases. It is evident that the curves of the scaled inner and outer variables shift upward as the velocities increase.

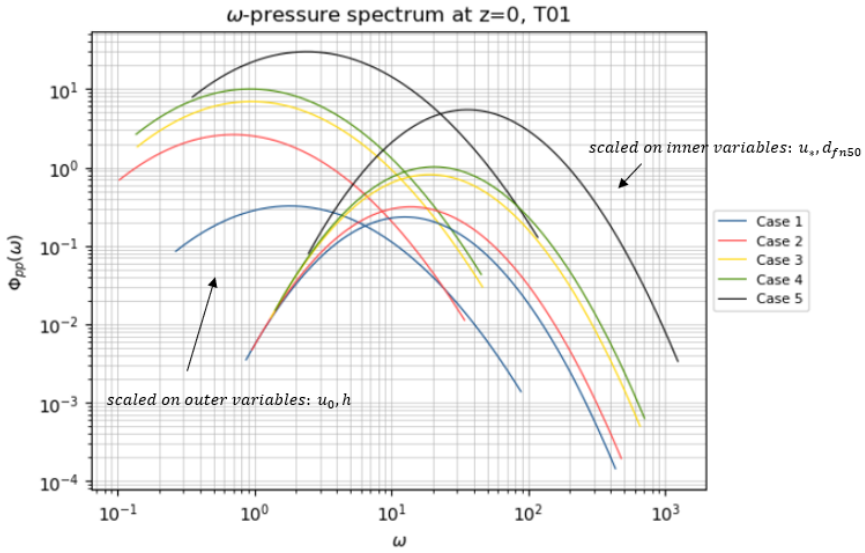

Figure 4.4: Frequency pressure spectrum.

To determine the actual gradient, we can merge the dimensional curves scaled on the outer variables with those scaled on the inner variables by drawing a line between them. Focusing on case 1 of T01, Figure 4.5 illustrates this concept, where the peaks of both curves are connected using a dotted line. The yellow line represents the curve scaled on the outer variables, while the blue line represents the curve scaled on the inner variables. Drawing a line between the two peaks adds a small area to the spectrum, impacting the actual gradient and resulting in a more conservative value. This will be discussed in more detail in chapter 5.

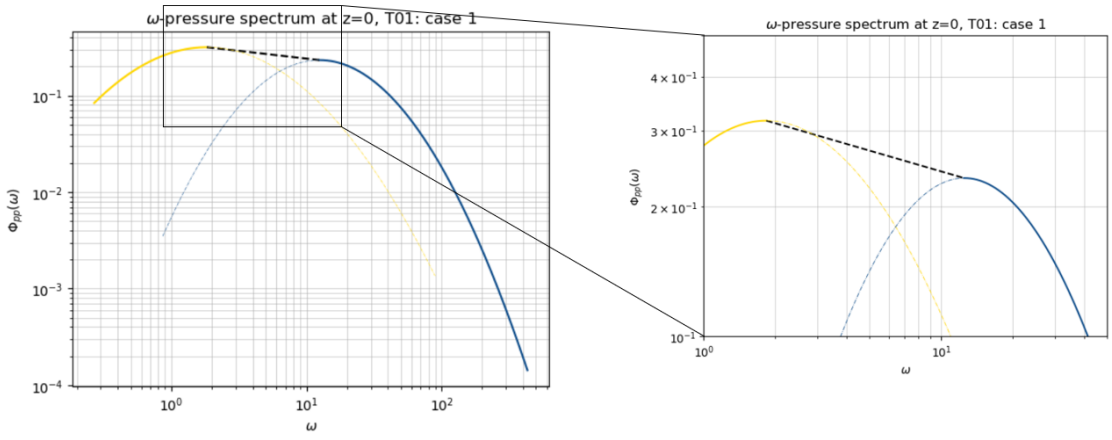

Figure 4.5: Dotted line combining both peaks of the pressure spectra.

In order to convert the frequency spectrum into the wave-number spectrum, the same convection velocity of

0.44 times the average velocity is employed, as initially introduced by Blake (1970). Subsequently, the pressure gradient spectrum, as outlined in equation (3.11), is derived. At this stage, the spectrum is obtained at the top of the filter layer, specifically at $z = 0$. By dividing the spectrum by $\cosh(\mathrm{kD_f})^2$, as described in equation (3.15), the pressure gradient spectrum at the filter/base interface ($z = -D_f$) is obtained, as depicted in figure 4.6.

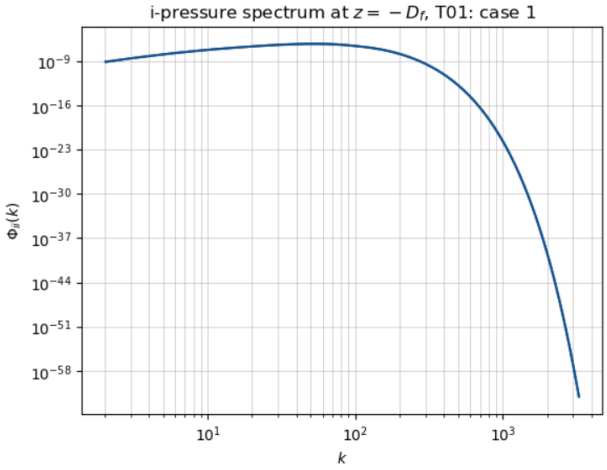

Figure 4.6: Pressure gradient spectrum at $z = D_f$.

4.2.2 The step size in both domains

Once the spectrum at the filter/base interface is determined, the second phase mentioned in the hypothesis starts. This involves the transformation of the spectral domain to the spatial domain by assuming a random-phase model with random phases uniformly distributed between $0 \leq \underline{\alpha} \leq 2\pi$. The discrete spectrum is then divided into equal wave-number bands denoted as Δk. Each gradient has been calculated by using the subsequent wave-number over the band width in the spectrum. In the spectrum the wave-numbers on the x-axis are plotted on logarithmic scale, which makes it more difficult to choose a step size. If the step size is very small, then the required computational time would be too large. And the other way around, if the step size is too large, then details in the spectrum will be ignored. Initially, a band width of $\Delta k = 1$ is assumed as a preliminary approximation. To determine the effect of the step size on the gradient different values for Δk are used. An effective method to determine the effect of the step size on the gradient is to make the step size small enough until one no longer notices the difference in the gradient. Apparently, when a step size of $\Delta k = 5$ is chosen, then the gradient will be smaller. For step sizes smaller than 1 ($\Delta k < 1$), no discernible difference is observed in the gradient. However, due to the long computational time of steps smaller than 1, the initial assumption of selecting a step size of 1 is chosen. Given the logarithmic scale, a potential alternative for future studies is to divide the spectrum into various step sizes of Δk. This approach facilitates more precise signal computations, enabling improved accuracy in the analysis.

The step size in both spectral and spatial domain influence each other. The step size Δk in the spectral domain determines the total length of the record in the spatial domain. Whereas in the spatial domain the step size Δx determines the maximum wave-number. In a discrete wave record, the maximum frequency that is not aliased is called the Nyquist frequency, see Vermeer (2012). Since the sampling of a function i(x) in space is entirely analogous to sampling a time function, the period T can be replaced by wavelength λ, and frequency f by wave-number k (Vermeer, 2012). The theoretical importance of the relationship between the two domains is shown in eq. (4.1) and (4.2):

$$\Delta x = \frac{\pi}{k_{max}} \tag{4.1}$$

and as spatial length of the record L:

$$L = \frac{2\pi}{\Delta k} \tag{4.2}$$

in which π and 2π derive from the wavelength $\lambda = \frac{2\pi}{k}$.

Damping effect in the filter layer

Another way to look at the influence of the step size, is by describing a physical boundary for the smallest eddies. If we focus on a situation where the forces directly influence the base material, which means without a filter layer, then the maximum wave-number (or minimum gradient) is equal to the diameter of the grains. Wave-numbers lower than this diameter do not contribute to the forces on the grain, see Booij (1998). However, in the case of a geotextile, the base material is also protected by the filter layer and the forces must first penetrate this layer. The filter layer has a damping effect on these forces which results in dissipation of the pressure fluctuations. To understand the damping effect of pressure fluctuations in the filter layer, reference is made to the gradients in (wave-induced) pressures in linear wave theory. When the energy of a wave passes through water, the energy sets water particles into orbital motion. This motion decreases when the particle descends deeper in the water, see figure 4.7 (left). In deep water when the water depth is larger than half the wavelength ($h > 1/2\lambda$), the water is unaffected by the wave energy and no wave motion occurs.

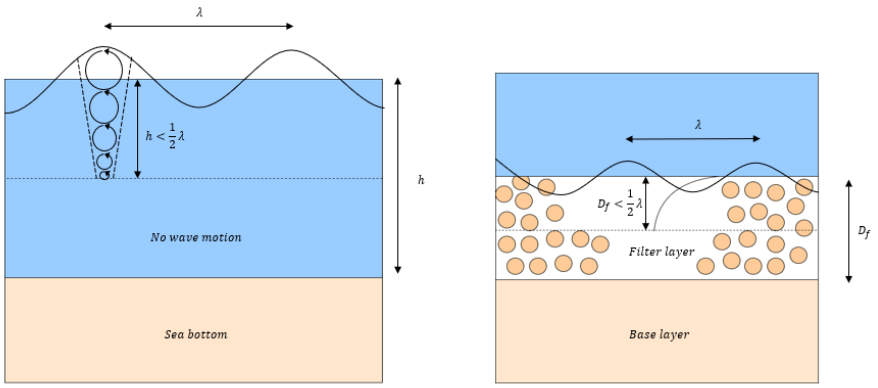

Figure 4.7: Damping effect in deep water (left) and in the filter layer (right).

With the application of the hypothesis, the pressure fluctuations are defined at the top of the filter layer (at $z = 0$). The above theory is applied to describe pressure penetration within the filter layer, as has been explained in deep water. The theory suggests that gradients corresponding to wavelengths shorter than twice the filter thickness ($D_f > \frac{1}{2}\lambda$) experience damping within the filter, as depicted in figure 4.7 (right). Previous experiments have demonstrated exponential damping of pressure fluctuations with increasing depth within a gravel layer, as observed in Klar (2005). In order to evaluate this theory within the hypothesis, it is assumed that the maximum wave-number does not exceed twice the filter thickness. This maximum damped wave-number is denoted as k_{D_f} and can be defined as follows:

$$D_f = \frac{1}{2}\lambda_{D_f} \quad \rightarrow \quad k_{D_f} = \frac{\pi}{D_f} \tag{4.3}$$

in which the maximum damped wave-number, denoted as k_{D_f}, can be determined as $\frac{2\pi}{\lambda_{D_f}}$. In the case of test T01, the filter thickness is 20 mm (refer to table 4.4). According to equation (4.3), the corresponding k_{D_f} value would be 157 m^{-1}. Figure 4.8 illustrates the pressure gradient spectrum for test T01 case 1, with the vertical dotted line representing the maximum damped wave-number k_{D_f}. The figure on the right provides a closer view of the spectrum. On the right side of the dotted line, the wave-numbers exceed k_{D_f}, and as a result, that portion is disregarded during the transformation to the spatial domain.

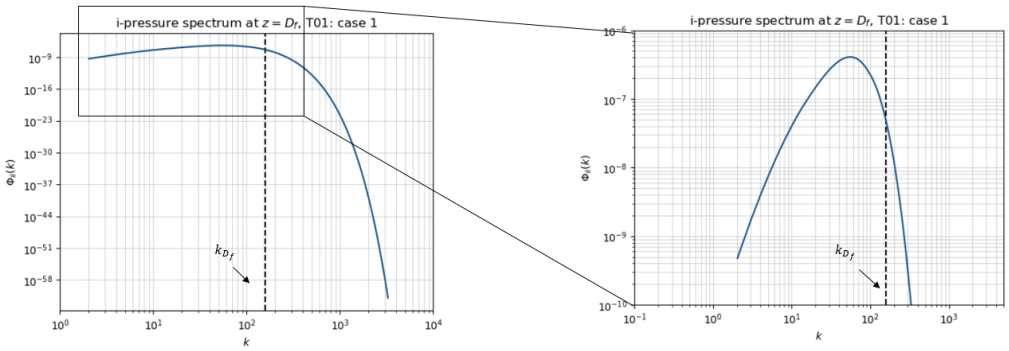

Figure 4.8: Dotted vertical line presenting the maximum damped wave-number k_{Df}.

Following eq. (3.18), the spatial record of figure 4.8 can be made. In order to determine the effect of the wave-number "cut-off" on the actual gradient, figure 4.9 shows the spatial record of the "untouched" spectrum in the left figure, and shows in the right figure the spatial record of the "cut-off" spectrum with k_{Df}. The number of gradient points in the spatial record are respectively,$N_p = 6551$ and $N_p = 315$.

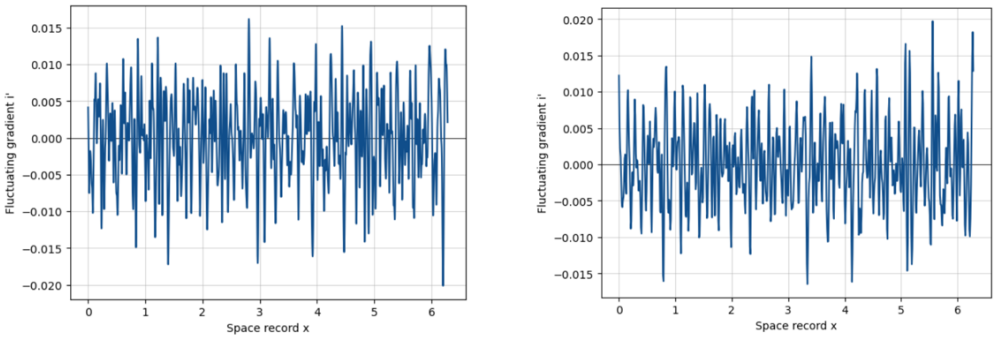

Figure 4.9: The spatial record for the "untouched" spectrum (left), and for the "cut-off" spectrum (right).

When comparing the spatial records in figure 4.9, no noticeable differences can be observed. However, a clear distinction can be observed when the gradients are presented in a histogram, as shown in Figure 4.10. The histogram reveals that the fluctuating gradient is approximately 0.90 times smaller for the "cut-off" spectrum compared to the complete spectrum. Furthermore, the number of gradient points is significantly reduced for the "cut-off" spectrum ($N_p = 6551$ to $N_p = 351$). This difference can be described by the right side of the dotted line that was neglected in figure 4.8. An advantage is that the computational time is significantly reduced when this area is ignored, enabling the computation of larger spatial records.

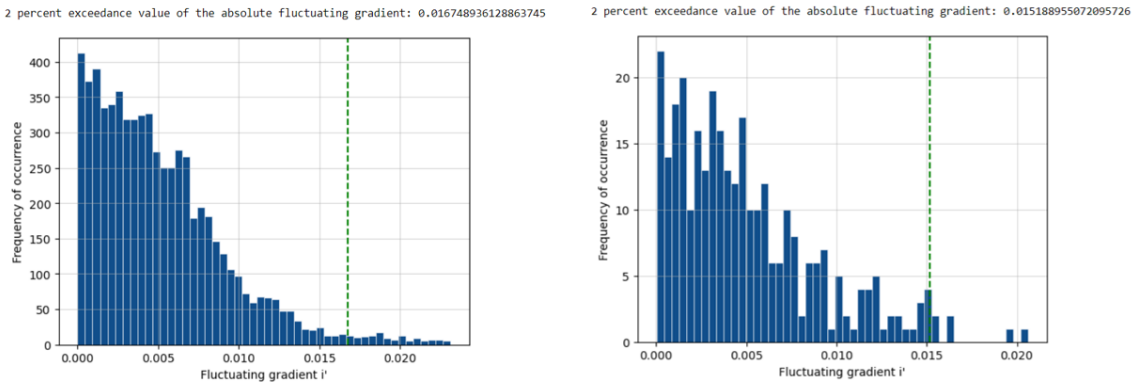

Figure 4.10: The histogram for the "untouched" spectrum (left), and for the "cut-off" spectrum (right).

Length of the signal

The fluctuating gradient is influenced by the length of the signal from which it is extracted. Increasing the total length of the signal leads to higher maximum gradients and converges the 2 percent exceedance value for the gradients to a constant. This effect is illustrated in Figure 4.11, which demonstrates the impact of signal length. The total length of the signal is determined by multiplying the number of repetitions of the record N by the length of the spatial record, denoted as L. In this context, the analysis is conducted for three cases: $N = 1$, $N = 10$, and $N = 100$. By computing the 2 percent exceedance value from the histograms, it is observed that the fluctuating gradient ($i'_{2\%}$) remains nearly constant, with a small difference of approximately ± 0.001. This small difference can be explained by the random phase model, with random phases uniformly distributed between $0 \leq \underline{\alpha} \leq 2\pi$, that is employed in the transformation from the spectral domain to the spatial domain.

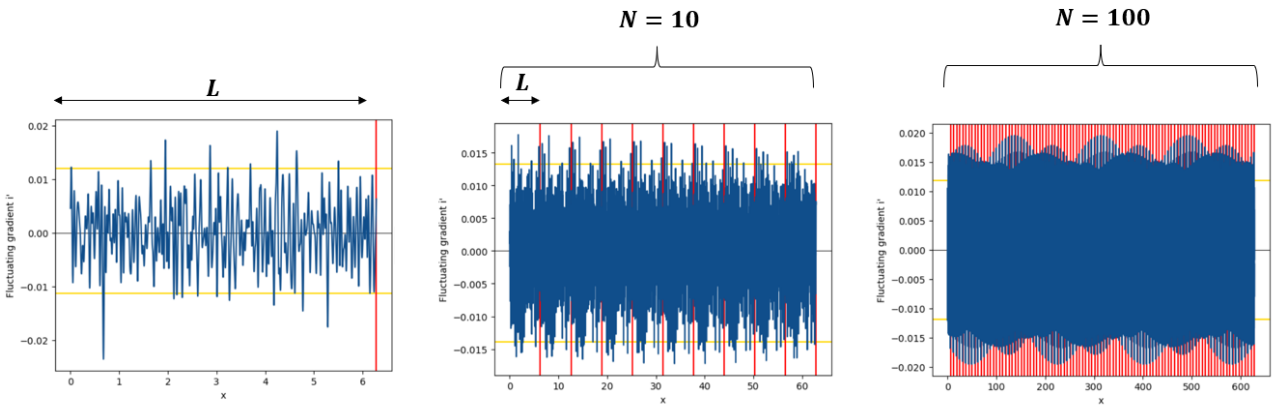

Figure 4.11: The spatial record for N=1, N=10 and N=100.

At this point, then, the gradient for the fluctuating pressures is derived from the histogram (figure 4.10 (left) and is ≈ 0.015 [-]. The average gradient is calculated according to eq. (2.26):

$$\bar{i} = \frac{u_*^2}{gh} = \frac{0.0326^2}{9.81 \cdot 0.067} = 0.00162 \quad [-] \tag{4.4}$$

The actual gradient derives from the average and fluctuating gradient, see eq. (3.19):

$$i_{a,2\%} = \bar{i} + i'_{2\%} = 0.0016 + 0.015 = 0.017 \quad [-] \tag{4.5}$$

4.2.3 Stability parameter for the hypothesis

To assess the stability at the filter/base interface, an additional step is necessary beyond the previously discussed hypothesis. Using this approach, an actual gradient of 0.014 [-] was determined for case 1 T01. The stability at the filter/base interface is determined by the transportation of base material through the filter layer. When the actual gradient remains below the critical gradient, no transport occurs, indicating a stable condition for the filter. This observation aligns with the design criteria proposed by Schiereck (2012).

The critical gradient is calculated with the formula of De Graauw (1983), see eq. (2.43). For this, the critical shear velocity is described according to Shields, see eq. (4.6). According to CUR (2012) realistic values for the relation between the critical stability parameter of the filter material and base material are between $\frac{\Psi_{c,f}}{\Psi_{c,b}} = 1.3$ and $\frac{\Psi_{c,f}}{\Psi_{c,b}} = 1.5$. From Shields curve (figure 2.9) can be seen that, when the diameter of the filter material is larger than 7 mm, the critical stability parameter for the filter material is constant. On the assumption of occasional movement of grains, see section 3.2, this parameter results in $\Psi_{c,f} = 0.03$. The stability parameter for the base material lays in the range from $\Psi_{c,b} = 0.023$ and $\Psi_{c,b} = 0.020$. Assuming the latter, the following critical shear velocity can be found according to Shields:

$$u_{*c} = \sqrt{g \Delta d_{b50} \Psi_{c,b}} = \sqrt{9.81 \cdot 1.63 \cdot 0.0003 \cdot 0.020} = 0.01 \quad [m/s] \tag{4.6}$$

in which the relative density ($\Delta = (\rho_b - \rho_w)/\rho_w$) follows from the density of the filter material, see table 4.3, and the water density ($\rho_w = 1000$ $[kg/m^3]$). The critical gradient, see eq. (2.43), follows:

$$i_c = \left[\frac{0.06}{0.43^3 \cdot 0.00742^{4/3}} + \frac{0.43^{5/3} \cdot 0.00742^{1/3}}{1000 \cdot 0.0003^{5/3}} \right] \cdot 0.01^2 = 5.6 \quad [\%] = 0.056 \quad [-] \tag{4.7}$$

in which n_F is the porosity of the filter, see table 4.3. The transport of the base material as a function of the gradient follows from eq. (3.19) and eq. (2.43). Therefore, the stability at the filter/base interface, where the geotextile is located, can be assessed as follows:

$$\frac{i_a}{i_c} < 1 \quad : \text{Stable} \tag{4.8}$$

Meaning that as long as the actual gradient is smaller than the critical gradient, there will be no sandy material from the base layer passing through the geotextile. This produces a stable filter design. In practice, this stability parameter could be higher, for example, in Wolters & Van Gent (2012) this value was found at 2-4. The stability parameter for case 1 of test T01 follows from the calculated actual and critical gradient:

$$\frac{i_{a,2\%}}{i_c} < 1 \quad \rightarrow \quad \frac{0.017}{0.056} = 0.30 \quad [-] \tag{4.9}$$

Eq. (4.9) shows that the actual gradient is 4 times smaller than the critical gradient, which means that for case 1 of T01 there is no transport of base material according to the actual gradient calculated with this hypothesis. With eq. 4.8 the stability at the filter/base interface can be determined. The results of the other test cases can be found in appendix A. Table 4.6 shows an overview of all stability parameters as determined by the approach of the hypothesis. The cells in the table that are highlighted with a yellow background, indicating a stable filter based on the conclusions drawn by Van de Sande (2012).

	T01	T02b	T03	T04	T06a	T07
	i_a/i_c [−]	i_a/i_c [−]	i_a/i_c [−]	i_a/i_c [−]	i_a/i_c [−]	i_a/i_c [−]
Case 1.	0.30	0.69	0.23	0.20	0.19	0.17
Case 2.	0.46	0.91	0.27	0.20	0.24	0.63
Case 3.	0.86	3.84	0.50	0.70	0.32	0.98
Case 4.	0.98	3.71	0.77	0.68	0.73	1.32
Case 5.	2.92	-	1.40	1.01	0.71	1.32
Case 6.	-	-	1.36	2.00	0.91	-
Case 7.	-	-	1.66	-	2.08	-

Table 4.6: Stability parameters at the filter/base interface.

In order to find out whether the base material is indeed stable at the filter/base interface, which means that there is no occasional movement of base material, the gradient ratio in eq. (4.8) is compared with the transport of base material. Van de Sande (2012) measured the amount of transported base material and plotted this against the mean velocity. In this way he could determine the value of the mean velocity that results in transport of base material; this he, then, defined as the critical value. The amount of transported base material is being defined as the transported material divided by the width of the flume and the duration of the test in g/m/h. The transported material q_s is made dimensionless as follows:

$$q_s^* = \frac{q_s \cdot \rho_s}{\rho_s \sqrt{\Delta g d_{b50}^3}} = [-] \tag{4.10}$$

The dimensionless form of transport q_s^* is plotted against the gradient where the latter is determined by the hypothesis. Figure 4.12 shows the stability parameters of table 4.6 on the x-axis and the dimensionless transport on the y-axis. Each value of the dimensionless transport corresponds to the amount of transported base material measured in the experiments of Van de Sande (2012) for a given mean velocity. This same mean velocity, then, is applied as the scaling parameter for the fluctuating gradient in the hypothesis.

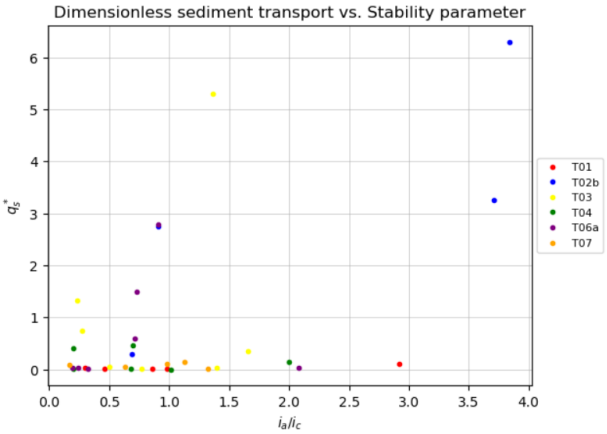

Figure 4.12: Dimensionless transport of base material vs. stability parameter.

4.3 Verification of the hypothesis with Wolters & Van Gent (2012)

Section 4.2 provides the verification of the hypothesis using the dataset utilized by Van de Sande (2012). As direct measurement of gradients was not undertaken in the study by Van de Sande (2012), stability was assessed based on the critical velocity. Ideally, if the critical velocity is inserted in the approach of the hypothesis, this would result in the threshold value at which the actual gradients become larger than the critical gradient (eq. 4.8).

Wolters & Van Gent (2012) conducted physical model tests where direct measurements of gradients were taken at the filter/base interface. The properties of the flume can be found in Wolters & Van Gent (2012). The granular filter material used in their experiments was subjected to waves, currents, and wave & current loading. The tests conducted under current conditions in Wolters & Van Gent (2012) are particularly relevant to our hypothesis, as it is based on uniform flow conditions. By comparing the gradients obtained in these tests with the approach of our hypothesis implemented under similar flow conditions, we can assess their compatibility. Table 4.7 presents the test conditions and measured gradients from Wolters & Van Gent (2012) specifically when the filter material was exposed to currents. These test conditions correspond to the red triangles depicted in Figure 2.24.

Current data	u_0 $[m/s]$	h $[cm]$	u_* $[m/s]$	d_{fn50} $[mm]$	D_f $[mm]$	i_c $[-]$	$i_{a,2\%}$ $[-]$
T01	1.25	40	0.122	22	55	0.039	0.047
T08	1.06	40	0.103	22	55	0.039	0.090
T10	0.63	40	0.062	22	55	0.039	0.074

Table 4.7: Test parameters and measured gradients under current loading (Wolters & Van Gent, 2012).

To determine the actual gradient for the input parameters provided in table 4.7, the same methodology outlined in section 4.2 is followed to calculate $i_{a,2\%}$. As the procedure has already been described in detail, table 4.8 presents the resulting gradients. For the steps outlined in the flowchart, please refer to Appendix **??**.

	Hypothesis		
Current data	i'	$\bar{i}$	$i_{a,2\%}$
T01	0.068	0.0038	0.072
T08	0.054	0.0027	0.057
T10	0.018	0.0010	0.019

Table 4.8: Gradients calculated with the approach of the hypothesis.

4.4 Summary - Verification of the hypothesis

The hypothesis was verified using measured data from Van de Sande's experiments as well as Wolters & Van Gent (2012). Van de Sande (2012) verified Hoffmans's design method for parallel flow conditions, where the critical velocity determined the threshold for base material transport through the filter layer. By incorporating Van de Sande's dataset into the scaling parameters of the dimensionless pressure spectra, the fluctuating gradients at the filter/base interface were calculated. To assess the stability of the filters, an additional step was introduced: the critical gradients. This enabled the application of criteria for open filters. In Wolters & Van Gent (2012), the stability of the filter layer was correlated with gradient measurements obtained at the filter/base interface. This allowed for a direct comparison of the gradients with those obtained from the hypothesis approach. The interpretation and comparison of these results with those of Van de Sande are discussed in Chapter 5.

5 | Analysis and discussion

This chapter focuses on the analysis of the test results presented in chapter 4. In section 5.1, the interpretation of these results is discussed, highlighting the differences compared to the findings of Van de Sande and Wolters & Van Gent. Furthermore, in section 5.2 the assumptions made in chapters 3 and 4 are thoroughly examined to identify potential modifications in the approach of the hypothesis that could enhance the results, bringing them closer to the measured datasets. As each step of this approach is demonstrated using the T01 test case, the analysis in this section also involves a detailed examination of this particular test case. Additionally, section 5.3 explores the potential adaptations required for its use under wave conditions.

5.1 Interpretation of the results

In this section, we discuss the results of the tests conducted in Chapter 4, where we verified the approach of the hypothesis using experimental data from Van de Sande (2012) and Wolters & Van Gent (2012). The differences between the measured datasets and the hypothesis can be explained for both experiments. In Van de Sande (2012), Hoffmans's method is based on the relationship between the properties of the filter and base material, while the hypothesis focuses on the actual gradients in the pressure that initiate grain motion. Eq. (2.48) takes the load indirectly into account, and with the properties of the selected material, the filter can be designed. In contrast, the hypothesis directly considers the loads by incorporating them as scaling parameters in the dimensionless pressure spectrum (see eq. (3.1) and (3.2)). Turning our attention to Wolters & Van Gent (2012), the transport of bed material as a function of the hydraulic gradient $i_{2\%}/i_c$ is described, where gradients were directly measured at the filter/base interface. Based on the measurements, an empirical transport formula was proposed (see eq. (2.50) and figure 2.24). The difference in this hypothesis lies in the attempt to describe the actual gradient from a pressure spectrum, whereas Wolters & Van Gent (2012) measured it directly at the filter/base interface.

5.1.1 Results compared to Van de Sande (2012)

In Van de Sande (2012), the velocity in the experiments was increased to a point (the so-called critical velocity) at which the material begins to move. This could be either filter material or base material. In the hypothesis of this study the same increasing velocities were used with the corresponding parameters (see table 4.5), and aims to find results equal to that of Van de Sande (2012). The hypothesis then is that this critical velocity at which the movement of base material begins, specifies the threshold value of any unstable filter. In the hypothesis, this means that the actual gradient should be smaller than the critical gradient for velocities below this critical velocity value, and thus yields a stable filter, see eq. (4.8). Whereas the filter becomes unstable with critical velocity values that surpass this value. Table 5.1 shows qualitative analysis of the stability of the filter layer described by Van de Sande (2012) and the hypothesis.

T01	Mean velocity u_0 $[m/s]$	Van de Sande (2012)	Hypothesis
Case 1.	0.30	Stable	Stable
Case 2.	0.40	Stable	Stable
Case 3.	0.55	Stable	Stable
Case 4.	0.60	Stable	Stable
Case 5.	1.00	Unstable	Unstable

Table 5.1: Qualitative analysis for the stability of the filter between the hypothesis and Van de Sande (2012).

In Van de Sande (2012), the stability of the filter is defined by the critical velocity; for test T01 the outcome is 1.00 m/s, see table 4.4. As discussed in previous chapters, the stability of the filter is characterized by the relationship between the actual and critical gradients. Table 4.6 presents the stability parameter calculated according to the hypothesis for all tests. The results indicate that test cases 1 to 4 describe a stable filter,

while test case 5 represents an unstable filter. These findings align with Van de Sande's observations (2012), which suggest that base material transport through the filter layer occurs when the mean velocity reaches 1.00 m/s, indicating an unstable filter. However, not all tests yield similar results. For instance, in test T04, Van de Sande recorded an unstable filter at a critical velocity of 0.85 m/s (see table A.12), whereas according to the hypothesis, the stability parameter for a mean velocity of 0.60 m/s (case 5) is 1.01 [-], as determined by eq. (4.8). This indicates that the actual gradient is larger than the critical gradient, suggesting an unstable filter for case 5.

According to the data presented in figure 4.12, it can be observed that the stability parameter exhibits a value that is three times larger than the stability parameter defined by Schiereck (2012), while not inducing any significant transport of base material. This finding aligns with previous experimental investigations, such as the study conducted by Wolters & Van Gent (2012), which similarly demonstrated that the stability parameter could reach values that are two to three times larger, while still not resulting in notable base material transport.

5.1.2 Results compared to Wolters & Van Gent (2012)

In Wolters & Van Gent (2012), the gradients were measured at the filter/base interface, allowing for a direct comparison of the results with those obtained in the hypothesis. Table 5.2 presents the quantitative analysis of the actual gradients determined using the pressure spectrum in the hypothesis and the measurements from Wolters & Van Gent (2012).

		Hypothesis	Wolters & Van Gent (2012)
Current data	Mean velocity u_0 $[m/s]$	$i_{a,2\%}$ $[-]$	$i_{a,2\%}$ $[-]$
T01	1.25	0.072	0.047
T08	1.06	0.057	0.090
T10	0.63	0.019	0.074

Table 5.2: Quantitative analysis for the actual gradient between the hypothesis and Wolters & Van Gent (2012).

The results in table (5.2)revealed that the calculated gradients exhibited a comparable magnitude, ranging from 0.25 smaller to 1.50 larger in comparison to the measured gradients reported by Wolters & Van Gent (2012). This indicates a reasonably close agreement between the calculated and measured gradients.

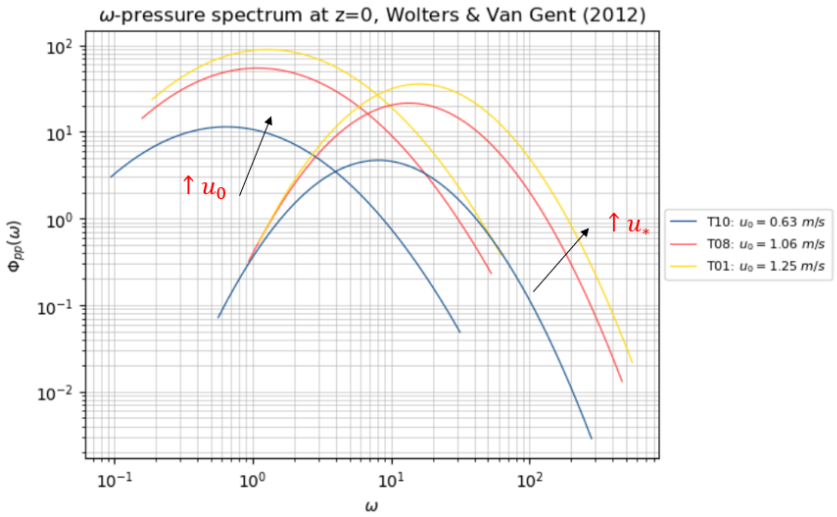

Figure 5.1: Pressure spectrum of current data Wolters & Van Gent (2012).

In the current tests conducted by Wolters & Van Gent (2012), the velocity in the flume increases while keeping the water depth and stone size constant. In the dimensional pressure spectrum, this translates to an increase in spectral density $\Phi_{pp}(\omega)$. Additionally, a slight shift to the right side of the spectrum is observed, indicating a shift towards higher frequencies. Applying the approach of the hypothesis to determine the actual gradients, this results in an actual gradient that is 3.8 times larger when the mean velocity is doubled.

5.2 Analysis of the hypothesis

This section focuses on discussing the assumptions made in Chapter 4 that could potentially impact the actual gradient value. It is important to note that some of these assumptions have already been discussed in Chapter 4, such as the step size Δk, the random phase and the length of the signal. Therefore, they will not be reiterated in this section.

5.2.1 Combining the dimensional pressure spectra

To determine the actual gradient in the hypothesis, the dimensional curves scaled on the outer variables and scaled on the inner variables are combined by connecting the peaks with a line. This concept is illustrated in figure (4.5), where an additional area has been included in the spectrum, increasing the spectral density. It was assumed that this inclusion would result in a more conservative estimate of the actual gradient. To assess the impact of this small area in the spectrum, the actual gradient is also calculated when the dimensional curves intersect at the intersection point. Figure 5.2 displays the intersection point for test T01: case 1.

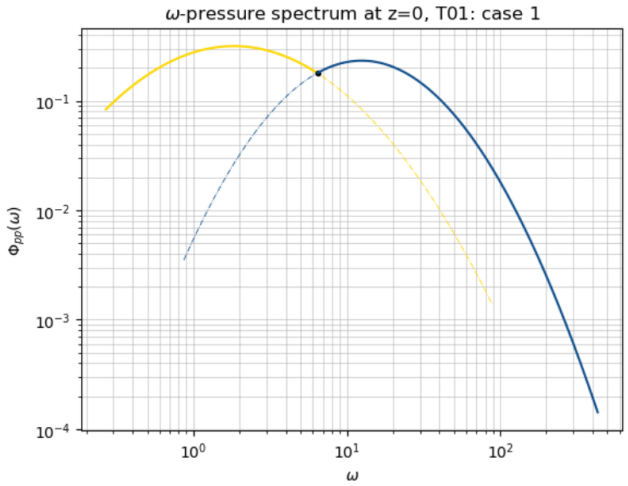

Figure 5.2: Intersection point combining both pressure spectra.

The spatial record and histogram of the fluctuating gradient, obtained through the steps outlined in the determination of the fluctuating gradient (which are not elaborated here as they align with those discussed in Chapter 4), are presented in Figure 5.3.

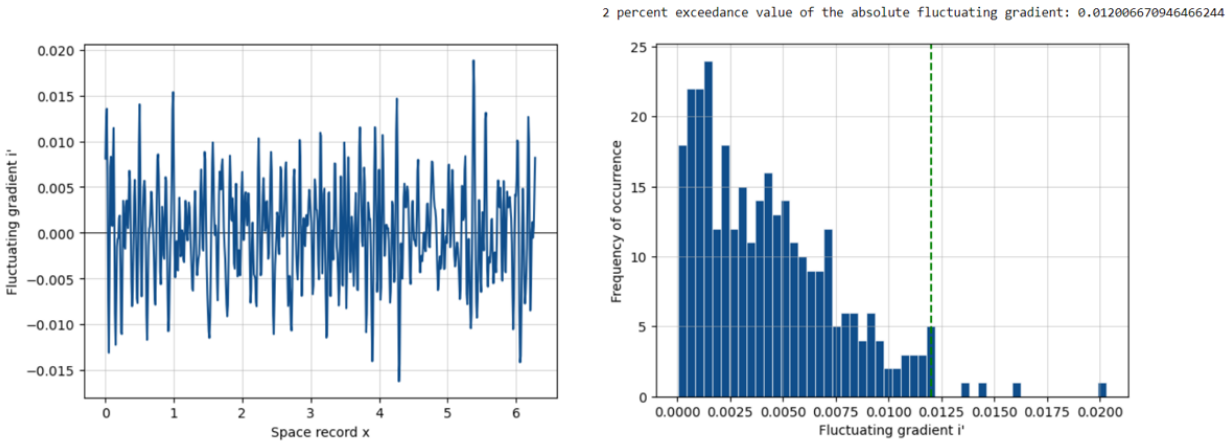

Figure 5.3: The spatial record and the histogram for the pressure spectrum merged at the intersection point.

The fluctuating gradient for the dotted line connecting the peaks of each spectrum is $i_{2\%} = 0.015$ [-], while for the intersected pressure spectra it is $i_{2\%} = 0.012$ [-]. Using eq. (3.19), this corresponds to an actual gradient of $i_{a,2\%} = 0.017$ [-] and $i_{a,2\%} = 0.014$ [-], respectively. Consequently, incorporating the small area added to the spectrum when combining the peaks results in an increase of 0.003 for the actual gradient. However, as the distance between the two dimensional curves widens, as shown in figure 4.4, the added area in the spectrum also increases. For example, in T01: case 2, the added area leads to an increase of 0.009 for the actual gradient. Given that the added value to the actual gradient increases when combining both peaks and the distance between the two curves becomes wider, it is recommended to conduct further research into the optimal method of combining the spectra scaled on the outer and inner variables.

5.2.2 Scaling characteristics

Earlier research did show clearly how different regions of the pressure spectrum are influenced by sources from different regions. These sources refer to the scaling characteristics (or variables) that lead to the collapse of the spectrum within a well-defined frequency range. Numerous characteristics have been suggested by researchers while accounting for the relevant experimental conditions (Blake, 1970; Farabee and Casarella, 1991; Lee & Sung, 2002; Meyers *et al.*, 2015). These conditions may vary depending on the properties of the wall: smooth or rough walls. They may also vary depending whether there is an equilibrium or non-equilibrium turbulent boundary flow. According to the theory on the TWP spectra for rough walls, as derived from windtunnel measurements, research has proven that there is an universal scaling for high-frequency regions (Meyers *et al.*, 2015; Joseph *et al.*, 2020). These universal scaling variables differ from the variables proposed by Blake, see paragraph 2.4.4. Yet, the spectra of Blake were applied in our hypothesis, since it offered the most suitable depiction of the scenario presented in this study involving geotextiles, see figure (2.18).

Hofland (2005) demonstrated that near-bed processes in the high-frequency region exhibit similarities between rough and smooth walls. Specifically, he observed that the smooth wall wind tunnel spectra, as discovered by Lee & Sung (2002), overlap with the rough wall spectra in the high-frequency range of his experiments. For the low-frequencies, the spectra probably are different, but this has not yet been proven. Also, it is still unknown which scaling characteristics for this part of the spectrum are to be used. As an initial assumption for our hypothesis, we selected the mean velocity u_0 and water depth h as the scaling characteristics for the low-frequency region. In Chapter 4, these scaling characteristics were employed using the values obtained from the datasets of Van de Sande and Wolters & Van Gent. Figure 4.4 displays the pressure spectrum, which was made dimensional by implementing the scaled outer and inner variables based on the dataset of Van de Sande (2012). This figure clearly illustrates the distinct separation between the low-frequency and high-frequency regions. It also highlights the slowly rising low-frequency region and the rapidly decaying high-frequency region, as mentioned in the literature review by Blake (2017).

However, it should be noted that two alterations were made to the scaling parameters for the low-frequency region. Instead of using the free-stream velocity U_∞, the average velocity u_0 was utilized. Similarly, the displacement thickness layer δ^* was substituted for the water depth h in equation (3.1). Although the verification of the hypothesis demonstrates some resemblance to the measured datasets of Van de Sande and Wolters & Van Gent, further investigation is still required regarding the outer scaling characteristics.

5.2.3 Premultiplied spectrum analysis

In Chapter 3, it was explained that plotting the spectra on a double logarithmic scale enhances the visual perception of the slope within the spectrum, for example by $\Phi_{pp}(\omega) \propto \omega^{-1}$ in the overlap region. Another visualization approach is the use of a premultiplied spectrum, which allows for a comprehensive examination of the energy-containing range. The advantage of visually interpreting the energy-containing range of the wave-numbers is gaining insights into the dominant scales or wave-numbers where the pressure fluctuations exhibit the highest energy levels. Figure 5.4 illustrates the premultiplied spectrum for all T01 test cases. In 5.4, the area under the curve within a specific wave-number band, represented by ΔA, is proportional to the energy content within that band. By analyzing changes in the spectrum's area for different test cases or conditions, such as varying velocities, one can observe how the energy distribution varies across different scales.

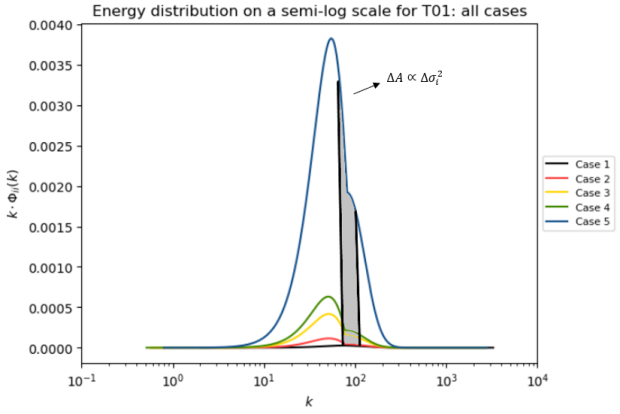

Figure 5.4: Premultiplied spectra describing the energy distribution of test T01 in Van de Sande (2012).

Based on the test cases of Van de Sande (2012), it becomes evident that the pressure fluctuations are most energetic in the smaller scales, particularly within the wave-number range of approximately $10^1 \leq k \leq 2 \cdot 10^2$. This indicates that the spectral density, representing the energy per unit wave-number, is highest within this specific range of wave-numbers. In order to see if the wave-number range of $10^1 \leq k \leq 2 \cdot 10^2$ indeed stands for the highest energy in the spectrum, the actual gradient is calculated for this specific range, see figure 5.5.

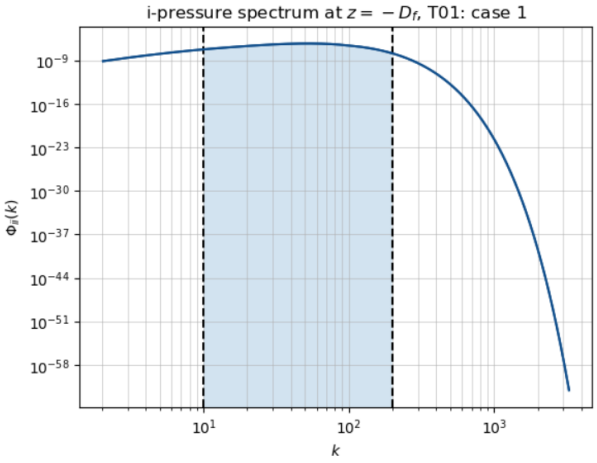

Figure 5.5: Area in the gradient spectrum according to the energy-containing wave-number range.

By utilizing the spatial record and following a series of additional steps, the actual gradient can be determined from the specific area in the gradient spectrum. For instance, considering only the blue area depicted in Figure 5.5, the calculated actual gradient is approximately 0.017 [-]. Notably, this value aligns with the gradient calculated from the spectrum in Chapter 4, see eq. (4.5), suggesting that the range of wave-numbers that encompasses the majority of the energy content can serve as a reliable indicator for gradient determination. This method holds potential as a valuable tool in future studies to describe the relevant area in the spectrum.

5.3 The hypothesis for waves

In this section, we explore the application of the hypothesis to wave conditions. One interesting aspect of the hypothesis is its connection to wave theory. By making a few adjustments, the hypothesis can be adapted to describe and be verified with wave datasets. Instead of utilizing a dimensionless pressure spectrum, the approach for waves can be derived from existing spectra, such as the JONSWAP (Joint North Sea Wave Project) spectrum shown in Figure 5.6. The JONSWAP spectrum is an empirical relationship that characterizes the energy distribution across a range of frequencies for wind-generated waves in oceanic waters. It is widely accepted and utilized as a design spectrum in the engineering community (Holthuijsen, 2007). For a comprehensive understanding of the JONSWAP spectrum, a thorough review by Holthuijsen (2007) is recommended.

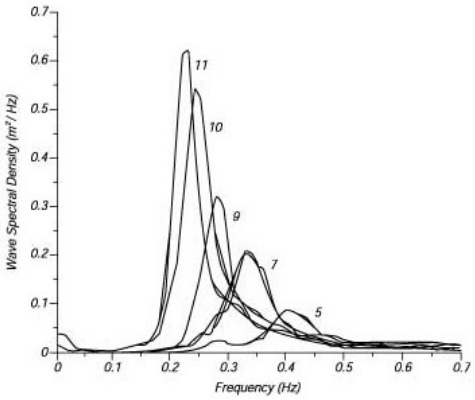

Figure 5.6: Spectra observed in JONSWAP under idealised, deep-water conditions according to Hasselmann *et al.* (1973).

Similar to the hypothesis formulated for uniform flow, the hypothesis for waves entails a set of underlying assumptions and simplifications. The same assumptions that were discussed in chapter 3 are valid for the hypothesis for waves. Specifically, the only external force on the waves is gravitation, which means that linear wave theory is valid. Additionally, it is introduced as an assumption that the waves remain unaffected by the presence of the porous filter layer, while assuming Darcy-flow (laminar flow) characteristics within the porous medium. Consequently, equations (3.12) and (3.13) can be derived specifically for waves. Figure 5.7 pictures, then, the new situation for waves. Note the difference in reference level of $z = 0$ (here located in the still-water level).

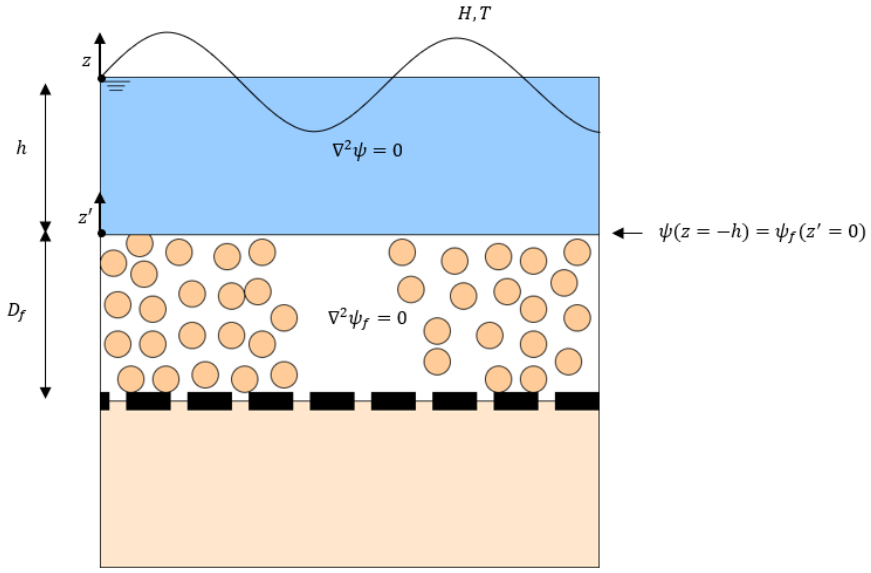

Figure 5.7: Pressure head ψ at the water/filter interface at $z = -h$ under waves.

The approach of the hypothesis for waves encompasses a few additional steps compared to that of uniform flow. Initially, the harmonic wave, which is characterized by the surface elevation η as shown in equation (2.4), is defined at the still-water level ($z = 0$). Consequently, an extra step involves the translation of the wave-induced pressure to the bed level ($z = -h$). Subsequently, the same procedure outlined in Chapter 3 can be followed to determine the fluctuating gradient, as described by equations (3.5) to (3.18). The transformation of the JONSWAP spectrum $\phi_{\eta\eta}(f, z = 0)$ at the still-water level to the pressure gradient spectrum $\phi_{ii}(k, z = D_f)$ at the filter/base interface is as follows:

$$\phi_{ii}(k, z = -D_f) = \frac{\phi_{\eta\eta}(f, z = 0) \cdot \frac{1}{2\pi} \cdot c_g \cdot k^2}{cosh(kh)^2 cosh(kD_f)^2} \tag{5.1}$$

The pressure gradient can be derived from the spectrum with the following function:

$$i'(x) = \sum_{n=\Delta k}^{N\Delta k} \sqrt{2 \cdot \Delta k \cdot \phi_{ii}(k, z = -D_f)} \cdot cos(k_n x + \underline{\alpha}_n) \tag{5.2}$$

The deduction of the gradient of the fluctuating pressures can be derived from equation (5.2). Subsequently, the 2% exceedance values of the gradients ($i'2\%$) can be determined through a histogram analysis. Notice how there is a resemblance of eq. (3.18) for uniform flow with eq. (5.2) for waves. However, the distinction lies in the nature of the spectra. For uniform flow, the spectrum represents the pressure spectrum, denoted in units of $[Pa^2/Hz]$, while for waves, it corresponds to the surface wave spectrum (JONSWAP) expressed in units of $[m^2/Hz]$.

5.4 Application of the critical filter velocity

In this section the application of the critical filter velocity is described as an alternative to the critical gradients. In absence of an approach to determine the critical gradients for geotextiles, we rely on the critical gradients identified by Lemmens (1996), see figure 2.4. As an initial observation of Lemmens' critical gradients, it appears peculiar that only one single value is associated with these critical gradients. One would expect a similar relationship as has been applied in the context of granular filters De Graauw (1983).

For granular open filters, the critical gradient incorporates the filter diameter, which implicitly determines the velocity. When the pore space varies due to smaller and larger stone sizes, water flows through at different velocities. Therefore, it is necessary to apply the critical velocity rather than the critical gradient. This critical velocity determines the velocity for the threshold of moving grains. For the stability of the filter layer, , the critical velocity can be found from the measured critical gradient and the Forchheimer equation, see eq. (2.34). Since the only critical gradients that are available for geotextiles are derived from Lemmens's experiments, these gradients are utilized to determine the critical filter velocity. When focusing on jute cloth and also jute cloth filled with 4 cm of wood pulp, the critical filter velocities can be calculated as follows, respectively:

$$i_{c,1} = 0.26 = a u_{f,c,1} + b u_{f,c,1} |u_{f,c,1}| \tag{5.3}$$
$$i_{c,2} = 0.56 = a u_{f,c,2} + b u_{f,c,2} |u_{f,c,2}| \tag{5.4}$$

Lemmens (1996) conducted his experiments by the placement of stones - ranging from 80 to 200 mm - with a d_{f15} of 0.106 m according to the Rock manual, on top of a sand layer with a median particle size d_{50} of 145 μm. As some values did not occur in Lemmens's tests, the same values as applied by Van de Sande were adopted in our research, e.g. the porosity in the filter layer. For the calculation of the coefficients in the Forchheimer equation, a porosity of 0.4 and a kinetic viscosity of 10^{-6} m^2/s were assumed. In eq. (2.34), this gives for the coefficients a and b respectively 0.03 s/m and 7.01 s^2/m^2. Then, the critical filter velocity in the filter layer $u_{f,c}$ can be computed, resulting in a critical velocity of 0.19 m/s for the jute cloth and a critical velocity of 0.28 m/s for the jute cloth filled with 4 cm of wood pulp:

$$u_{f,c,1} = 0.19 \quad [m/s] \tag{5.5}$$
$$u_{f,c,2} = 0.28 \quad [m/s] \tag{5.6}$$

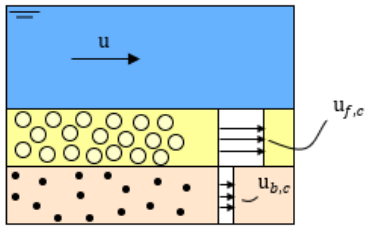

Figure 5.8: The velocity in the filter and base layer.

By rephrasing the critical gradient deduced from Lemmens in terms of velocities, this approach provides predictions for the critical filter velocities, see eq. (5.5) and (5.6) . This adjustment is necessary because the critical gradient includes the filter diameter, which indirectly affects the velocity. Consequently, to analyze the critical value for geotextile stability in terms of gradients implies an error. Instead, an alternative measure, namely the critical filter velocity, is proposed in this research project. The hypothesis, thus, posits that the critical filter velocity is expected to demonstrate relative consistency across different stone sizes, and it thereby renders a promising substitute for the gradient as argued by Lemmens. Confirmation of this hypothesis through empirical testing is recommended in order to establish its validity and reliability.

5.5 Summary - Analysis and discussion

The stability parameter in equation (4.8) theoretically yields two potential outcomes: a stable filter or an unstable filter. Upon examining the results presented in the hypothesis and comparing them with Van de Sande's findings (as shown in Table 5.1), it can be concluded that they align. However, it is important to note that not all tests yield similar results. For instance, in test T04, Van de Sande measured an unstable filter at a critical velocity of 0.85 m/s, whereas according to the hypothesis, the filter becomes unstable at a velocity of 0.60 m/s. It must be borne in mind that the stability parameter is based on the concept that when the actual gradient exceeds the critical gradient, the filter becomes unstable. Experimental studies, such as Wolters & Van Gent (2012), have shown that this parameter does not necessarily need to be strictly equal to 1. Values of 2 and 4 were measured without significant base material transport. Therefore, it can be concluded that while the stability parameter may suggest an unstable filter, it does not necessarily imply a significant amount of base material transport through the filter layer.

The comparison between the results of the hypothesis and those of Wolters & Van Gent (2012) revealed that the actual gradients obtained from both methods are within the same order of magnitude. An interesting finding observed from the results: an increase in flume velocity corresponded to an elevation in spectral density $\Phi_{pp}(\omega)$. Analysis of the hypothesis results indicated that doubling the average velocity resulted in an actual gradient that was 3.8 times larger. Moreover, a slight shift towards higher frequencies in the spectrum was also observed.

In the hypothesis a few assumptions where made that could potentially influence the value of the actual gradient. One such assumption pertains to the connection of the dimensional curves, which are scaled on the outer and inner variables. This concept is visually depicted in Figure 4.5, where an additional area is included in the spectrum, consequently increasing the spectral density. To assess the impact of this extra area, the actual gradient was also calculated when both curves merge at the intersection point, as illustrated in Figure 5.2. In accordance with test T01: case 1, combining the peaks with a line resulted in an increase of 0.001 in the actual gradient. However, as the distance between the two dimensional curves widens, the added area in the spectrum also increases. Therefore, it is recommended to conduct further research to determine the optimal method of combining the spectra scaled on the outer and inner variables.

In Chapter 4, an assumption was made regarding the damping of wavelengths shorter than twice the filter thickness within the filter layer. As a result, the spectrum can be "cut-off" at a point where these wavelengths are damped. Another approach involves utilizing a premultiplied spectrum, which enables a visual interpretation of the energy-containing range of wave-numbers within the spectrum. This provides valuable insights into the dominant wave-numbers where the pressure fluctuations exhibit the highest energy levels. Analysis of the test cases conducted by Van de Sande (2012) revealed that the pressure fluctuations are most energetic within the wave-number range of approximately $10^1 \leq k \leq 2 \cdot 10^2$. By focusing on this wave-number range within the spectrum, it was observed that the calculated actual gradient yields the same values as those determined in Chapter 4. This suggests that the range of wave-numbers that encompasses the majority of the energy content can serve as an indicator for gradient determination. The advantage of this method is its potential to serve as a valuable tool in future studies for accurately describing the relevant area in the spectrum. By identifying the wave-number range associated with the highest energy levels, the focus can be directed towards this specific part of the spectrum. Consequently, other areas that do not contain significant energy can be effectively neglected in future analyses.

The objective of our study is the development of a design method which applies to any context of uniform flow conditions. An important advantage is how, with a few modifications, the design method could also be extended to include wave conditions. When considering waves, the wave-induced pressure at still water level can be defined by using linear wave theory. Also, by following a similar approach in the hypothesis of the design method for uniform flow, it becomes possible to calculate the pressure gradients at the filter/base interface. In contrast to the use of a pressure spectrum in the approach for uniform flow, the approach for waves can incorporate a wave spectrum, such as the commonly used JONSWAP spectrum.

6 Designing a geotextile filter: an application

The main research objective in this study was to formulate a design method for geotextiles under a single granular filter layer. To achieve this, it was necessary to take some steps back and define the actual gradients, as well as identify the most suitable method for estimating these gradients. As a result, a hypothesis was formulated to determine the actual gradient at the filter/base interface. This hypothesis has been verified using two different datasets, and the results indicate a close agreement between the predicted and measured data.

With a clearer understanding of how to calculate the actual gradients at the geotextile interface, the same approach employed in the hypothesis is applied to address the design of a stable open geotextile under a single granular filter layer. This chapter focuses on the design of a stable geotextile, starting with the definition of an "open" geotextile for jute geotextiles in section 6.1. Subsequently, an application is presented in section 6.2, illustrating the design process for achieving filter stability.

6.1 "Open" geotextiles

The starting point of our research project were the experiments which Lemmens had conducted in 1996. His experiments revealed that jute exhibits similar sandtightness as conventional geotextiles when considering the sandtightness for the critical gradient. While synthetic geotextiles have fixed mesh sizes, jute geotextiles may experience fiber swelling, which leads to variable permeability at different locations within the fabric. To gain an understanding of this swelling effect, a filter fabric was submerged in water for two weeks until the jute fabric reached full saturation. Both cases involved measuring the pore size. The majority of the pore sizes of the dry filter fabric was measured to be approximately 1.5 mm, while in the case of the saturated filter fabric, the majority of the pore sizes is slightly reduced due to the swelling of natural fibers. However, even in the saturated state, the majority of the jute fabric maintained a pore size of approximately 1-1.5 mm.

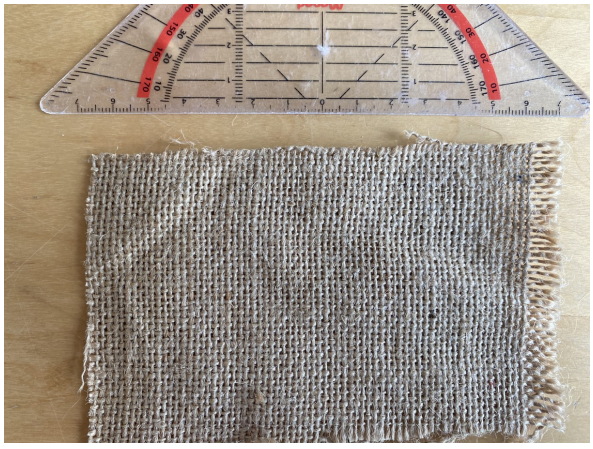

(a) Small piece of the dry jute material.

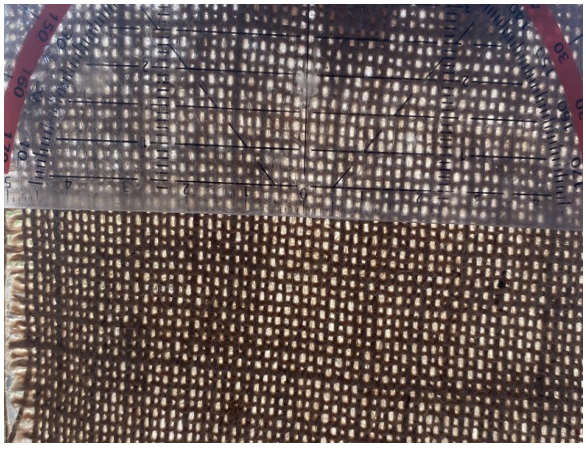

(b) Focused specifically on pore size.

Figure 6.1: The dry jute material from Van Aalsburg B.V.

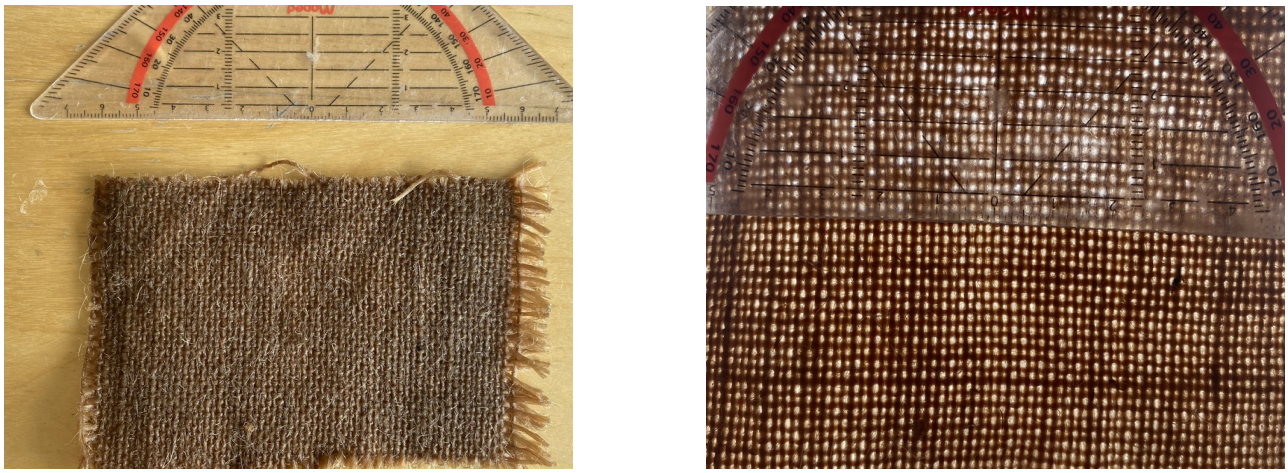

(a) Small piece of the saturated jute material.

(b) Focused specifically on pore size.

Figure 6.2: The saturated jute material from Van Aalsburg B.V.

In the introduction of this study, it was assumed that geotextiles fabricated from natural fibers possess an open structure. This assumption can be supported by examining the pore size of the jute fabric presented in figures 6.1 and 6.2. By analyzing these figures, it is possible to assume the opening size O_{90}, which represents the size at which 90% of the openings in a mesh grid are smaller. The visual inspection of the mesh grid in figures 6.1 and 6.2 indicates that the majority of the grid exhibits pore sizes ranging from 1 mm to 1.5 mm. This assumption further supports the earlier proposition that geotextiles composed of natural fibers can be regarded as open structures.

6.2 Design of a stable filter for a fictional case

This section introduces a fictional case study aimed at determining the parameters for designing a stable filter consisting of a geotextile and a single filter layer. The focus of this study is to determine the appropriate thickness of the granular filter layer. A schematization of the fictional case is presented in figure 6.3.

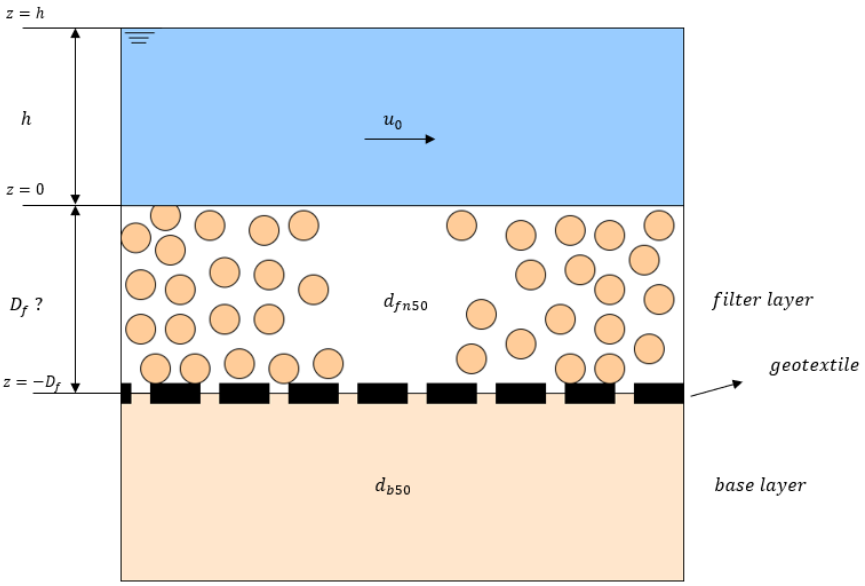

Figure 6.3: The schematization of the fictional case.

Table 6.1 presents the relevant parameters for the fictional case, some of which have been derived from measurements conducted by Van de Sande or Wolters & Van Gent (Δ, Ψ, n_f, ρ_s, ρ_s). The same diameter of the sand is used as in the experiments of Lemmens (1996).

List of given parameters			
b	3.0 $[m]$	ρ_s	2600 $[kg/m^3]$
h	5.0 $[m]$	ρ_w	1000 $[kg/m^3]$
u_0	1.00 $[m/s]$	Δ	1.60 $[-]$
c_f	0.0038 $[-]$	Ψ	0.02 $[-]$
n_f	0.40 $[-]$	d_{b50}	145 $[\mu m]$

Table 6.1: List of given parameters for the fictional case.

In this fictional case stone type A, with a nominal diameter of 10 mm, will be tests under uniform flow. Based on the data provided in table 6.2, the input parameters are known and could be implemented in the dimensionless pressure spectrum of Blake. The steps to determine the actual gradient which are presented in the hypothesis are shown for this fictional case. Table 6.2 provides an overview of the input parameters for stone type A.

	u_0 $[m/s]$	h $[m]$	u_* $[m/s]$	d_{fn50} $[m]$
Stone type A	1.00	5.0	0.0613	0.01

Table 6.2: Input parameters for fictional case.

Hypothesis for the actual gradient

To determine the actual gradient, the first step is to calculate the fluctuating gradients from the pressure spectra. By inputting the parameters from table 6.2 into eq. (6.1) and (6.2), the dimensional rough wall pressure spectra can be obtained:

$$\frac{\Phi(\omega)}{u_0^3 c_f^2 \rho_w^2 h} \quad \text{vs.} \quad \frac{\omega h}{u_0} \quad \text{(outer)} \tag{6.1}$$

$$\frac{\Phi(\omega)}{u_*^3 \rho_w^2 d_{n50}} \quad \text{vs.} \quad \frac{\omega d_{n50}}{u_*} \quad \text{(inner)} \tag{6.2}$$

The resulting dimensional pressure spectrum at $z = 0$ is depicted in figure 6.4.

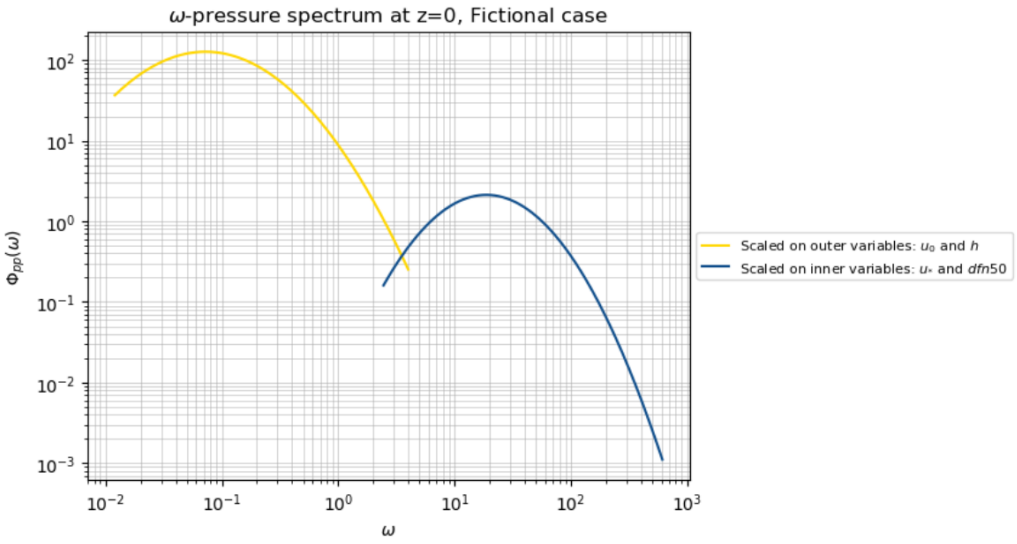

Figure 6.4: The frequency pressure spectrum of the geotextile for the fictional case.

The next step involves combining the dimensional curve scaled on the outer variables (u_0 and h) with the curve scaled on the inner variables (u_* and d_{n50}) by drawing a line between the peaks. This is illustrated in figure 6.5. It should be noted that the area added by this line contributes little to the total actual gradient, as discussed in section 5.2.1.

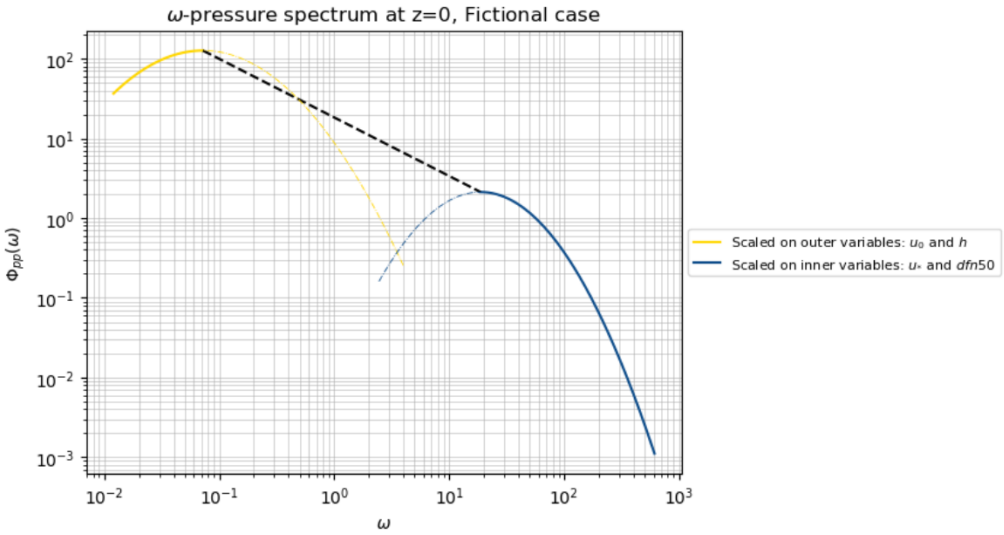

Figure 6.5: Combining both dimensional pressure spectra of the geotextile for the fictional case.

To convert the frequency spectrum into the wave-number spectrum, the spectral density is multiplied by the convection velocity, which is assumed to be 0.44 times the average velocity. Simultaneously, the angular frequency is divided by the convection velocity, as demonstrated in equations (6.3) and (6.4):

$$\Phi_{pp}(k) = \Phi_{pp}(\omega) \cdot 0.44 \cdot u_0 = \Phi_{pp}(\omega) \cdot u_c \tag{6.3}$$

$$k = \omega/(0.44 \cdot u_0) \tag{6.4}$$

Subsequently, the wave-number pressure spectrum is transformed into the gradient spectrum using eq. (6.5) (see for reference eq.(3.11)).

$$\Phi_{ii}(k, z = 0) = \Phi_{pp}(k) \cdot (\frac{k}{\rho_w g})^2 \tag{6.5}$$

At this point, the spectrum is described at the top layer of the filter ($z = 0$). To determine the spectrum at the filter/geotextile interface, eq. (3.15) is utilized, where the unknown filter thickness D_f is assumed to be three times the nominal diameter of the stone, resulting in a filter layer of 30 mm for the first iteration:

$$\Phi_{ii}(k, z = -D_f) = \frac{\Phi_{ii}(k, z = 0)}{cosh(kD_f)^2} \tag{6.6}$$

As can be seen in the equation is that in here the filter thickness D_f is used. Since, the thickness is unknown, an initial assumption is made to assess whether the actual gradients lead to a stable filter design. If not, an iterative process is conducted until a stable design method is identified. For the initial assumption, a filter thickness D_f of 30 mm filter layer is assumed. The gradient spectrum, as illustrated in figure 6.6 based on eq. (3.15), showcases the dotted vertical line representing the theory of the "deep water limit." This theory suggests that the maximum damped wave-number k_{D_f} acts as an upper limit, indicating that wave-numbers larger (or wavelengths smaller) than this value are hypothesized to be damped within the filter layer. Furthermore, it is important to observe the slight discontinuity at the wave-number of $4 \times 10^1 \mathrm{m}^{-1}$. This point represents the intersection between the peak of the curve scaled on the inner variables and the dotted line.

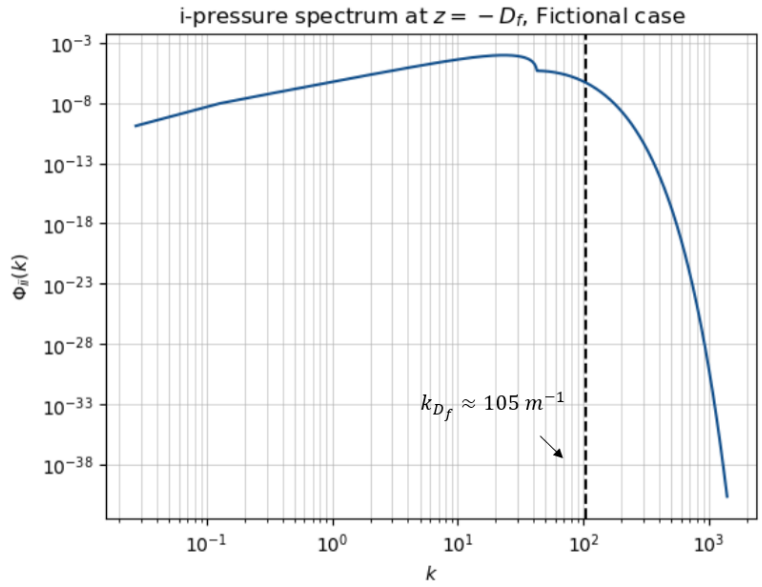

Figure 6.6: The gradient spectrum of the geotextile for the fictional case.

The gradient spectrum in the wave-number domain is then transformed to the spatial domain using a random phase model with random phases uniformly distributed between $0 \leq \underline{\alpha} \leq 2\pi$. Following the sampling theory, appropriate step sizes and length of the domains are chosen:

$$\Delta k = 1 \tag{6.7}$$

$$k_{D_f} = \frac{\pi}{D_f} \tag{6.8}$$

$$\Delta x = \frac{\pi}{k_{D_f}} \tag{6.9}$$

$$L = \frac{2\pi}{\Delta k} \tag{6.10}$$

Note that for wave-number band Δk a band width of 1 is taken, since step sizes smaller than 1, showed no discernible difference in the observed gradient, but resulted in an extensive computational time (see section 4.2.2). Following eq. (3.18), the spatial record of the gradient spectrum at $z = D_f$ can be made, see figure 6.7. The number of points N depicted in the spatial record is 2095.

$$i'(x) = \sum_{n=\Delta k}^{N\Delta k} \sqrt{2 \cdot \Delta k \cdot \Phi_{ii}(k_n, z = -D_f)} \cdot cos(k_n x + \underline{\alpha}_n) \tag{6.11}$$

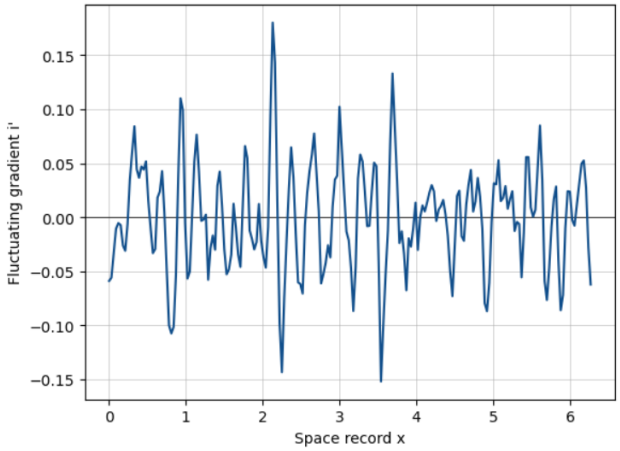

Figure 6.7: The spatial record of the gradient spectrum for the fictional case.

The histogram of the fluctuating gradient values is created to visualize their distribution and identify the bins capturing the top 2 percent of the largest gradients of the total gradient points (N=210). In figure 6.8, the value $i'_{2\%}$ is represented by the green dotted line, which corresponds to the largest absolute value of 0.116 [-].

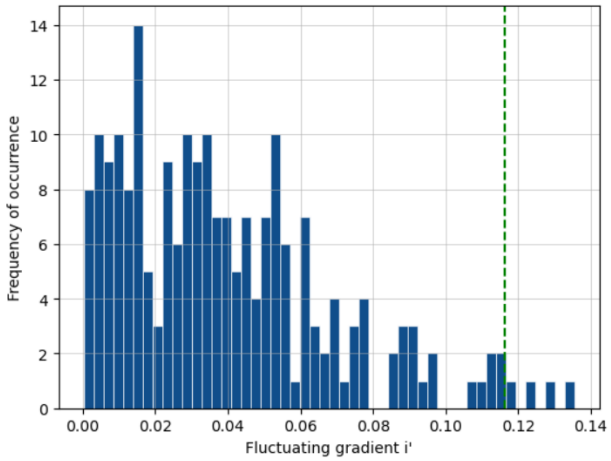

Figure 6.8: The histogram represents the distribution of the fluctuating gradients from the spatial record.

So far, the actual gradient is derived for the gradient of the fluctuating pressures ($i'_{2\%}$). The average gradient is therefore not yet taken into account. To account for the average gradient, eq.(2.26) is used to calculate the average gradient $\bar{i}$ for a uniform flow:

$$\bar{i} = \frac{\tau_b}{\rho_w g h} = \frac{c_f u_0^2}{g h} = 7.65 \cdot 10^{-}5 \quad [-] \tag{6.12}$$

The actual gradient $i_{a,2\%}$ is obtained by combining the average gradient $\bar{i}$ from equation (6.12) and the 2 percent largest gradients of the fluctuating gradient $i'_{2\%}$ from equation (6.11), as shown in eq. (3.19).

$$i_{a,2\%} = \bar{i} + i'_{2\%} = 7.65 \cdot 10^{-5} + 0.116 = 0.116 \quad [-] \tag{6.13}$$

It is worth noting that the impact of the average gradient is considerably smaller compared to the fluctuating gradient. To be more precise, the average gradient is 1517 times smaller than the fluctuating gradient. Therefore, it can be concluded that, in this fictional case, the actual gradients are primarily influenced by the fluctuating gradients alone.

Critical gradient Lemmens

To assess the stability of the filter on top of the geotextile, the design criteria for open filters are applied. According to these criteria, the filter is considered stable when the actual gradient is smaller than the critical gradient, as expressed by the following relation:

$$\frac{i_{a,2\%}}{i_c} < 1 \quad \text{Stable} \tag{6.14}$$

Following the design criteria for open filters, it is necessary to determine the critical gradient for the geotextile. It is important to note the distinction between granular filters and geotextiles in terms of loading and resisting forces. While the velocity through the filter layer serves as the loading force in both cases, the resistance differs due to the filtering action of the geotextile. The Hoffmans method combines both the load and resistance in a single formula for granular open filters (Hoffmans, 2012). However, this is not valid for geotextiles. For granular filters the critical gradient can be determined by using the formula that was suggested by De Graauw (1983); however, no such a formula exists for the critical gradient of open geotextiles. In absence of this theory, we rely on the critical gradients identified by Lemmens (1996), see figure 2.4. For this fictional case, we use the critical gradient of 26% for jute cloth from Lemmens' research. Thus, the stability parameter according to equation (4.8) is calculated as follows:

$$\frac{0.12}{0.26} = 0.46 \quad [-] \tag{6.15}$$

Filter thickness according to the hypothesis

According to eq. (6.15), the initial assumption of a filter thickness of 30 mm leads to a stable filter design. To investigate the effect of varying thickness on filter stability, the results are summarized in table 6.3.

D_f $[mm]$	$i_{a,2\%}$ $[-]$	i_c $[-]$	$i_{a,2\%}/i_c$ $[-]$	Stable/Unstable
200	0.02	0.26	0.08	Stable
100	0.04	0.26	0.15	Stable
50	0.08	0.26	0.31	Stable
30	0.12	0.26	0.46	Stable
20	0.14	0.26	0.54	Stable

Table 6.3: The stability parameter for different filter thicknesses.

The table indicates that even when the filter thickness is 20 mm, the stability parameter indicates a stable filter design. On the other hand, increasing the filter thickness leads to a decrease in the actual gradient value and subsequently a lower stability parameter. Considering the assumptions made in the hypothesis, a safety factor of 1.5 is used on the stability parameter, presenting a stable filter design with a filter thickness of 20-30 mm. Unfortunately, it was not possible to describe a realistic filter thickness that result in an unstable filter design.

7 | Conclusions

In this chapter, the research questions will be addressed first, followed by the main research objective. Given that the research questions have been extensively discussed in the conclusions of each chapter, only a brief description is provided here, followed by a more extensive discussion of the main research objective.

1. How can the actual gradient at the geotextile interface be defined?
A literature study was undertaken in order to investigate the hydrodynamic processes that define the actual gradient at the location where the geotextile is positioned. The framework of linear wave theory proved to be a valuable tool for investigating and modeling these hydrodynamic processes. Based on this literature review, it became apparent that the actual gradient at the bed level can be defined as the sum of an average component and a fluctuating component. To determine the actual gradient, the following hypothesis is proposed:

The actual gradient can be defined by adding the average gradient to a turbulent component derived from measured turbulent wall pressure spectra at the top of the filter layer. Based on the spectral approach and the principles of linear wave theory, it is hypothesized that these turbulent components undergo damping within the filter layer, resulting in a diminished turbulent component at the filter/base interface.

2. Can a method be formulated to calculate this actual gradient under the relevant hydraulic conditions (rough horizontal bed, uniform open channel flow)?
The average gradient in uniform flow can be determined by considering the equilibrium between the bottom shear stress and the fluid pressure component acting on the slope. For the turbulent component acting on a rough bed, extensive research has been conducted on turbulent wall pressures and their unique scaling characteristics. Figure 2.18 presents an overview of the identified scaling characteristics and the various wall conditions and application fields in which the experiments were carried out. It can be inferred that the dimensionless turbulent rough wall pressure spectra developed by Blake (1970) offer the most appropriate representation for this study on geotextiles. In a turbulent wall pressure spectrum, outer scaling variables and inner variables relate to different length scales within the flow, representing large-scale and small-scale fluctuations, respectively. In this hypothesis, it is assumed that the low-frequency region is scaled by the average velocity u_0 and water depth h, while the scaling variables for the high-frequency region are presented in terms of the shear velocity u_* and nominal diameter of the filter material d_{n50}. By combining both spectra, converting the pressure spectrum to the gradient spectrum, and transforming the spectral domain to the spatial record, the fluctuating gradient can be determined.

3. Is it possible to verify this approach with the use of measured data?
To verify this hypothesis, two suitable datasets were identified in the literature. The dataset from Van de Sande (2012) provides an indirect verification of the hypothesis by examining stable or unstable filter conditions. By incorporating Van de Sande's measured dataset into the scaling parameters of the dimensionless pressure spectra and determining the stability parameter for open filters, it was concluded that qualitatively the results align with Van de Sande's findings, indicating stability or instability of the filter layer. However, in some test cases, the hypothesis suggested instability while the experiments indicated stability. This discrepancy may be due to the fact that while the stability parameter may indicate an unstable filter, it does not necessarily correlate with significant base material transport through the filter layer. In a quantitative analysis, the amount of dimensionless transport of base material was compared to the stability parameter. According to the data presented in figure 4.12, it can be observed that the stability parameter exhibits a value that is three times larger then the stability parameter defined by Schiereck (2012), while not inducing any significant transport of base material. This finding aligns with previous experimental investigations, such as the study conducted by Wolters & Van Gent (2012), which similarly demonstrated that the stability parameter could reach values that are two to three times larger, while still not resulting in notable base material transport.

The other dataset identified in the literature was that of Wolters & Van Gent (2012). The verification in this

quantitative analysis verified the hypothesis by comparing the gradients obtained in the hypothesis with the measured gradients from Wolters & Van Gent (2012). The calculated gradients were found to be of similar magnitude, ranging from 0.25 smaller to 1.50 larger than the measured gradients of Wolters & Van Gent (2012).

4. Are there other field of applications for which this approach can be used, and how can this be realized?
The objective of our study was the development of a design method which applies to any context of uniform flow conditions. With a few modifications, the design method could also be extended to wave conditions. By following a similar approach in the hypothesis of the design method for uniform flow, the wave-induced pressures at still water level can be used to calculate the pressure gradients at the filter/base interface. In contrast to the use of a pressure spectrum in the approach for uniform flow, the approach for waves can incorporate a wave spectrum, such as the commonly used JONSWAP spectrum.

Main objective

The main objective of this research was formulated as:

To formulate a design method for geotextiles under a single granular filter layer based on the principles of open filters.

The main research objective in this study was to formulate a design method for geotextiles under a single granular filter layer. Given the novelty of the concept of "open" geotextiles and the limited availability of existing literature or methods related to these filters, it was necessary to take some steps back and first define the actual gradients, as well as identify the most suitable method for estimating these gradients. The verification of the hypothesis yielded results that indicate an approach capable of estimating the actual gradients with a similar magnitude as the measurements from two datasets found in the literature. With a clearer understanding of how to estimate the actual gradients at the location where the geotextile is constructed, the same approach employed in the hypothesis is applied to address the design of a stable open geotextile under a single granular filter layer. This has been demonstrated through a case study, where the thickness of the filter layer was determined to create a stable filter structure.

Discussion

Despite the hypothesis providing an indication of the actual gradient within the same order of magnitude as the two other datasets, there are still certain assumptions that may influence the actual gradient. Regarding the pressure spectrum presented by Blake (1970), one consideration is that the average velocity is equal to the free-stream velocity. However, in open channels, the average velocity is typically lower due to the presence of a rough bed. This difference in velocity should be taken into account. Another point to note is that the spectral curve by Blake was measured for elements with a roughness height of 5 mm. It is expected that the pressure spectrum would be different when larger elements are present in the experiments. Since the filter material used in the measured datasets had larger dimensions, there is some uncertainty about the accuracy of Blake's spectrum for these cases. Additionally, the frequency range measured by Blake is limited by the constraints of his measurements, which were conducted in a wind tunnel. It is unknown if this range captures all the frequencies relevant to open channel flow.

While further research is needed, this hypothesis still offers a fresh perspective on evaluating the stability of open filter structures. If successfully refined, the design method could become a valuable tool in geotextile design and potentially find applications in a broader context involving open structures.

8 Recommendations

This chapter lists practical recommendations for future research based on the findings and conclusions that were presented in chapters 7. Since this study emphasized on understanding the actual gradients within the context of an open channel with uniform flow conditions, the following recommendations are applicable to horizontal beds. Yet, future research may explore bank protections on sloped surfaces and investigate the effect of water/air conditions on natural geotextiles.

1. The surface pressure fluctuations at the bed result from local variations in flow properties such as velocity, vorticity, and turbulence. Accurate measurement of these fluctuations is crucial to characterize the spectral density of wall pressure fluctuations in open channel flow. However, the behavior of the pressure spectrum in the low-frequency region, influenced by the free surface, remains unknown and is expected to differ from wind tunnel measurements conducted in 1970. It would be intriguing to investigate how the spectrum would appear today using more precise measurement techniques under open channel flow conditions. This approach could provide a directly relevant pressure spectrum for open channels. To accomplish this, the initial step would involve measurement of these fluctuations on a rough bed and their inclusion in a spectrum. Subsequently, different scaling characteristics may be employed to achieve the best collapse of the spectrum in the low-frequency region. By developing a pressure spectrum specifically designed for open channel flow, more accurate estimation of the fluctuating gradients can be obtained. This would significantly improve our approach to determine the gradients at the filter/base interface, providing a stronger foundation for further analysis.

2. The test materials used by Lemmens (1996), such as the geotextile jute with 4 cm wood pulp (see figure 2.4), are no longer used in current testing practices. Consequently, in order to determine the critical gradient value for new materials, it is necessary to conduct tests on to them. To assess the strength of modern jute geotextiles, it is recommended to replicate Lemmens' test set-up (1996) but using 'modern' jute materials and up-to-date measurement equipment. While our main focus has been on jute fabric, which was suggested by Lemmens as a promising alternative due to its effective sandtightness, it would also be valuable to examine other materials using the same experimental setup. This approach would generate a new list of critical gradients for various natural 'open' geotextiles, that can be integrated into the design methodology.

   To ensure the stability of open filters, these critical gradients can then be correlated with the actual gradients arising from the loading forces exerted on the geotextile. The pressure spectrum, as explained in the hypothesis of this study, can be utilized to determine the loading forces. Additionally, the pressure gradient at the top of the filter layer can be measured to assess the loading forces. By measuring the pressure gradient at the bottom of the filter layer (at the filter/base interface), it becomes possible to compare the observed reduction with the theoretical approach described in the hypothesis.

3. In this study it is hypothesized that the turbulent component of the pressures measured at the top of the filter layer undergo linear damping within the filter layer. This leads to a diminished turbulent component at the filter/base interface. However, in the case of non-linear damping, the damping behavior will be different. Therefore, additional research is necessary to incorporate the distribution of pressure at the filter/base interface into the design method for non-linear damping in the filter layer.

4. In chapter 5, the discussion arose regarding an alternative to the critical gradient for determination of the critical value of geotextiles, namely the critical filter velocity. The critical gradient, as described by De Graauw (1983), includes the filter diameter, which indirectly affects the velocity in the filter layer. To address this, a suggested alternative measure is the critical filter velocity. In Lemmens' study, the critical filter velocities for both jute and jute with 4 cm woodpulp were calculated using the Forchheimer equations (see eq. (5.3) and (5.4)). These calculated velocities were $u_{f,c,1} = 0.19$ $[m/s]$ and $u_{f,c,2} = 0.28$ $[m/s]$ respectively. One may hypothesize that the critical filter velocity will demonstrate relative consistency

across different stone sizes within the filter layer, whereas the critical gradient is expected to increase with smaller stones. This would result in a critical filter velocity that remains highly consistent among different types of stones on the same geotextile (assuming the flow regime, either turbulent or laminar, remains unchanged).

To verify this hypothesis, an experiment is proposed wherein the same geotextile is subjected to different stone sizes for protection. The velocity will be gradually increased until the filter layer becomes unstable, after which the critical filter velocity can be ascertained. If the critical filter velocity approximately converges to the same value across different stone sizes, it would indicate a higher level of consistency. To determine this effect, the feasibility of using various stone sizes in a flume needs to be assessed. The experimental setup of Lemmens will be utilized, and two stone sizes specified by the NEN-EN 13383 standard will be theoretically placed in the flume. The grading of the two stone types are as follows: stone type A (45-125 mm) with a median particle diameter (d_{50}) of 0.080 m, and stone type B (90-180 mm) with d_{50} of 0.135 m. Under identical flow conditions and utilizing the respective critical gradients for the jute cloth ($i_{c,1} = 0.26$) and jute cloth filled with 4 cm of wood pulp ($i_{c,2} = 0.56$), the critical filter velocity for stone type A (45-125 mm) will be:

$$u_{f,c,1,A} = 0.14 \quad [m/s] \tag{8.1}$$
$$u_{f,c,2,A} = 0.20 \quad [m/s] \tag{8.2}$$

and for stone type B (90-180 mm):

$$u_{f,c,1,B} = 0.18 \quad [m/s] \tag{8.3}$$
$$u_{f,c,2,B} = 0.27 \quad [m/s] \tag{8.4}$$

These theoretical concepts can be verified through experimental testing using a flume setup with various geotextiles. Furthermore, one then may conclude whether the critical gradient varies or not, when using different stones that are applied to the same geotextile. If these tests confirm the hypothesis, it would be possible to modify the design method as has been developed in our study. The modified design method would incorporate the calculation of filter velocity using the Forchheimer equation and also the actual gradients that have been derived from the spectrum analysis. However, it should be noted that Lemmens conducted his experiments using the same sand ($d_{b50} = 145\mu m$). Therefore, further research is necessary to investigate the impact of varying sand diameters on the critical filter velocity. Additionally, the opening size of the geotextile, which has not been tested thus far, could potentially affect the critical filter velocity. Thus, it is important to conduct further investigations in this regard.

5. The hypothesis for the actual gradients for waves can be verified with other datasets. In this study was explained how the approach of the actual gradients under currents can be modified so that this could also be applied for wave conditions. The starting point of this approach would then be a wave spectrum, for example JONSWAP. To perform a quantitative analysis, the actual gradients for the hypothesis can be compared with the measured gradients found for wave conditions in Wolters & Van Gent (2012). Therefore, a similar verification can be done as presented in this study for the currents.

Bibliography

Álvarez-Mozos, J., Abad, E., Giménez, R., Campo, M. A., Goñi, M., Arive, M., Casalí, J., Díez, J., & Diego, I. (2014). Evaluation of erosion control geotextiles on steep slopes. part 1: Effects on runoff and soil loss. *CATENA*, *118*, 168–178. https://doi.org/https://doi.org/10.1016/j.catena.2013.05.018

Bai, X., Li, F., Ma, L., & Li, C. (2022). Weathering of geotextiles under ultraviolet exposure: A neglected source of microfibers from coastal reclamation. *Science of The Total Environment*, *804*, 150168.

Bakker, K., Verheij, H., & De Groot, M. (1994). Design relationship for filters in bed protection. *Journal of Hydraulic engineering*, *120*(9), 1082–1088.

Barba, L. (2013). Computational fluid dynamics.

Bendat, J. S., & Piersol, A. G. (1971). Random data: Analysis and measurement procedures john wiley & sons. *New York*.

Blake, W. K. (1970). Turbulent boundary-layer wall-pressure fluctuations on smooth and rough walls. *Journal of Fluid Mechanics*, *44*(4), 637–660.

Blake, W. K. (2017). *Mechanics of flow-induced sound and vibration, volume 2: Complex flow-structure interactions*. Academic press.

Booij, R. (1998). Erosie onder een geometrisch open filter. *Report 1998-2 (for RWS)*.

Carneiro, J. R., Almeida, P. J., & Lopes, M. d. L. (2019). Evaluation of the resistance of a polypropylene geotextile against ultraviolet radiation. *Microscopy and Microanalysis*, *25*(1), 196–202.

Carroll, R. (1983). *Geotextile filter criteria*. Mirafi Incorporated.

Chang III, P. A., Piomelli, U., & Blake, W. K. (1999). Relationship between wall pressure and velocity-field sources. *Physics of Fluids*, *11*(11), 3434–3448.

CUR. (1993). *Filters in de waterbouw*. https://books.google.nl/books?id=DH0NAQAACAAJ

CUR. (2000). Cur 205: Water-en oeverplanten. *Gouda, 429p*.

CUR. (2012). Cur 233: Interface stability of granular filter structures.

De Graauw, A., de Bye, M. v. d. D., & van der Meulen, T. (1983). *Design criteria for granular filters*. Delft Hydraulics Laboratory.

Detert, M. (2008). *Hydrodynamic processes at the water-sediment interface of streambeds* (Doctoral dissertation). Zugl.: Karlsruhe, Univ., Diss., 2008.

Du Saar, N. (2022). *Alleen circulaire bouwers komen straks nog binnen bij rijksvastgoedbedrijf*.

Farabee, T. M., & Casarella, M. J. (1991). Spectral features of wall pressure fluctuations beneath turbulent boundary layers. *Physics of Fluids A: Fluid Dynamics*, *3*(10), 2410–2420.

Giroud, J.-P. (2010). Development of criteria for geotextile and granular filters. *Proceedings of the 9th international conference on geosynthetics, Guaruja, Brazil*, *2327*, 4564.

Gravante, S., Naguib, A., Wark, C., & Nagib, H. (1998). Characterization of the pressure fluctuations under a fully developed turbulent boundary layer. *AIAA journal*, *36*(10), 1808–1816.

Hasselmann, K., Barnett, T. P., Bouws, E., Carlson, H., Cartwright, D. E., Enke, K., Ewing, J., Gienapp, A., Hasselmann, D., Kruseman, P., et al. (1973). Measurements of wind-wave growth and swell decay during the joint north sea wave project (jonswap). *Ergaenzungsheft zur Deutschen Hydrographischen Zeitschrift, Reihe A*.

Hoan, N. T. (2008). Stone stability under non-uniform flow.

Hoffmans, G. J. (2012). *The influence of turbulence on soil erosion* (Vol. 10). Eburon Uitgeverij BV.

Hofland, B. (2005). Rock and roll: Turbulence-induced damage to granular bed protections.

Holthuijsen, L. H. (2007). *Waves in oceanic and coastal waters*. Cambridge university press.

Izbash, S. (1931). O filtracii v kropnozernstom materiale. *Leningrad, USSR*, (in Russian).

Jiao, W., Chen, H., Cheng, L., Zhang, B., Yang, Y., & Luo, C. (2022). Experimental study on flow evolution and pressure fluctuation characteristics of the underwater suction vortex of water jet propulsion pump unit in shallow water. *Ocean Engineering*, *266*, 112569.

Joseph, L. A., Molinaro, N. J., Devenport, W. J., & Meyers, T. W. (2020). Characteristics of the pressure fluctuations generated in turbulent boundary layers over rough surfaces. *Journal of Fluid Mechanics*, *883*, A3.

Kalore, S. A., & Babu, G. S. (2022). Improved design criteria for nonwoven geotextile filters with internally stable and unstable soils. *Geotextiles and Geomembranes*, *50*(6), 1120–1134.

Khan, M., Dawson, A., & Marshall, A. (2022). Filtration performance of non-woven geotextiles with internally-stable and-unstable soils under dynamic loading. *Geotextiles and Geomembranes*, *50*(2), 293–311.

Klar, M. (2005). *Design of an endoscopic 3-d particle-tracking velocimetry system and its application in flow measurements within a gravel layer* (Doctoral dissertation).

Lama, T. D., Burman, D., Mandal, U. K., Sarangi, S. K., & Sen, H. S. (2021). *Transforming coastal zone for sustainable food and income security* (T. Lama, D. Burman, U. K. Mandal, S. K. Sarangi, & H. Sen, Eds.). Springer International Publishing. https://doi.org/10.1007/978-3-030-95618-9

Lee, I., & Sung, H. J. (2002). Multiple-arrayed pressure measurement for investigation of the unsteady flow structure of a reattaching shear layer. *Journal of Fluid Mechanics*, *463*, 377–402.

Lee, Y.-T., Blake, W., & Farabee, T. (2005). Prediction of wall pressure spectrum using a rans calculation. *43rd AIAA Aerospace Sciences Meeting and Exhibit*, 802.

Lemmens, R. (1996). Natuurvriendelijke verbetering van de zanddichtheid van klassieke zink-en kraagstukken.

Meyers, T., Forest, J. B., & Devenport, W. J. (2015). The wall-pressure spectrum of high-reynolds-number turbulent boundary-layer flows over rough surfaces. *Journal of Fluid Mechanics*, *768*, 261–293.

Moraci, N., Mandaglio, M. C., & Ielo, D. (2012). A new theoretical method to evaluate the internal stability of granular soils. *Canadian Geotechnical Journal*, *49*(1), 45–58.

PIANC-MarCom. (2011). *The application of geosynthetics in waterfront areas*. PIANC report 113 Secrétariat Général. https://books.google.nl/books?id=aq7Z6H4jplAC

Prambauer, M., Wendeler, C., Weitzenböck, J., & Burgstaller, C. (2019). Biodegradable geotextiles–an overview of existing and potential materials. *Geotextiles and Geomembranes*, *47*(1), 48–59.

Schiereck, G. J. (2012). *Introduction to bed, bank and shore protection*. CRC Press.

Shields, A. (1936). Anwendung der aehnlichkeitsmechanik und der turbulenzforschung auf die geschiebebewegung. *PhD Thesis Technical University Berlin*.

Van de Sande, S. (2012). Stability of open filter structures.

Van Gent, M. R. A. (1992). Formulae to describe porous flow. *Communications on hydraulic and geotechnical engineering, No. 1992-02*.

Varano, N. D. (2010). *Fluid dynamics and surface pressure fluctuations of turbulent boundary layers over sparse roughness* (Doctoral dissertation). Virginia Tech.

Veldman, A. (2013). Computational fluid dynamics.

Vermeer, G. J. (2012). *3d seismic survey design*. Society of Exploration Geophysicists.

Weggel, J. R., & Ward, N. D. (2012). A model for filter cake formation on geotextiles: Theory. *Geotextiles and Geomembranes*, *31*, 51–61.

Wolters, G., & Van Gent, M. R. (2012). Granular open filters on a horizontal bed under wave and current loading. *Proc. Coastal Eng*, *1*(33), 10–9753.

Wörman, A. (1989). Riprap protection without filter layers. *Journal of Hydraulic engineering*, *115*(12), 1615–1630.

List of Figures

List of Tables

A | Appendix A - Verification of hypothesis for Van de Sande (2012)

All test cases are run for N=1 and given step sizes as in chapter 4.

A.1 Test T01

T01	Mean velocity u_0 $[m/s]$	Water depth h $[cm]$	Shear velocity u_* $[m/s]$	Stone size d_{fn50} $[mm]$
Case 1.	0.30	6.7	0.0326	7.54
Case 2.	0.40	23.4	0.0360	7.54
Case 3.	0.55	23.8	0.0494	7.54
Case 4.	0.60	26.5	0.0533	7.54
Case 5.	1.00	17.1	0.0933	7.54

Table A.1: Scaling parameters for pressure spectrum obtained from dataset Van de Sande (2012): T01

T01	$i_{2\%}$ $[-]$	$\bar{i}$ $[-]$	i_a $[-]$	i_c $[-]$	i_a/i_c $[-]$
Case 1.	0.015	0.0016	0.017	0.055	0.30
Case 2.	0.024	0.0006	0.025	0.055	0.46
Case 3.	0.046	0.0011	0.047	0.055	0.86
Case 4.	0.054	0.0011	0.059	0.055	0.98
Case 5.	0.156	0.0052	0.161	0.055	2.92

Table A.2: 2 percent exceedance gradient, 'mean' gradient, actual gradient, critical gradient and stability parameter for T01

T01	Mean velocity u_0 $[m/s]$	Van de Sande (2012)	Hypothesis
Case 1.	0.30	Stable	Stable
Case 2.	0.40	Stable	Stable
Case 3.	0.55	Stable	Stable
Case 4.	0.60	Stable	Stable
Case 5.	1.00	Unstable	Unstable

Table A.3: Stable or unstable filter based on Van de Sande (2012) & the hypothesis.

A.2 Test T02b

T02b	Mean velocity u_0 $[m/s]$	Water depth h $[cm]$	Shear velocity u_* $[m/s]$	Stone size d_{fn50} $[mm]$
Case 1.	0.25	28.4	0.0289	22.01
Case 2.	0.30	26.5	0.0350	22.01
Case 3.	0.58	24.5	0.068	22.01
Case 4.	0.60	29.4	0.069	22.01

Table A.4: Scaling parameters for pressure spectrum obtained from dataset Van de Sande (2012): T02b

T02b	$i_{2\%}$ $[-]$	$\bar{i}$ $[-]$	i_a $[-]$	i_c $[-]$	i_a/i_c $[-]$
Case 1.	0.011	0.0003	0.011	0.017	0.69
Case 2.	0.014	0.0005	0.015	0.017	0.91
Case 3.	0.062	0.0019	0.064	0.017	3.84
Case 4.	0.060	0.0017	0.062	0.017	3.71

Table A.5: 2 percent exceedance gradient, 'mean' gradient, actual gradient, critical gradient and stability parameter for T02b

T01	Mean velocity u_0 $[m/s]$	Van de Sande (2012)	Hypothesis
Case 1.	0.25	Stable	Stable
Case 2.	0.30	Stable	Stable
Case 3.	0.58	Unstable	Unstable
Case 4.	0.60	Unstable	Unstable

Table A.6: Stable or unstable filter based on Van de Sande (2012) & the hypothesis.

A.3 Test T03

T03	Mean velocity u_0 $[m/s]$	Water depth h $[cm]$	Shear velocity u_* $[m/s]$	Stone size d_{fn50} $[mm]$
Case 1.	0.30	15.7	0.0378	22.01
Case 2.	0.35	18.4	0.0430	22.01
Case 3.	0.48	26.7	0.0560	22.01
Case 4.	0.60	20.4	0.0725	22.01
Case 5.	0.80	18.3	0.0983	22.01
Case 6.	0.82	18.1	0.1010	22.01
Case 7.	0.90	19.9	0.1092	22.01

Table A.7: Scaling parameters for pressure spectrum obtained from dataset Van de Sande (2012): T03

T03	$i_{2\%}$ $[-]$	$\bar{i}$ $[-]$	i_a $[-]$	i_c $[-]$	i_a/i_c $[-]$
Case 1.	0.007	0.0009	0.008	0.034	0.23
Case 2.	0.008	0.0010	0.009	0.034	0.27
Case 3.	0.016	0.0012	0.017	0.034	0.50
Case 4.	0.024	0.0026	0.026	0.034	0.77
Case 5.	0.043	0.0054	0.048	0.034	1.40
Case 6.	0.041	0.0057	0.047	0.034	1.36
Case 7.	0.051	0.0061	0.057	0.034	1.66

Table A.8: 2 percent exceedance gradient, 'mean' gradient, actual gradient, critical gradient and stability parameter for T03

T01	Mean velocity u_0 $[m/s]$	Van de Sande (2012)	Hypothesis
Case 1.	0.30	Stable	Stable
Case 2.	0.35	Stable	Stable
Case 3.	0.48	Stable	Stable
Case 4.	0.60	Stable	Stable
Case 5.	0.80	Unstable	Unstable
Case 6.	0.82	Unstable	Unstable
Case 7.	0.90	Unstable	Unstable

Table A.9: Stable or unstable filter based on Van de Sande (2012) & the hypothesis.

A.4 Test T04

T04	Mean velocity u_0 $[m/s]$	Water depth h $[cm]$	Shear velocity u_* $[m/s]$	Stone size d_{fn50} $[mm]$
Case 1.	0.25	21.9	0.0299	22.01
Case 2.	0.26	26.1	0.0304	22.01
Case 3.	0.50	21.9	0.0598	22.01
Case 4.	0.52	25.9	0.0608	22.01
Case 5.	0.60	24.4	0.0707	22.01
Case 6.	0.85	17.9	0.1048	22.01

Table A.10: Scaling parameters for pressure spectrum obtained from dataset Van de Sande (2012): T04

T04	$i_{2\%}$ $[-]$	$\bar{i}$ $[-]$	i_a $[-]$	i_c $[-]$	i_a/i_c $[-]$
Case 1.	0.012	0.0004	0.013	0.066	0.20
Case 2.	0.012	0.0004	0.013	0.066	0.20
Case 3.	0.045	0.0017	0.046	0.066	0.70
Case 4.	0.044	0.0015	0.046	0.066	0.68
Case 5.	0.065	0.0021	0.067	0.066	1.01
Case 6.	0.126	0.0063	0.133	0.066	2.00

Table A.11: 2 percent exceedance gradient, 'mean' gradient, actual gradient, critical gradient and stability parameter for T04

T01	Mean velocity u_0 $[m/s]$	Van de Sande (2012)	Hypothesis
Case 1.	0.25	Stable	Stable
Case 2.	0.26	Stable	Stable
Case 3.	0.50	Stable	Stable
Case 4.	0.52	Stable	Stable
Case 5.	0.60	Stable	Unstable
Case 6.	0.85	Unstable	Unstable

Table A.12: Stable or unstable filter based on Van de Sande (2012) & the hypothesis.

A.5 Test T06a

T06a	Mean velocity u_0 $[m/s]$	Water depth h $[cm]$	Shear velocity u_* $[m/s]$	Stone size d_{fn50} $[mm]$
Case 1.	0.25	17.8	0.0280	15.72
Case 2.	0.30	19.6	0.0331	15.72
Case 3.	0.35	21.3	0.0382	15.72
Case 4.	0.50	18.6	0.0556	15.72
Case 5.	0.52	21.7	0.0566	15.72
Case 6.	0.60	18.4	0.0668	15.72
Case 7.	0.85	19.6	0.0938	15.72

Table A.13: Scaling parameters for pressure spectrum obtained from dataset Van de Sande (2012): T06a

T06a	$i_{2\%}$ $[-]$	$\bar{i}$ $[-]$	i_a $[-]$	i_c $[-]$	i_a/i_c $[-]$
Case 1.	0.006	0.0005	0.007	0.037	0.19
Case 2.	0.008	0.0006	0.009	0.037	0.24
Case 3.	0.011	0.0007	0.012	0.037	0.32
Case 4.	0.025	0.0017	0.027	0.037	0.73
Case 5.	0.024	0.0015	0.026	0.037	0.71
Case 6.	0.031	0.0025	0.033	0.037	0.91
Case 7.	0.072	0.0046	0.076	0.037	2.08

Table A.14: 2 percent exceedance gradient, 'mean' gradient, actual gradient, critical gradient and stability parameter for T06a

T01	Mean velocity u_0 $[m/s]$	Van de Sande (2012)	Hypothesis
Case 1.	0.25	Stable	Stable
Case 2.	0.30	Stable	Stable
Case 3.	0.35	Stable	Stable
Case 4.	0.50	Stable	Stable
Case 5.	0.52	Stable	Stable
Case 6.	0.60	Stable	Stable
Case 7.	0.85	Unstable	Unstable

Table A.15: Stable or unstable filter based on Van de Sande (2012) & the hypothesis.

A.6 Test T07

T07	Mean velocity u_0 $[m/s]$	Water depth h $[cm]$	Shear velocity u_* $[m/s]$	Stone size d_{fn50} $[mm]$
Case 1.	0.30	24.5	0.0322	15.72
Case 2.	0.60	19.3	0.0663	15.72
Case 3.	0.75	18.1	0.0837	15.72
Case 4.	0.80	18.7	0.0889	15.72
Case 5.	0.90	21.0	0.0984	15.72

Table A.16: Scaling parameters for pressure spectrum obtained from dataset Van de Sande (2012): T07

T07	$i_{2\%}$ $[-]$	$\bar{i}$ $[-]$	i_a $[-]$	i_c $[-]$	i_a/i_c $[-]$
Case 1.	0.006	0.0004	0.006	0.037	0.17
Case 2.	0.020	0.0023	0.023	0.037	0.63
Case 3.	0.032	0.0039	0.036	0.037	0.98
Case 4.	0.037	0.0043	0.041	0.037	1.13
Case 5.	0.044	0.0047	0.048	0.037	1.32

Table A.17: 2 percent exceedance gradient, 'mean' gradient, actual gradient, critical gradient and stability parameter for T07

T01	Mean velocity u_0 $[m/s]$	Van de Sande (2012)	Hypothesis
Case 1.	0.30	Stable	Stable
Case 2.	0.60	Stable	Stable
Case 3.	0.75	Stable	Stable
Case 4.	0.80	Stable	Unstable
Case 5.	0.90	Unstable	Unstable

Table A.18: Stable or unstable filter based on Van de Sande (2012) & the hypothesis.

B | Appendix B- Python code

In this python code each individual test case can be implemented based on the values given in the tables of appendix A and B.

B.1 Van de Sande (2012)

```
import numpy as np
import matplotlib.pyplot as plt
import math
import numpy.random as npr
from numpy import diff
from scipy.interpolate import interp1d
from scipy.optimize import curve_fit
from scipy.integrate import simpson
```

```
#Constant conditions
width        = 0.4
g            = 9.81
p_w          = 999
```

Pick a test

```
def test(test_name):
    if test_name == "T01":
        p_s    = 2633
        dfn50  = 7.54*10**-3
        df15   = 7.42*10**-3
        Df     = 20*10**-3
        db50   = 309*10**-6
        delta  = (p_s-p_w) / p_w
        shields= 0.02
        n_f = 0.43
        return p_s, dfn50, df15, Df, db50, delta, shields, n_f
    elif test_name == "T02b":
        p_s    = 2633
        dfn50  = 22.01*10**-3
        df15   = 22.45*10**-3
        Df     = 27*10**-3
        db50   = 309*10**-6
        delta  = (p_s-p_w) / p_w
        shields= 0.02
        n_f    = 0.43
        return p_s, dfn50, df15, Df, db50, delta, shields, n_f
```

```
    elif test_name == "T03":
        p_s    = 2633
        dfn50  = 22.01*10**-3
        df15   = 22.45*10**-3
        Df     = 61.5*10**-3
        db50   = 309*10**-6
        delta  = (p_s-p_w) / p_w
        shields= 0.02
        n_f    = 0.31
        return p_s, dfn50, df15, Df, db50, delta,shields, n_f

    elif test_name == "T04":
        p_s    = 2633
        dfn50  = 22.01*10**-3
        df15   = 22.45*10**-3
        Df     = 27*10**-3
        db50   = 633*10**-6
        delta  = (p_s-p_w) / p_w
        shields= 0.02
        n_f    = 0.31
        return p_s, dfn50, df15, Df, db50, delta, shields, n_f
    elif test_name == "T06a":
        p_s    = 2960
        dfn50  = 15.72*10**-3
        df15   = 15.93*10**-3
        Df     = 40*10**-3
        db50   = 309*10**-6
        delta  = (p_s-p_w) / p_w
        shields= 0.02
        n_f    = 0.38
        return p_s, dfn50, df15, Df, db50, delta, shields, n_f
```

```
    elif test_name == "T07":
        p_s    = 2960
        dfn50  = 15.72*10**-3
        df15   = 15.93*10**-3
        Df     = 57*10**-3
        db50   = 309*10**-6
        delta  = (p_s-p_w) / p_w
        shields= 0.02
        n_f    = 0.38
        return p_s, dfn50, df15, Df, db50, delta, shields, n_f
    else:
        return "Invalid test name."

test_name = input("Choose which test you want to see: ")
test = test(test_name)

if isinstance(test, str):
    print(test)
else:
    p_s, dfn50, df15, Df, db50, delta, shields, n_f = test
    print("p_s =", p_s)
    print("dfn50 =", dfn50)
    print("df15 =", df15)
    print("Df =", Df)
    print("db50 =", db50)
    print("delta =", delta)
    print("shields =", shields)
    print("n_f =", n_f)
```

Fill in scaling parameters: u_0, h, u_*, d_{fn50} according to appendix A

```
u_mean = input("Choose the velocity of the test in m/s:\n")
u_mean = float(u_mean)
h      = input("Choose the height of the test in m:\n")
h      = float(h)

R   = (width*h) / (width + 2*h)
kr  = 2*dfn50
C   = 18 * np.log10((12*R)/kr)
c_f = g / C**2

def u_shear(width, h, kr, u_mean, g, C, c_f):
    #u_shear_chezy   = u_mean* np.sqrt(c_f)
    u_shear_chezy   = (u_mean * np.sqrt(g)) / C
    return u_shear_chezy
u_shear = u_shear(width, h, kr, u_mean, g, C, c_f)

print(u_mean, "= mean velocity u0")
print(h, "= water depth h")
print(u_shear, "= shear velocity u*")
print(dfn50, "= stone diameter dfn50")
print(c_f, "= dimenionsless friction coefficient cf")
```

1. Reproduce the dimensionless pressure spectrum of Blake, 1970

```
# Use various points from spectrum Blake
x_out = np.array([0.06, 0.08, 0.1, 0.2, 0.3, 0.4, 0.5, 0.6, 0.8, 1, 2, 4, 6, 8, 10, 20])
y_out = np.array([10**-4, 10**-1, 10**-0, 10**-1, 10**2, 10**5, 10**4, 10**3, 10**2, 10**0, 10**-3, 10**-7, 10**-10, 10**-14, 10**-18, 10**-25])
y_out = 10**(np.log10(y_out)/10)
boundary_left_out  = 0.06
boundary_right_out = 20

# Fill in dimensions in log-format
logx_out = np.log(x_out)
logy_out = np.log(y_out)
poly_out = np.poly1d(np.polyfit(logx_out,logy_out, deg=6))
yfit_out = lambda x: np.exp(poly_out(np.log(x_out)))

# Plot in log-log
plt.loglog(x_out, yfit_out(x_out),'#FFD700')
plt.title('Dimensionless rough wall pressure spectrum, Blake (1970)')
plt.xlabel(r'$\frac{\omega h}{u_0}$')
plt.ylabel(r'$\frac{\Phi(\omega)}{ u_0^3 \rho_w^2 c_f^2 h} $')
#plt.legend(['(1) Scaled on outer variables: $u_0$ and $h$ '], loc='center left', bbox_to_anchor=(1,0.5),prop={'size': 8})
plt.grid(True, which="both", ls="-", linewidth=0.4)
plt.show()
```

```
x_in  = np.array([0.4, 0.6, 0.8, 1, 2,3, 4, 6, 8, 10, 15, 20, 30, 40, 50, 60, 80, 100])
y_in  = np.array([10**-6, 10**-4, 10**-3,10**-3, 10**-2, 10**-1, 10**-0.5, 10**-2.5, 10**-4, 10**-5, 10**-7, 10**-10, 10**-14 ,10**-18, 10**-21, 10**-26, 10**-29, 10**-34 ])
y_in = 10**(np.log10(y_in)/10)
boundary_left_in  = 0.4
boundary_right_in = 100

logx_in  = np.log(x_in)
logy_in  = np.log(y_in)
poly_in  = np.poly1d(np.polyfit(logx_in ,logy_in , deg=6))
yfit_in  = lambda x: np.exp(poly_in (np.log(x_in )))
plt.loglog(x_in,  yfit_in (x_in ),'#104E8B')
plt.title('Dimensionless rough wall pressure spectrum , Blake (1970)')
plt.xlabel(r'$\frac{\omega  dfn50}{u_*}$')
plt.ylabel(r'$\frac{\Phi(\omega)}{u_*^3 \rho_w^2 dfn50}$')
#plt.legend(['Scaled on inner variables: $u_{*}$ and $dfn50$'], loc='center left', bbox_to_anchor=(1,0.5),prop={'size': 8})
plt.grid(True, which="both", ls="-", linewidth=0.4)
plt.show()
```

2. Make the spectrum dimensional into: ω-spectrum at $z = 0$

```
# Define axis of the outer variables u_mean and h
def w_start_out(boundary_left_out, u_mean, h):
    w_start = (boundary_left_out * u_mean) / h
    return w_start
w_start_out = w_start_out(boundary_left_out, u_mean, h)

def w_end_out(boundary_right_out, u_mean, h):
    w_end = (boundary_right_out * u_mean) / h
    return w_end
w_end_out = w_end_out(boundary_right_out, u_mean, h)
w_step_out = 0.001
w_list_out = np.arange(w_start_out, w_end_out, w_step_out)

def horizontal_value_out(w, h, u_mean):
    horizontal= (w * h) / u_mean
    return horizontal
vert_val_out = np.interp(horizontal_value_out(w_list_out,h, u_mean), x_out,y_out)

def Gpp_out(v,u_mean,p_w,c_f,h):
    variance = (v * u_mean**3 * p_w**2 * c_f**2 * h)
    return variance

Gpp_list_out = np.zeros(len(vert_val_out))
for i in range(len(vert_val_out)):
    Gpp_list_out[i] = Gpp_out(vert_val_out[i], u_mean,p_w,c_f, h)
```

```
# Define axis of the inner variables u_shear and dfn50
def w_start_in(boundary_left_in, u_shear,dfn50):
    w_start = (boundary_left_in * u_shear) /  dfn50
    return w_start
w_start_in = w_start_in(boundary_left_in, u_shear,dfn50)

def w_end_in(boundary_right_in, u_shear,dfn50):
    w_end = (boundary_right_in * u_shear) / dfn50
    return w_end
w_end_in = w_end_in(boundary_right_in, u_shear ,dfn50)
w_step_in = 0.1
w_list_in = np.arange(w_start_in, w_end_in, w_step_in)

def horizontal_value_in(w, dfn50, u_shear):
    horizontal= (w * dfn50) / u_shear
    return horizontal
vert_val_in = np.interp(horizontal_value_in(w_list_in, dfn50, u_shear), x_in,y_in)

def Gpp_in(v, u_shear, p_w, dfn50):
    variance = v * u_shear**3 * p_w**2 *dfn50
    return variance

Gpp_list_in = np.zeros(len(vert_val_in))
for i in range(len(vert_val_in)):
    Gpp_list_in[i] = Gpp_in(vert_val_in[i], u_shear,p_w,dfn50)
```

```
# Plot the line for the outer variables
logw_list_out = np.log(w_list_out)
logGpp_list_out = np.log(Gpp_list_out)
poly_dim_out = np.poly1d(np.polyfit(logw_list_out,logGpp_list_out, deg=2))
yfit_dim_out = lambda x: np.exp(poly_dim_out(np.log(w_list_out)))
plt.loglog(w_list_out, yfit_dim_out(w_list_out),'#FFD700')

# Plot the line of the inner variables
logw_list_in = np.log(w_list_in)
logGpp_list_in = np.log(Gpp_list_in)
poly_dim_in = np.poly1d(np.polyfit(logw_list_in,logGpp_list_in, deg=2))
yfit_dim_in = lambda x: np.exp(poly_dim_in(np.log(w_list_in)))
plt.loglog(w_list_in, yfit_dim_in(w_list_in),'#104E8B')


# Plot characteristics
plt.title('$\omega$-pressure spectrum at z=0, T01: case 1')
plt.xlabel(r'$\omega$')
plt.ylabel(r'$\Phi_{pp}(\omega)$')
plt.legend(['Scaled on outer variables: $u_0$ and $h$ ','Scaled on inner variables: $u_{*}$ and $dfn50$'], loc='center left', bbox_to_anchor=(1,0.5),prop={'size': 8})
plt.grid(True, which="both", ls="-", linewidth=0.4)
plt.show()
```

3.Connect the two peaks with a line

```
# Find the maximum values and corresponding indices
max_value_out = np.max(yfit_dim_out(w_list_out))
max_index_out = np.argmax(yfit_dim_out(w_list_out))
max_w_out = w_list_out[max_index_out]

max_value_in = np.max(yfit_dim_in(w_list_in))
max_index_in = np.argmax(yfit_dim_in(w_list_in))
max_w_in = w_list_in[max_index_in]

# Remove values to the right of the maximum in the first curve
new_w_list_out = w_list_out[:max_index_out+1]
new_yfit_dim_out = yfit_dim_out(w_list_out)[:max_index_out+1]

# Remove values to the left of the maximum in the second curve
new_w_list_in = w_list_in[max_index_in:]
new_yfit_dim_in = yfit_dim_in(w_list_in)[max_index_in:]

# Plot the modified curves
plt.loglog(new_w_list_out, new_yfit_dim_out, '#FFD700')
plt.loglog(new_w_list_in, new_yfit_dim_in, '#104E8B')

# Connect the two points with a line
plt.plot([max_w_out, max_w_in], [max_value_out, max_value_in], 'k--', label='Line between Peaks')

# Plot original lines to illustrate curve
plt.loglog(w_list_out, yfit_dim_out(w_list_out), '#FFD700', linewidth = 0.6, linestyle = '-.' )
plt.loglog(w_list_in, yfit_dim_in(w_list_in), '#104E8B',  linewidth = 0.6, linestyle = '-.')

# Plot characteristics
plt.title(r'$\omega$-pressure spectrum at z=0, T01: case 1')
plt.xlabel(r'$\omega$')
plt.ylabel(r'$\Phi_{pp}(\omega)$')
plt.legend(['Scaled on outer variables: $u_0$ and $h$ ','Scaled on inner variables: $u_{*}$ and $dfn50$'], loc='center left', bbox_to_anchor=(1,0.5),prop={'size': 8})
plt.grid(True, which="both", ls="-", linewidth=0.4)
#plt.xlim(10**0, 5*10**1)
#plt.ylim(10**-1, 5*10**-1)

plt.show()
```

4.Combine both curves in one spectrum (based on dotted line)

```
one_spectrum_x = np.concatenate((new_w_list_out, new_w_list_in))
one_spectrum_y = np.concatenate((new_yfit_dim_out, new_yfit_dim_in))
plt.loglog(one_spectrum_x, one_spectrum_y, '#104E8B')

# Plot characteristics
plt.title(r'$\omega$-pressure spectrum at z=0, T01: case 1')
plt.xlabel(r'$\omega$')
plt.ylabel(r'$\Phi_{pp}(\omega)$')
#plt.legend(['Scaled on outer variables: $u_0$ and $h$ ','Scaled on inner variables: $u_{*}$ and $dfn50$'], loc='center left', bbox_to_anchor=(1,0.5),prop={'size': 8})
plt.grid(True, which="both", ls="-", linewidth=0.4)
plt.show()
```

5.Transformation from frequency spectrum to wave-number spectrum

```
#Blake suggested a convection velocity of 0.44 times the mean velocity for rough walls
u_convection = 0.44*u_mean
one_spectrum_x_k = one_spectrum_x / u_convection
one_spectrum_y_k = one_spectrum_y * u_convection
plt.loglog(one_spectrum_x_k, one_spectrum_y_k, '#104E8B')

plt.title('k-pressure spectrum at z=0, T01: case 1')
plt.xlabel(r'$k$')
plt.ylabel(r'$\Phi_{pp}(k)$')
plt.xlim(10**-1,10**5)
#plt.legend(['Scaled on outer variables: $u_0$ and $h$ ','Scaled on inner variables: $u_{*}$ and $dfn50}$'], loc='center left', bbox_to_anchor=(1,0.5),prop={'size': 8})
plt.grid(True, which="both", ls="-", linewidth=0.4)
plt.show()
```

6. Describe the gradient spectrum at $z = -Df$ by linear damping

```
#Step size in wave-number domain and spatial domain
delta_k   = 1
k_s       = one_spectrum_x_k[-1]
delta_x   = np.pi / k_s
length_wave_record = (2*np.pi) / delta_k
k_range = np.arange(one_spectrum_x_k[0], one_spectrum_x_k[-1], delta_k)
G_k = np.interp(k_range, one_spectrum_x_k, one_spectrum_y_k)

# Define gradient function
def Gii(G, k, p_w, g):
    gradient = G*(k / (p_w*g))**2
    return gradient

G_ii = np.zeros(len(G_k))
for i in range(len(G_k)):
    G_ii[i] = Gii(G_k[i], k_range[i], p_w, g)

G_ii_Df = np.zeros(len(G_k))
for i in range(len(G_k)):
    G_ii_Df[i] = Gii(G_k[i],k_range[i], p_w, g) / (np.cosh(k_range[i]*Df))**2


# Limit the gradient spectrum with a physical boundary > filterthickness Df
delta_k     = 1
k_damping   = np.pi / Df
k_s_damping = k_damping
delta_x_damping = np.pi / k_s_damping
k_range_damping = np.arange(one_spectrum_x_k[0], k_damping, delta_k)
G_k_damping = np.interp(k_range_damping, one_spectrum_x_k,one_spectrum_y_k)

# Find new points of gradient spectrum
G_ii_damping = np.zeros(len(G_k_damping))
for i in range(len(G_k_damping)):
    G_ii_damping[i] = Gii(G_k_damping[i], k_range_damping[i], p_w, g) / (np.cosh(k_range_damping[i]*Df))**2
```

```
# Limit the gradient spectrum with a physical boundary > filterthickness Df
delta_k     = 1
k_damping   = np.pi / Df
k_s_damping = k_damping
delta_x_damping = np.pi / k_s_damping
k_range_damping = np.arange(one_spectrum_x_k[0], k_damping, delta_k)
G_k_damping = np.interp(k_range_damping, one_spectrum_x_k,one_spectrum_y_k)

# Find new points of gradient spectrum
G_ii_damping = np.zeros(len(G_k_damping))
for i in range(len(G_k_damping)):
    G_ii_damping[i] = Gii(G_k_damping[i], k_range_damping[i], p_w, g) / (np.cosh(k_range_damping[i]*Df))**2


# Plot gradient spectrum at z = -Df
plt.axvline(k_damping, linestyle ='--', color='k')
plt.loglog(k_range,G_ii_Df, color='#104E8B')
plt.title('i-pressure spectrum at $z=D_f$, T01: case 1')
plt.xlabel(r'$k$')
plt.ylabel(r'$\Phi_{ii}(k)$')
plt.grid(True, which="both", ls="-", linewidth=0.4)
plt.show()
```

7. Convert to the spatial domain by assuming random phase

```
# Number of times the record is repeated
N_times            = 1

#Define function for gradient at z=-Df
def gradient_record(delta_k, G, k, x, phase):
    amplitude_gradient = np.sqrt(2*delta_k* G)
    pressure_gradient  = amplitude_gradient * np.cos(k*x + phase)
    return pressure_gradient

# Generate gradient record
spatial_domain = np.arange(0, N_times*length_wave_record, delta_x_damping)
random_phase = np.zeros(len(G_k_damping))
result = []
for i in range(len(G_k_damping)):
    random_phase[i] = npr.uniform(0, 2*np.pi)
    for j in range(len(spatial_domain)):
        each_gradient = gradient_record(delta_k, G_ii_damping[i], k_range_damping[i], spatial_domain[j], random_phase[i])
        result.append(each_gradient)

# Sum gradient of all amplitudes over spatial domain x
sum_gradient = np.zeros(len(spatial_domain))
for i in range(len(result)):
    q = i
    if i == len(spatial_domain):
        break
    sum_gradient[i] = sum(result[q::len(spatial_domain)])


# Plot the gradient record
plt.axhline(0,color='black',linewidth=0.6)
plt.title("Pressure gradient at $z=-D_f$")
plt.xlabel("Space record x")
plt.ylabel("Fluctuating gradient i'")
plt.plot(spatial_domain,sum_gradient, color='#104E8B')
plt.grid(True, which="both", ls="-", linewidth=0.4)
plt.show()
```

8. Make histogram of spatial record

```
new_sum_gradient = [abs(value) if value < 0 else value for value in sum_gradient]
i_2percent = np.percentile(new_sum_gradient, 98)

print('2 percent exceedance value of the absolute fluctuating gradient:', i_2percent)

# Add vertical lines for percentiles
plt.axvline(i_2percent, color='g', linestyle='--')
plt.grid(True, which="both", ls="-", linewidth=0.4)
plt.hist(new_sum_gradient, bins=50, edgecolor='w',linewidth=0.5,color='#104E8B')
plt.xlabel("Fluctuating gradient i'")
plt.ylabel("Frequency of occurrence")
plt.show()
```

9. Earlier, the fluctuating gradient is calculated. To describe the $i_{2\%}$ then the mean gradient the bed shear stress must be included

```
def i_mean(u_shear, rho, g, h):
    tau = rho * u_shear**2
    i = tau / (rho*g*h)
    return i
i_mean = i_mean(u_shear,p_w,g,h)
print('The mean gradient due to the pressure i_mean',i_mean)
print('The gradient caused by the fluctuating pressures i_2percent',i_2percent)
i_total = i_mean + i_2percent
print('The total gradient is then i_a:',i_total)
```

10. Define the critical gradient i_c

In order to establish a relation for the critical gradient in porous flow, the Forchheimer equation with the threshold of movement as given by Shields are linked together. and resulted in an emperical relation:

$$i_C = [\frac{0.06}{n_F^3 d_{15F}^{4/3}} + \frac{n_F^{5/3} d_{15F}^{1/3}}{1000 d_{50B}^{5/3}}] \quad u_{*c}^2$$

```
def critical_gradient(n_f ,df15, db50, delta, shields):
    u_shear_c = np.sqrt(g*delta*db50*shields)
    u_shear_old = 1.3* db50**0.57 + 8.3*10**-8*db50**-1.2
    ic = ((0.06 / ((n_f)**3 * (df15**(4/3))) )  + ( (n_f**(5/3) * (df15**(1/3))) / (1000 * db50**(5/3)) )  ) * u_shear_c**2
    return ic
ic = critical_gradient(n_f, df15, db50, delta, shields)
i_c = ic*100
print('The critical gradient is', ic,'[-] or', i_c, '%')
```

11. Stability parameter

```
def stability(i_total, ic):
    stability_formula = i_total/ic
    return stability_formula

print('The stability parameter',stability(i_total,ic))
```

All test cases for dimensionless sediment transport vs. $i_{2\%}/i_c$

[7]:
```
q_sd_T01  =[0.038, 0.0032, 0.0096, 0.0077, 0.1080]
q_sd_T02b =[0.30, 2.74, 6.30, 3.26]
q_sd_T03  =[1.314, 0.742, 0.043, 0.009, 0.026, 5.302, 0.345]
q_sd_T04  =[0.004, 0.409, 0.459, 0.003, 0.001, 0.143]
q_sd_T06a =[0.024, 0.030, 0.012, 1.488, 0.588, 2.776, 0.021]
q_sd_T07  =[0.079, 0.047, 0.096, 0.134, 0.012]

# Values below are multiplied with 10^3
stability_T01  = [0.30,0.46,0.86,0.98,2.92]
stability_T02b = [0.69,0.91,3.84,3.71]
stability_T03  = [0.23,0.27,0.50,0.77,1.40,1.36,1.66]
stability_T04  = [0.20,0.20,0.70,0.68,1.01,2.00]
stability_T06a = [0.19,0.24,0.32,0.73,0.71,0.91,2.08]
stability_T07  = [0.17,0.63,0.98,1.13,1.32]

plt.plot(stability_T01, q_sd_T01, '.' ,color='red')
plt.plot(stability_T02b, q_sd_T02b,'.' ,  color='blue')
plt.plot(stability_T03, q_sd_T03, '.',color='yellow')
plt.plot(stability_T04, q_sd_T04,'.', color='green')
plt.plot(stability_T06a, q_sd_T06a, '.' ,color='purple')
plt.plot(stability_T07, q_sd_T07, '.' ,color='orange')


plt.title(r'Dimensionless sediment transport vs. Stability parameter')

plt.xlabel(r'$i_a/i_c$')
plt.ylabel('$q_s^*$')
plt.legend(['T01','T02b','T03', 'T04', 'T06a', 'T07'], loc='center left', bbox_to_anchor=(1,0.5),prop={'size': 8})
plt.grid(True, which="both", ls="-", linewidth=0.4)
plt.show()
```

B.2 Wolters & Van Gent (2012

For Wolters & Van Gent the same steps as shown in Van de Sande are used. Only the pick a test was different, see figure below.

Pick a test

```
def test(test_name):
    if test_name == "Wolters":
        p_s    = 2650
        dfn50  = 22*10**-3
        df15   = 22.45*10**-3
        Df     = 55*10**-3
        db50   = 150*10**-6
        delta  = (p_s-p_w) / p_w
        shields= 0.02
        n_f    = 0.44
        return p_s, dfn50, df15, Df, db50, delta, shields, n_f

    else:
        return "Invalid test name."

test_name = input("Choose which test you want to see: ")
test = test(test_name)

if isinstance(test, str):
    print(test)
else:
    p_s, dfn50, df15, Df, db50, delta, shields, n_f = test
    print("p_s =", p_s)
    print("dfn50 =", dfn50)
    print("df15 =", df15)
    print("Df =", Df)
    print("db50 =", db50)
    print("delta =", delta)
    print("shields =", shields)
    print("n_f =", n_f)
```

B.3 Case study

For the case study the same steps as shown in Van de Sande are used. Only the flow conditions and the pick a test was different, see figure below.

```
#Constant conditions Lemmens
width        = 3
g            = 9.81
p_w          = 1000
p_s          = 2600
delta        = 1.63
shields      = 0.02
n_f          = 0.4
db50         = 145*10**-6
```

Pick a test

```
def test(test_name):
    if test_name == "Case study":
        dfn50  = 0.01
        return dfn50
    else:
        return "Invalid test name."

test_name = input("Choose which test you want to see: ")
test = test(test_name)

if isinstance(test, str):
    print(test)
else:
    dfn50= test
    print("dfn50 =", dfn50)
```